

# Control and Estimation of Induction Motor Drives

## 8.1 INTRODUCTION

The control and estimation of induction motor drives constitute a vast subject, and the technology has further advanced in recent years. Induction motor drives with cage-type machines have been the workhorses in industry for variable-speed applications in a wide power range that covers from fractional horsepower to multi-megawatts. These applications include pumps and fans, paper and textile mills, subway and locomotive propulsions, electric and hybrid vehicles, machine tools and robotics, home appliances, heat pumps and air conditioners, rolling mills, wind generation systems, etc. In addition to process control, the energy-saving aspect of variable-frequency drives is getting a lot of attention nowadays.

The control and estimation of ac drives in general are considerably more complex than those of dc drives, and this complexity increases substantially if high performances are demanded. The main reasons for this complexity are the need of variable-frequency, harmonically optimum converter power supplies, the complex dynamics of ac machines, machine parameter variations, and the difficulties of processing feedback signals in the presence of harmonics. While considering drive applications, we need to address the following questions:

- One-, two- or four-quadrant drive?
- Torque, speed, or position control in the primary or outer loop?
- Single- or multi-motor drive?
- Range of speed control? Does it include zero speed and field-weakening regions?
- Accuracy and response time?
- Robustness with load torque and parameter variations?
- Control with speed sensor or sensorless control?
- Type of front-end converter?

- Efficiency, cost, reliability, and maintainability considerations?
- Line power supply, harmonics, and power factor considerations?

In this chapter, we will study different control techniques of induction motor drives, including scalar control, vector or field-oriented control, direct torque and flux control, and adaptive control. Intelligent controls with expert systems, fuzzy logic, and the neural network will be covered in Chapters 10, 11, and 12, respectively. The estimation of feedback signals, particularly speed estimation in sensorless vector controls will be discussed. Variable-frequency power supplies will be considered with voltage-fed inverters, current-fed inverters, and cycloconverters. However, emphasis will be given to voltage-fed converters because of their popularity in industrial drives. The reader should thoroughly review the fundamentals of induction machines in Chapter 2 before embarking on this chapter.

## 8.2 INDUCTION MOTOR CONTROL WITH SMALL SIGNAL MODEL

The general control block diagram for variable-frequency speed control of an induction motor drive is shown in Figure 8.1. It consists of a converter-machine system with hierarchy of control loops added to it. The converter-machine unit is shown with voltage ( $V_s^*$ ) and frequency ( $\omega_e^*$ ) as control inputs. The outputs are shown as speed ( $\omega_r$ ), developed torque ( $T_e$ ), stator current ( $I_s$ ), and rotor flux ( $\psi_r$ ). Instead of voltage control, the converter may be current-controlled with direct or indirect voltage control in the inner loop. The machine's dynamic model given by Equations (2.104), (2.105), and (2.115) is nonlinear and multivariable. Besides, there are coupling effects between the input and output variables. For example, both the torque and flux of a machine are functions of voltage and frequency. Machine parameters may vary with saturation, temperature, and skin effect, adding further nonlinearity to the machine model. The converter can be described by a simplified model, which consists of an amplifier gain and a dead-time lag due to the PWM sampling delay. The system becomes discrete-time because of the converter and digital control sampling effects. All the control and feedback signals can be considered as dc

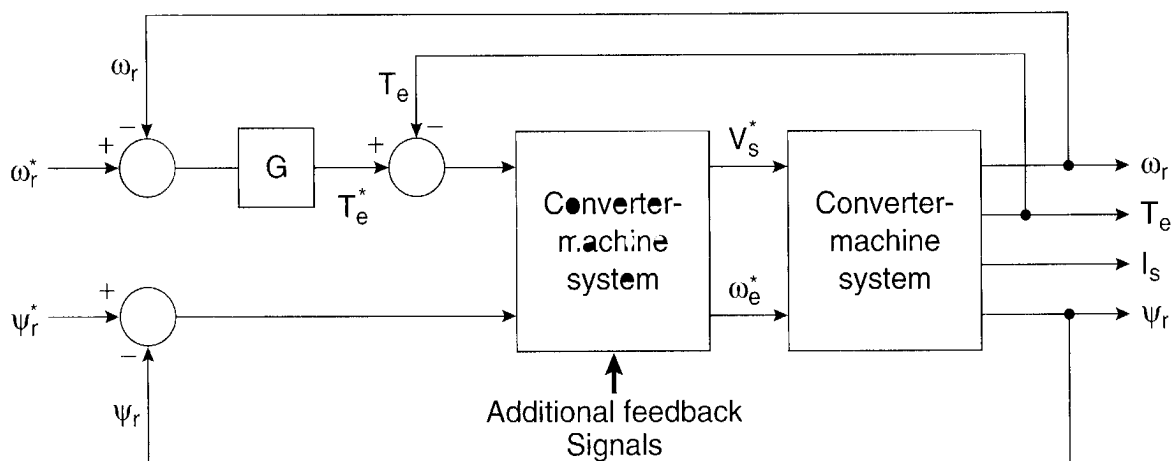


**Figure 8.1** General speed control block diagram of induction motor drive

and proportional to actual variables. The speed control is shown with an inner torque control loop, which may be optional. Adding a high-gain inner loop control provides the advantages of linearization, improved bandwidth, and the ability to control the signals within safe limits. Like a dc machine, the flux of an ac machine is normally controlled to be constant at the rated value because it gives fast response and high developed torque per ampere of current. In fact, the flux under consideration may be stator flux ( $\psi_s$ ), rotor flux ( $\psi_r$ ), or air gap flux ( $\psi_m$  or  $\psi_g$ ). However, the rotor flux control is considered in the present case. The inner control loops have faster response (i.e., higher bandwidth) than the outer loop. The “controller” block shown in the figure may have different structures, which will be discussed later.

Since an ac drive system is multivariable, nonlinear with internal coupling effect, and discrete-time in nature, its stability analysis is very complex. Computer simulation study becomes very useful for investigating the performance of the drive, particularly when a new control strategy is developed. Once the control structure and parameters of the control system are determined by the simulation study for acceptable performance, a prototype system can be designed and tested with further iteration of the controller parameters.

### 8.2.1 Small-Signal Model

Neglecting the discrete-time nature of the converter, the converter-machine system in Figure 8.1 can be linearized on a small-signal perturbation basis at a steady-state operating point and a transfer function model can be derived between a pair of input/output signals. The advantage of such a transfer function model is that the stability analysis of the drive system at the quiescent point is now possible using classical control theory, such as the Bode, Nyquist, or root-locus technique. Since the system is nonlinear, the poles, zeros, and gain of the transfer functions will vary as the steady-state operating point shifts. The close loop control system can then be designed with controller parameters such that at the worst operating point, the system is adequately stable and the performances are acceptable.

A dynamic model of an induction motor can be given by a fifth-order system, which is formed by combining Equations (2.104), (2.105), and (2.115). Assembling these equations in matrix form and applying a small-signal perturbation about a steady-state operating point, we get

$$\begin{bmatrix} v_{qso} + \Delta v_{qs} \\ v_{dso} + \Delta v_{ds} \\ v_{qro} + \Delta v_{qr} \\ v_{dro} + \Delta v_{dr} \\ T_{Lo} + \Delta T_L \end{bmatrix} = \begin{bmatrix} R_s + SL_s & (\omega_{eo} + \Delta\omega_e)L_s & SL_m & (\omega_{eo} + \Delta\omega_e)L_m & 0 \\ -(\omega_{eo} + \Delta\omega_e)L_s & R_s + SL_s & -(\omega_{eo} + \Delta\omega_e)L_m & SL_m & 0 \\ SL_m & (\omega_{eo} + \Delta\omega_e)L_m & R_r + SL_r & (\omega_{eo} + \Delta\omega_e)L_r & -L_m(i_{dso} + \Delta i_{ds}) - L_r(i_{dro} + \Delta i_{dr}) \\ -(\omega_{eo} + \Delta\omega_e)L_m & SL_m & -(\omega_{eo} + \Delta\omega_e)L_r & R_r + SL_r & L_m(i_{qso} + \Delta i_{qs}) + L_r(i_{qro} + \Delta i_{qr}) \\ \frac{3P}{2}L_m(i_{dro} + \Delta i_{dr}) & -\frac{3P}{2}L_m(i_{qro} + \Delta i_{qr}) & 0 & 0 & -\frac{2}{P}JS \end{bmatrix} \begin{bmatrix} i_{qso} + \Delta i_{qs} \\ i_{dso} + \Delta i_{ds} \\ i_{qro} + \Delta i_{qr} \\ i_{dro} + \Delta i_{dr} \\ \omega_{ro} + \Delta\omega_r \end{bmatrix} \quad (8.1)$$

where load torque disturbance  $T_L$  is considered an input signal. Parameters  $v_{qso}$ ,  $v_{dso}$ ,  $v_{qro}$ ,  $v_{dro}$ ,  $T_{Lo}$ ,  $\omega_{eo}$ ,  $i_{qso}$ ,  $i_{dso}$ ,  $i_{qro}$ ,  $i_{dro}$ , and  $\omega_{ro}$  describe the steady-state operating point and can be determined by solving the equations with all time derivatives (terms with  $S$ ) set equal to zero. Linearizing Equation (8.1) by neglecting the  $\Delta^2$  terms and eliminating steady-state terms, we get the small-signal linear state-space equation in the form

$$\frac{dX}{dt} = AX + BU \quad (8.2)$$

where

$$X = [\Delta i_{qs} \quad \Delta i_{ds} \quad \Delta i_{qr} \quad \Delta i_{dr} \quad \Delta \omega_r]^T \quad (8.3)$$

$$U = [\Delta V_s \quad 0 \quad 0 \quad 0 \quad \Delta \omega_e \quad \Delta T_L]^T \quad (8.4)$$

$$A = \frac{-1}{L_s L_r - L_m^2} \begin{bmatrix} R_s L_r & (L_s L_r - L_m^2) \omega_{ro} + L_m^2 \omega_{rs} & -R_r L_m & L_m L_r \omega_{ro} & L_m^2 i_{ds0} + L_m L_r i_{dr0} \\ -(L_s L_r - L_m^2) \omega_{ro} - L_m^2 \omega_{rs} & R_s L_r & -L_m L_r \omega_{ro} & -R_r L_m & -L_m^2 i_{qs0} - L_m L_r i_{qr0} \\ -R_s L_m & -L_m L_s \omega_{ro} & R_r L_s & (L_s L_r - L_m^2) \omega_{ro} - L_s L_r \omega_{rs} & -L_m L_s i_{ds0} - L_s L_r i_{dr0} \\ L_m L_s \omega_{ro} & -R_s L_m & -(L_s L_r - L_m^2) \omega_{ro} + L_s L_r \omega_{rs} & R_r L_s & L_m L_s i_{qs0} + L_s L_r i_{qr0} \\ \frac{-3}{8} \frac{P^2}{J} L_m (L_s L_r - L_m^2) i_{dr0} & \frac{3}{8} \frac{P^2}{J} L_m (L_s L_r - L_m^2) i_{qr0} & \frac{3}{8} \frac{P^2}{J} L_m (L_s L_r - L_m^2) i_{ds0} & \frac{-3}{8} \frac{P^2}{J} L_m (L_s L_r - L_m^2) i_{qs0} & 0 \end{bmatrix} \quad (8.5)$$

$$B = \frac{1}{L_s L_r - L_m^2} \begin{bmatrix} L_r & 0 & -L_m & 0 & -(L_s L_r - L_m^2) i_{ds0} & 0 \\ 0 & L_r & 0 & -L_m & (L_s L_r - L_m^2) i_{qs0} & 0 \\ -L_m & 0 & L_s & 0 & -(L_s L_r - L_m^2) i_{dr0} & 0 \\ 0 & -L_m & 0 & L_s & (L_s L_r - L_m^2) i_{qr0} & 0 \\ 0 & 0 & 0 & 0 & 0 & -\frac{P}{2J} (L_s L_r - L_m^2) \end{bmatrix} \quad (8.6)$$

In the expressions above, the machine is considered stator-fed only (i.e.,  $\Delta v_{qr} = \Delta v_{dr} = 0$ ) and the stator voltage  $\Delta V_s$  is aligned to the  $q^e$ -axis so that  $\Delta v_{qs} = \Delta V_s$  and  $\Delta v_{ds} = 0$ , leaving only  $\Delta V_s$ ,  $\Delta \omega_e$ , and  $\Delta T_L$  as input variables. The small-signal block diagram is shown in Figure 8.2, where the electrical and mechanical responses have been separated. The converter gain can be easily merged with the input voltage signal  $\Delta V_s$ . The converter-machine model generates currents from input control signals  $\Delta V_s$  and  $\Delta \omega_e$ , and feedback speed signal  $\Delta \omega_r$  acts to generate the speed-induced CEMF. The developed torque  $\Delta T_e$  is synthesized from the currents by the equation

$$\Delta T_e = \frac{3}{2} \left( \frac{P}{2} \right) L_m \left[ (i_{dr0} \Delta i_{qs} + i_{qs0} \Delta i_{dr}) - (i_{ds0} \Delta i_{qr} + i_{qr0} \Delta i_{ds}) \right] \quad (8.7)$$

The other small-signal outputs,  $\Delta I_s$  and  $\Delta \psi_r$  in Figure 8.1, can be synthesized from the current signals as follows:

The stator current  $\hat{I}_s$  is given as

$$|\bar{I}_s| = |I_{qds}| = \sqrt{i_{qs}^2 + i_{ds}^2} \quad (8.8)$$

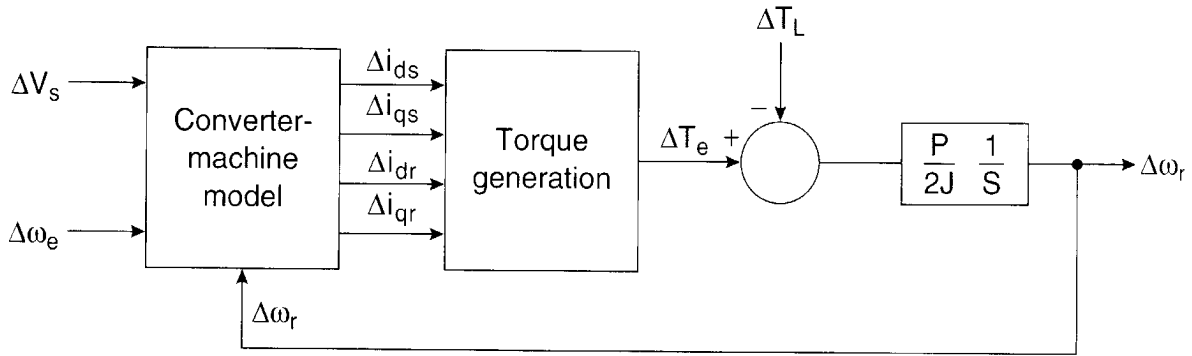


**Figure 8.2** Small-signal control block diagram

which can be small-signal linearized as

$$\left| \Delta \bar{I}_s \right| = \frac{i_{qso}}{\sqrt{i_{qso}^2 + i_{dso}^2}} \Delta i_{qs} + \frac{i_{dso}}{\sqrt{i_{qso}^2 + i_{dso}^2}} \Delta i_{ds} \quad (8.9)$$

Similarly, the rotor flux is given as

$$\left| \bar{\psi}_r \right| = \left| \psi_{qdr} \right| = \sqrt{\psi_{qr}^2 + \psi_{dr}^2} \quad (8.10)$$

where

$$\psi_{qr} = L_r i_{qr} + L_m i_{qs} \quad (8.11)$$

$$\psi_{dr} = L_r i_{dr} + L_m i_{ds} \quad (8.12)$$

can be easily derived from the  $d^e$ - $q^e$  equivalent circuits of Figure 2.23.

The linearized equation for the rotor flux can be derived as

$$\begin{aligned} \left| \Delta \bar{\psi}_r \right| &= \frac{\psi_{qro}}{\psi_{ro}} \Delta \psi_{qr} + \frac{\psi_{dro}}{\psi_{ro}} \Delta \psi_{dr} \\ &= \frac{L_m (L_r i_{qro} + L_m i_{qso})}{\psi_{ro}} \Delta i_{qs} + \frac{L_m (L_r i_{dro} + L_m i_{dso})}{\psi_{ro}} \Delta i_{ds} \\ &\quad + \frac{L_r (L_r i_{qro} + L_m i_{qso})}{\psi_{ro}} \Delta i_{qr} + \frac{L_r (L_r i_{dro} + L_m i_{dso})}{\psi_{ro}} \Delta i_{dr} \end{aligned} \quad (8.13)$$

where

$$\psi_{r0} = \sqrt{(L_r i_{qro} + L_m i_{qso})^2 + (L_r i_{dro} + L_m i_{dso})^2} \quad (8.14)$$

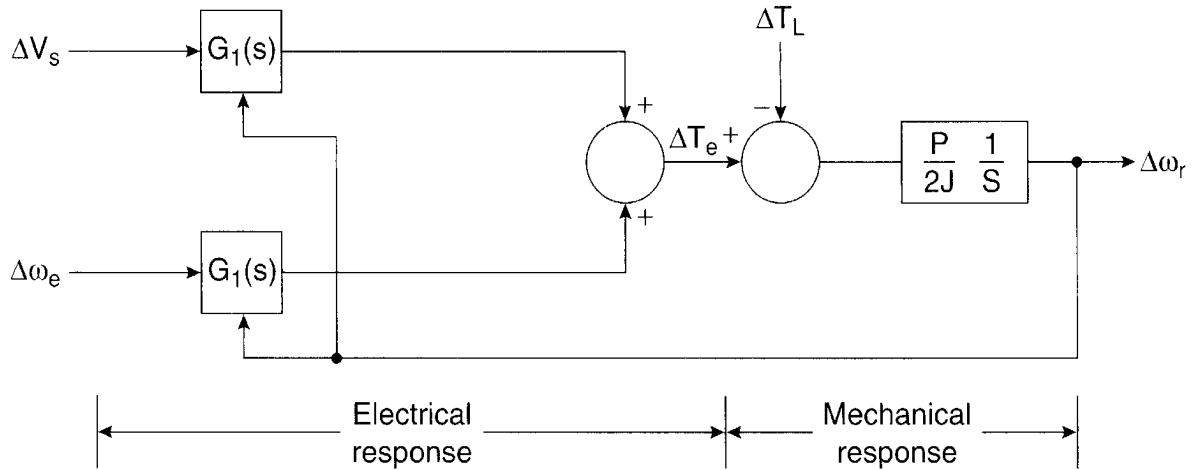


**Figure 8.3** Small-signal transfer function block diagram

The small-signal transfer function block diagram derived from Figure 8.2 is shown in Figure 8.3. Here, the transfer functions  $G_1(S)$  and  $G_2(S)$  are defined as

$$G_1(S) = \left. \frac{\Delta T_e}{\Delta V_s} \right|_{\Delta \omega_r = 0, \Delta \omega_e = 0} \quad (8.15)$$

$$G_2(S) = \left. \frac{\Delta T_e}{\Delta \omega_e} \right|_{\Delta \omega_r = 0, \Delta V_s = 0} \quad (8.16)$$

In these equations, the speed is treated as a constant parameter ( $\Delta \omega_r = 0$ ), assuming the system inertia  $J$  is very large (i.e., mechanical response is more sluggish compared to electrical response). In such a case, the response of speed  $\Delta \omega_r$  is essentially dictated by the  $J$  parameter. For any finite inertia system, transfer functions  $\Delta \omega_r / \Delta V_s$ ,  $\Delta \omega_r / \Delta \omega_e$ , and  $\Delta \omega_r / \Delta T_L$  can be derived from the state-space form of Equation (8.2).

### 8.3 SCALAR CONTROL

Scalar control, as the name indicates, is due to magnitude variation of the control variables only, and disregards the coupling effect in the machine. For example, the voltage of a machine can be controlled to control the flux, and frequency or slip can be controlled to control the torque. However, flux and torque are also functions of frequency and voltage, respectively. Scalar control is in contrast to vector or field-oriented control (will be discussed later), where both the magnitude and phase alignment of vector variables are controlled. Scalar-controlled drives give somewhat inferior performance, but they are easy to implement. Scalar-controlled drives have been widely used in industry. However, their importance has diminished recently because of the superior performance of vector-controlled drives, which is demanded in many applications. In this section, a few selected scalar control techniques with voltage-fed and current-fed inverters will be discussed.

### 8.3.1 Voltage-Fed Inverter Control

#### 8.3.1.1 Open Loop Volts/Hz Control

The open loop volts/Hz control of an induction motor is by far the most popular method of speed control because of its simplicity, and these types of motors are widely used in industry. Traditionally, induction motors have been used with open loop 60 Hz power supplies for constant speed applications. For adjustable speed applications, frequency control is natural. However, voltage is required to be proportional to frequency so that the flux ( $\psi_s = V_s/\omega_e$ ) remains constant (see Figure 2.14), neglecting the stator resistance  $R_s$  drop. Figure 8.4 shows the block diagram of the volts/Hz speed control method. The power circuit consists of a diode rectifier with a single- or three-phase ac supply, LC filter, and PWM voltage-fed inverter. Ideally, no feedback signals are needed for the control. The frequency  $\omega_e^*$  is the primary control variable because it is approximately equal to speed  $\omega_r$ , neglecting the small slip frequency  $\omega_{sl}$  of the machine. The phase voltage  $V_s^*$  command is directly generated from the frequency command by the gain factor  $G$ , as shown, so that the flux  $\psi_s$  remains constant. If the stator resistance and leakage inductance of the machine are neglected, the flux will also correspond to the air gap flux  $\psi_m$  or rotor flux  $\psi_r$ . As the frequency becomes small at low speed, the stator resistance tends to absorb the major amount of the stator voltage, thus weakening the flux. The boost voltage  $V_0$  is

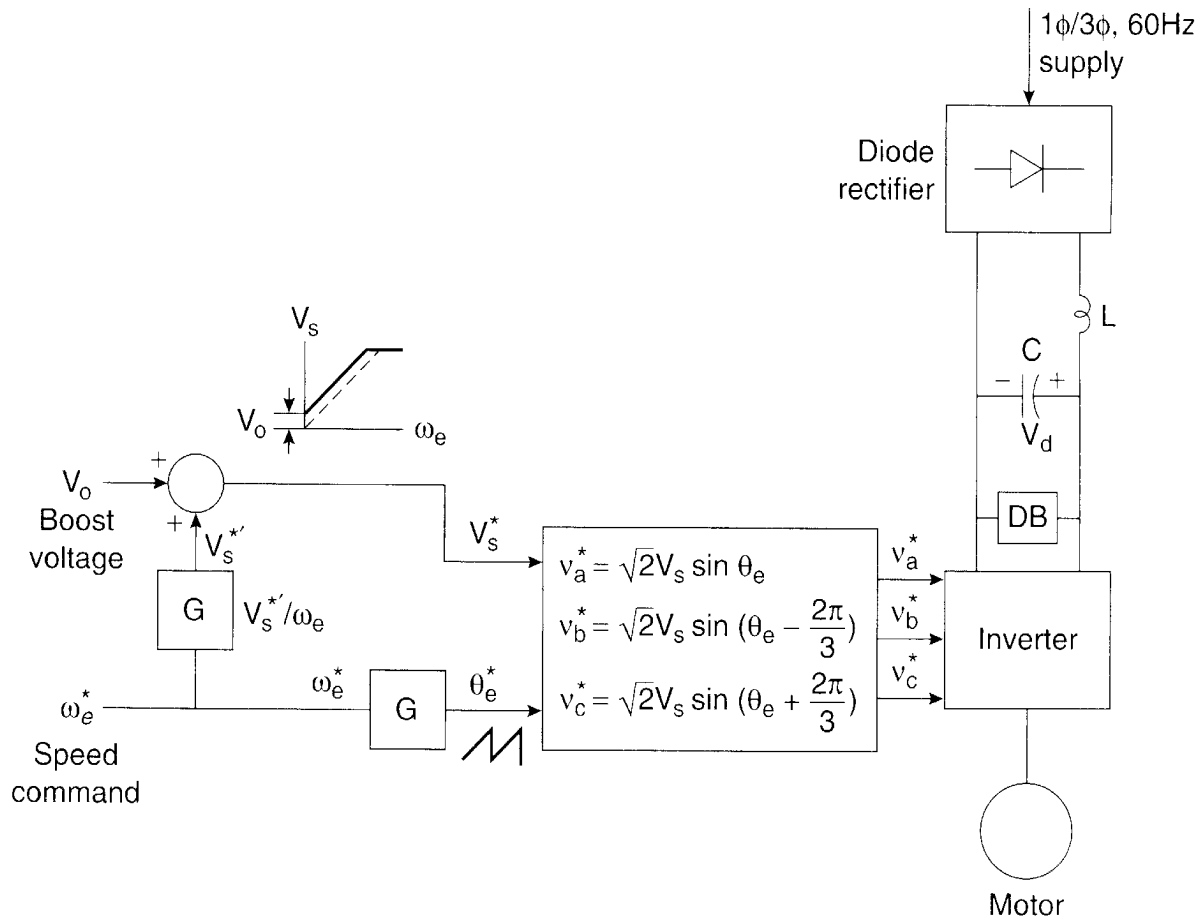


**Figure 8.4** Open loop volts/Hz speed control with voltage-fed inverter

added so that the rated flux and corresponding full torque become available down to zero speed. Note that the effect of boost voltage becomes negligible at higher frequencies. The  $\omega_e^*$  signal is integrated to generate the angle signal  $\theta_e^*$ , and the corresponding sinusoidal phase voltages ( $v_a^*$ ,  $v_b^*$ , and  $v_c^*$  signals) are generated by the expressions shown in the figure. The PWM controller is merged with the inverter block.

Figure 8.5 shows the drive's steady-state performance on a torque-speed plane with a fan or pump-type load ( $T_L = K\omega_r^2$ ). As the frequency is gradually increased, the speed also increases almost proportionally, as indicated by points 1, 2, 3, 4, etc. The operation can be continued smoothly in the field-weakening region where the supply voltage  $V_s$  saturates.

Now consider the load torque and line voltage variation effects. If the initial operating point is 3 and the load torque is increased to  $T_L'$  for the same frequency command, the speed will droop from  $\omega_r$  to  $\omega_r'$ . This droop is small, particularly with a high-efficiency (i.e., low slip) machine, and is easily tolerated for a pump or fan-type drive where precision speed control is not necessary. Assume now that the operation is at point a in another torque-speed curve. If the ac line voltage decreases, that lowers the machine terminal voltage. The speed will also droop corresponding to point b, as shown in the figure. As the literature suggests, a speed droop correction in an open loop control can be achieved by adding an estimated slip signal with the frequency command.

If the frequency command  $\omega_e^*$  is changed abruptly by a small increment, the slip will change to change the developed torque (within the safe limit), but the speed will tend to remain constant because of machine inertia. However, if it is desired to change the speed by a large step of the frequency command (positive or negative), the drive will easily become unstable. The satisfactory acceleration/deceleration characteristics of the machine are explained in Figure 8.6.

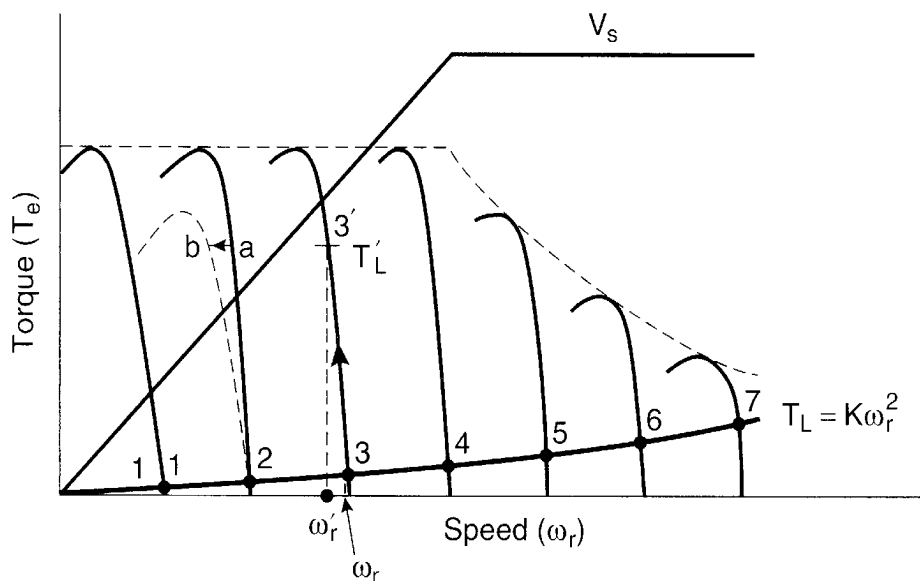


**Figure 8.5** Torque-speed curves showing effect of frequency variation, load torque, and supply voltage changes



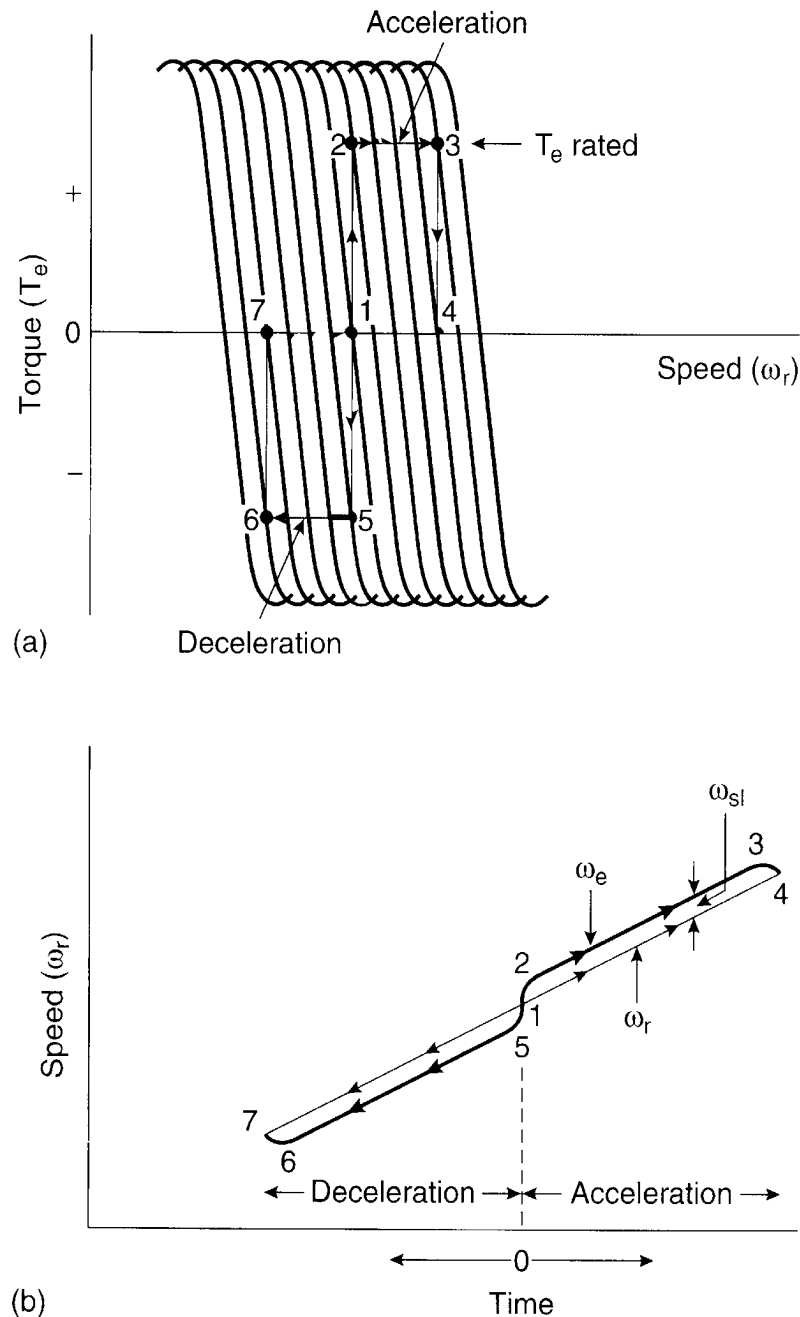


**Figure 8.6** Acceleration/deceleration characteristics with volts/Hz control:  
 (a) On torque-speed curves,  
 (b) As function of time

Assume a pure inertia-type load for simplicity and that the machine is initially operating at point 1. The command frequency is now increased abruptly by a small step so that with an increment of slip frequency, the operating point shifts to point 2, which corresponds to the rated, developed torque. The drive now goes through constant acceleration with the ramping of the frequency command when the speed tracks the frequency within the limit of slip frequency so that the stability and safe stator current limit are maintained. At operating point 3, the frequency

command can be decremented to attain the steady-state operating point, which is 4. The machine torque and speed are related by the following equation:

$$\omega_r = \int \frac{(T_e - T_L)}{J} dt \quad (8.17)$$

where  $J$  = moment of inertia,  $T_e$  = developed torque, and  $T_L$  = load torque (zero in this case). With the rated  $T_e$ , the slope of acceleration  $d\omega_r/dt$ , as indicated in Figure 8.6(b), is dictated by parameter  $J$ , that is, a higher  $J$  will permit slow acceleration, and vice versa. If it is possible to estimate  $J$  on-line for a variable inertia load, the acceleration of the drive can be predetermined. The deceleration performance is similar, and it is also explained in Figure 8.6. With a diode rectifier on the line side, the inverter will need a dynamic brake, as indicated in Figure 8.4. By decrementing the frequency command in a step, the operating point will shift from point 1 to 5 due to a negative developed torque. It will then decelerate with constant slope given by Equation (8.17) until the steady-state operating point, 7, can be reached again.

Typical drive performance with open loop volts/Hz control in both the accelerating and decelerating conditions with load torque  $T_L = K \omega_r^2$  is given by the simulation results shown in Figure 8.7. The inherent machine coupling effect slows down the torque response, as explained before. In addition, there is some amount of underdamping in the torque and flux responses, which increases at lower frequencies but does not affect the speed response because of inertia filtering. Drift in the flux signal for varying torque (i.e., stator current) is also evident. Small-signal analysis and simulation study indicate that at certain regions of operation, the system tends to be unstable [3].

#### 8.3.1.2 Energy Conservation Effect by Variable Frequency Drive

Numerous ac motor drives are used with a pump or fan-type load, where fluid flow control is needed. The traditional method of flow control is by operating the machine at a constant speed with a 60 Hz power supply, and then controlling the flow by throttle opening. The efficiency of this method of flow control is poor, as shown in Figure 8.8, where power consumption is plotted with the loading factor. Variable-frequency speed control of the drive with a fully open throttle reduces power consumption, which is indicated in the figure. For example, with 60 percent loading, the efficiency improvement can be as high as 35 percent. Since drives operate most of the time at light loads, the accumulated energy savings for a prolonged time period can be substantial. The payback period for investment cost of power electronics is small, particularly where the energy cost is high. In addition to the economic factor, efficient utilization of energy reduces the energy demand and correspondingly helps solve the environmental pollution problem where it is generated by fossil fuels. Further improvement of drive efficiency by programming the flux at light loads will be discussed later.

#### 8.3.1.3 Speed Control with Slip Regulation

An improvement of open loop volts/Hz control is close loop speed control by slip regulation as shown in Figure 8.9. Here, the speed loop error generates the slip command  $\omega_{sl}^*$  through

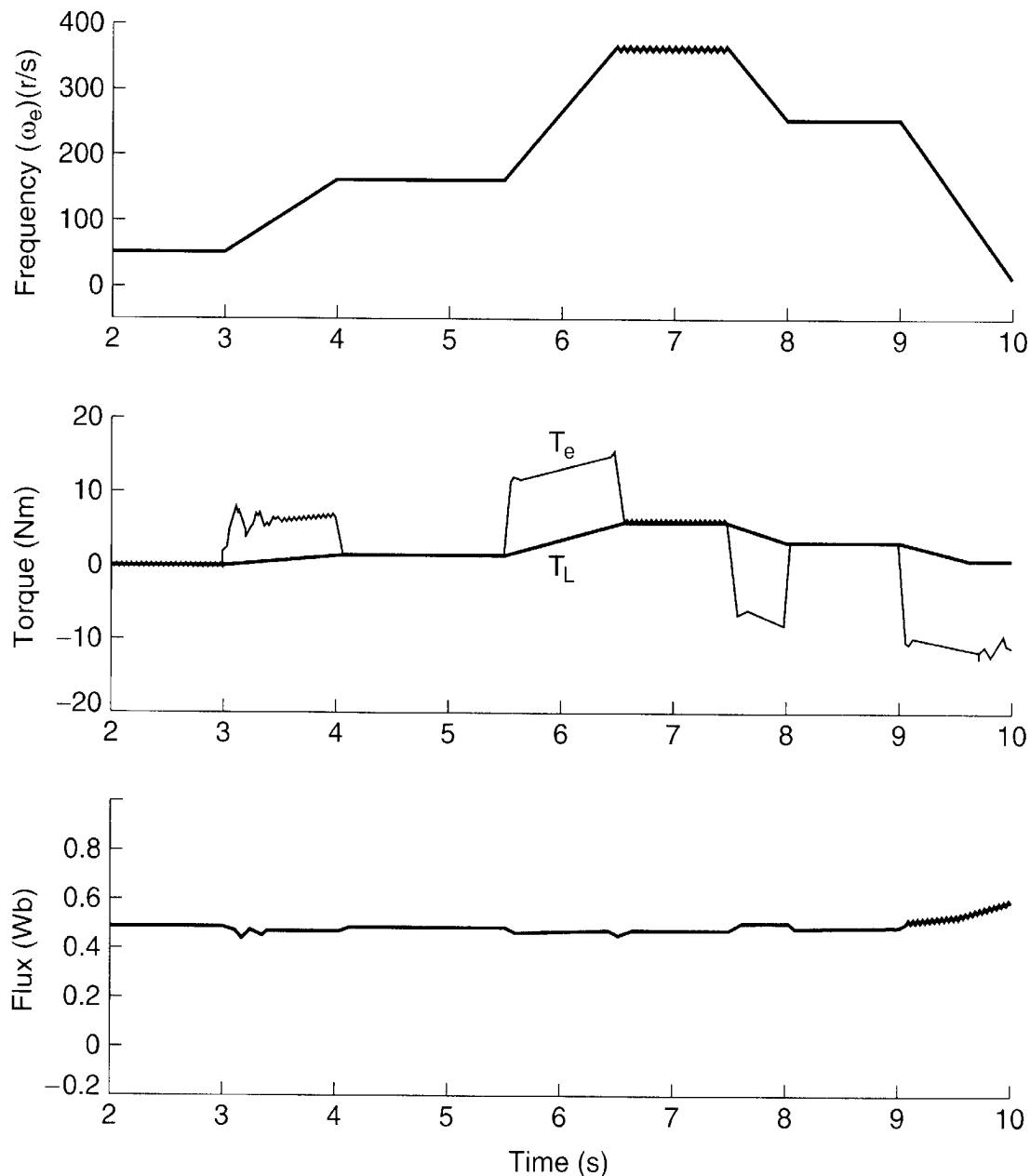


**Figure 8.7** Volts/Hz control performance

a proportional-integral (P-I) controller and limiter. The slip is added to the feedback speed signal to generate the frequency command as shown. The frequency command  $\omega_e^*$  also generates the voltage command through a volts/Hz function generator, which incorporates the low-frequency stator drop compensation. Since the slip is proportional to the developed torque at constant flux (Equation (2.41)), the scheme can be considered as an open loop torque control within a speed control loop. The feedback current signal is not used anywhere in the loop. With a step-up speed command, the machine accelerates freely with a slip limit that corresponds to the stator current or torque limit, and then settles down to the slip value at steady state as dictated by the load torque. If the command speed  $\omega_r^*$  is reduced by a step, the drive goes into regenerative or dynamic braking mode and decelerates with constant negative slip  $-\omega_{sl}^*$ , as indicated in the

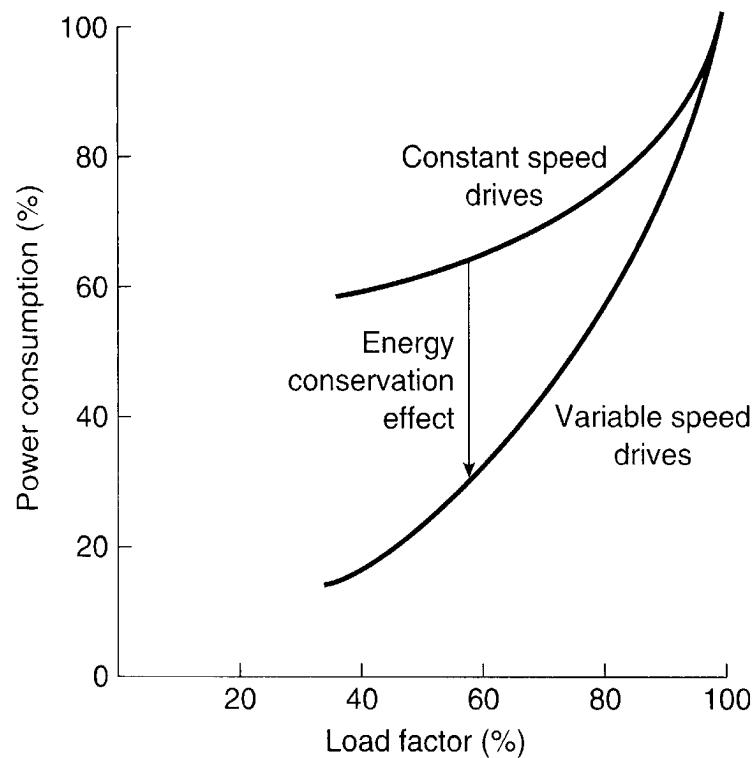


**Figure 8.8** Energy-saving characteristics with variable-frequency speed control

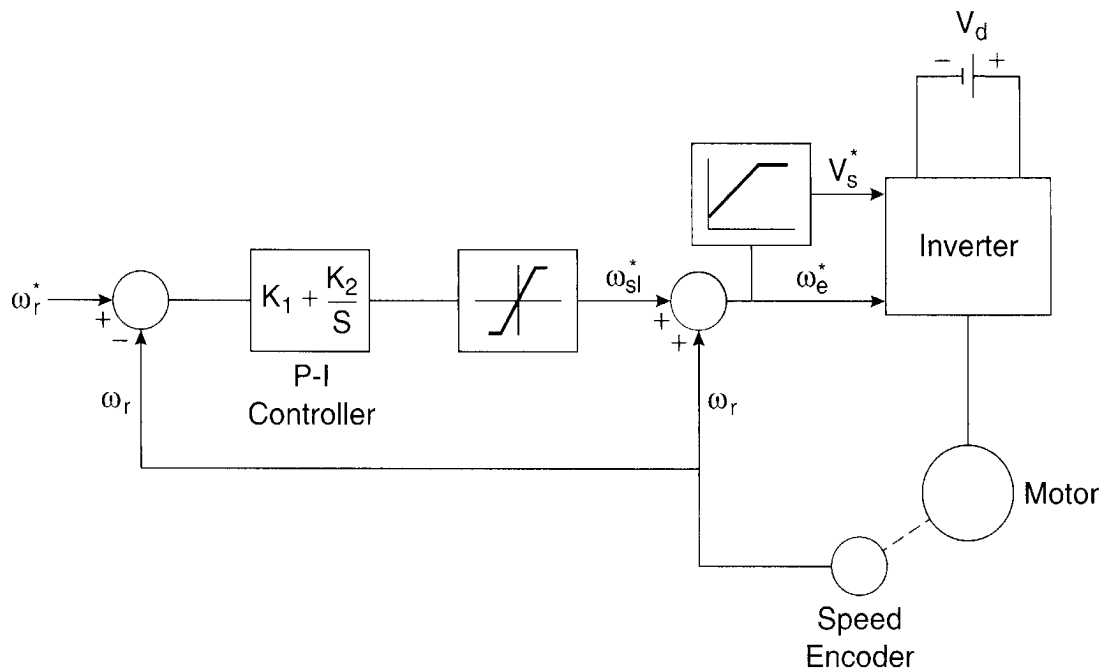


**Figure 8.9** Close loop speed control with volts/Hz control and slip regulation

figure. The effects of load torque and line voltage variation are explained in Figure 8.10. If the initial operating point is 1 and the load torque is increased from  $T_L$  to  $T_L'$ , the speed will tend to drop corresponding to point 2. However, the speed control loop will increase the frequency until the original speed is restored at point 3. Since there is no close loop flux control, the line voltage variation will cause some flux drift. Again, if the initial operating point is 1 on curve *a* of Figure

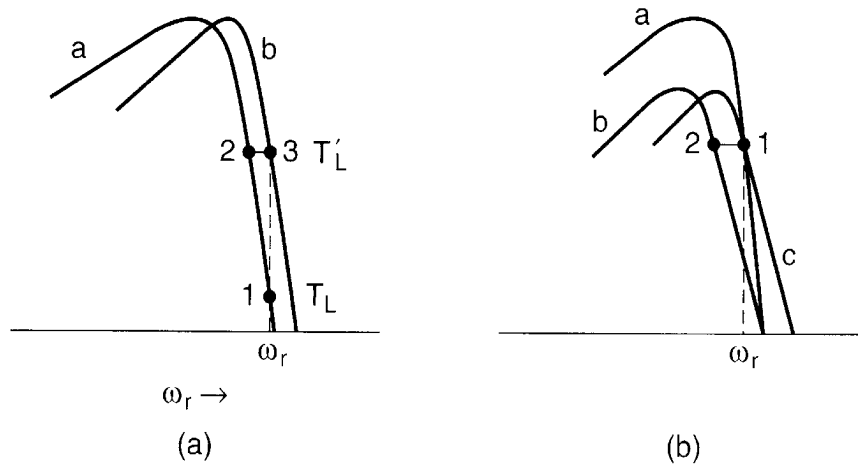


**Figure 8.10** (a) Effect of load torque variation, (b) Effect of supply voltage variation

8.10(b), the decrease of line voltage will reduce the flux, tending to shift the operating point to 2. The resulting speed drop will act on the speed loop and raise the frequency to restore the original speed at point 1 on curve *c*. The system works well in the field-weakening mode also.

#### 8.3.1.4 Speed Control with Torque and Flux Control

As discussed above, the volts/Hz control has the disadvantage that the flux may drift, and as a result, the torque sensitivity with slip (Equation (2.41)) will vary. In addition, line voltage variation, incorrect volts/Hz ratio, stator drop variation by line current, and machine parameter variation may cause weaker flux or the flux may saturate. In Figure 8.9, if the flux becomes weak, the developed torque will decrease with the slip limit and the machine's acceleration/deceleration capability will decrease.

A speed control system with close loop torque and flux control is shown in Figure 8.11. Additional feedback loops mean complexity of additional feedback signal synthesis and potential stability problems. A torque loop within the speed loop improves the speed loop's response. The flux control loop controls the voltage  $V_s^*$  as shown. Both the torque and flux feedback signals can be estimated from the machine terminal voltages and currents, as indicated. The feedback signal estimation will be discussed later. With constant  $\hat{\psi}_r^*$  command, as the speed increases, the voltage increases proportionally until square-wave mode is reached and field-weakening mode starts. However, if PWM operation is desired in field-weakening mode, the flux command must be decreased to vary inversely with the speed signal so that the PWM controller does not saturate. The flux control loop is usually slower than the torque control loop. The drive can operate in regenerative (or dynamic) braking mode, but the reversal of speed requires a reversal of the phase sequence of the inverter.

With scalar control, as the frequency command  $\omega_e^*$  is increased by the torque loop, the flux temporarily decreases until it is compensated by the sluggish flux control loop. This inherent coupling effect slows down the torque response.

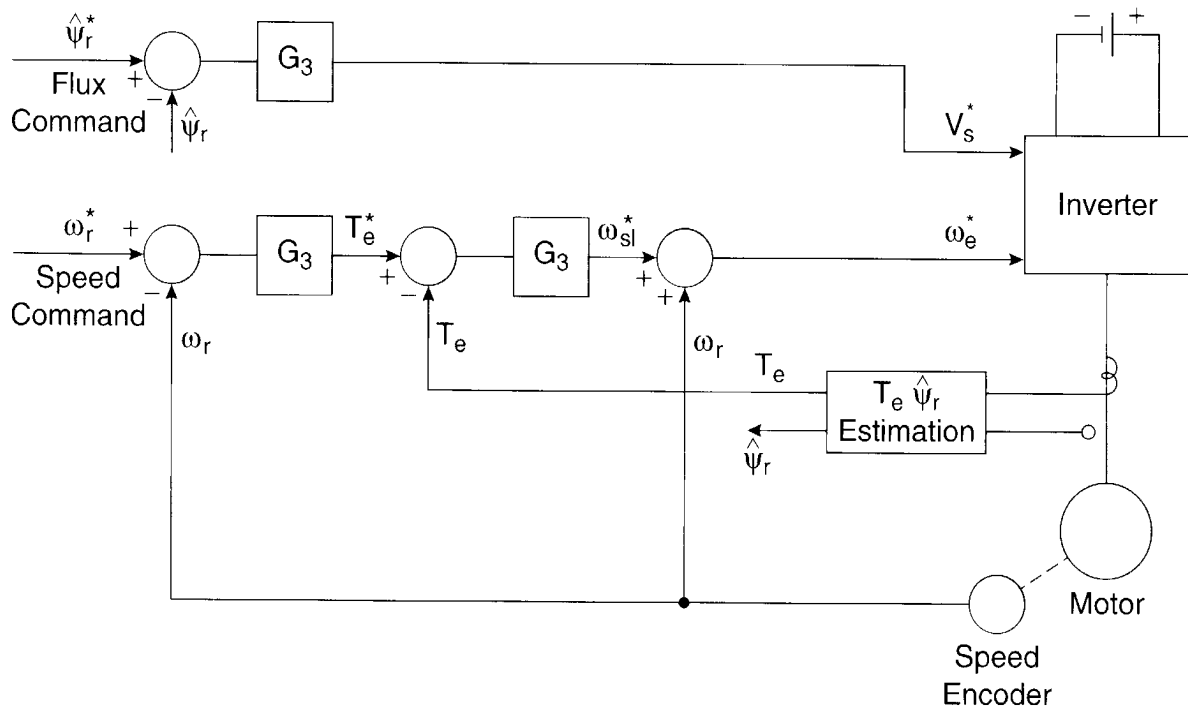


**Figure 8.11** Close loop speed control with torque and flux control

#### 8.3.1.5 Current-Controlled Voltage-Fed Inverter Drive

Instead of controlling inverter voltage by the flux loop, the stator current can also be controlled. Close loop current control is beneficial to power semiconductors because of the inherent protection from overcurrent. Besides, the torque and flux of the machine are directly sensitive to currents. A voltage-fed inverter drive with outer loop torque and flux control and hysteresis-band current control in the inner loop is shown in Figure 8.12. Instead of constant rated flux, the flux can be programmed with torque as shown for a light-load efficiency improvement, which will be discussed later. In the figure, the flux control loop generates the stator current magnitude, and its frequency command is generated by the torque loop. The three-phase command currents are then generated by the relations shown in the figure. The feedback phase currents  $i_a$ ,  $i_b$ , and  $i_c$  can be sensed by two current sensors because for an isolated neutral load,  $i_a + i_b + i_c = 0$ .

The performance of the drive for subway traction [5] in both acceleration and regenerative braking modes is explained in Figure 8.13. The figure is essentially the same as Figure 2.14 except that a braking region has been added. In the constant torque region, the inverter operates in the PWM current control mode and has the features of a current-fed inverter. Beyond the base speed, the inverter operates in square-wave mode, because with the constant flux command, the PWM controller fully saturates and the current commands are converted to square-wave voltage commands. In field-weakening mode, only frequency variation by slip control is possible to control the torque. To operate on the torque envelope, the slip is increased to the maximum value in a preprogrammed manner so that the stator current remains constant within the limit value. Beyond the constant power region, the slip remains constant, but the stator current decreases as indicated. The drive may operate at reduced torque at any speed by the reduction of slip. The

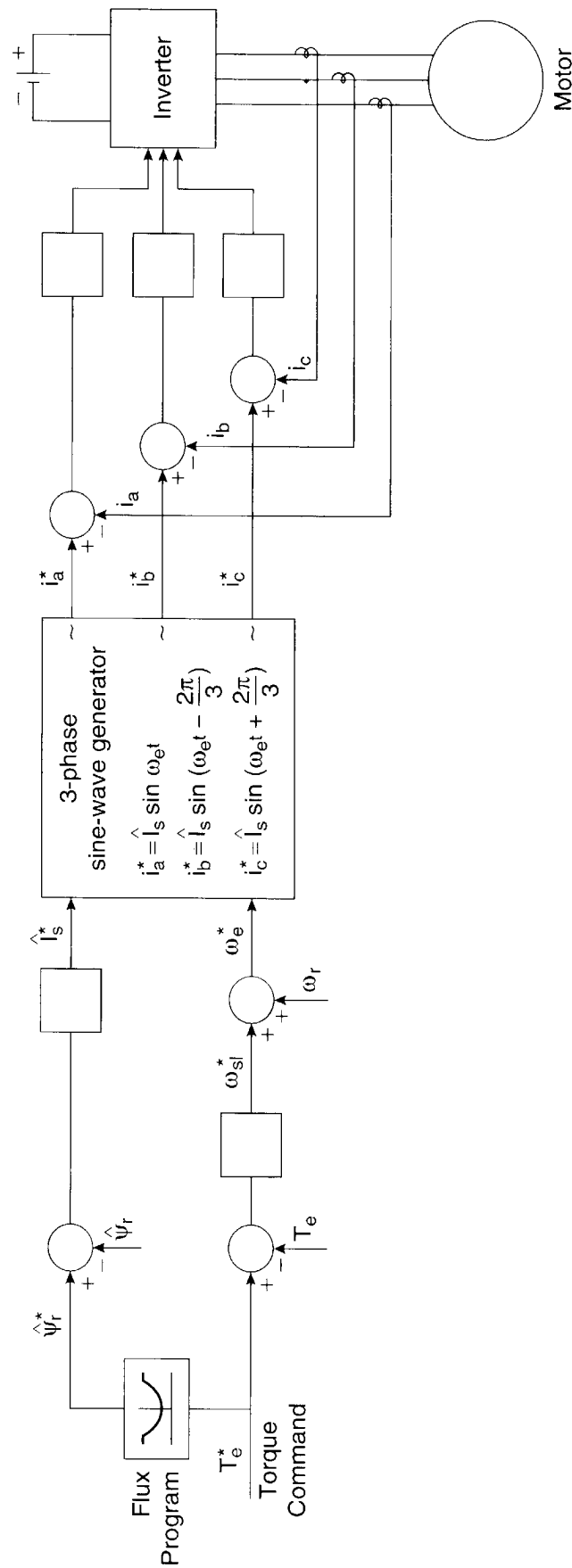


**Figure 8.12** Voltage-fed, current-regulated inverter drive with torque and flux control

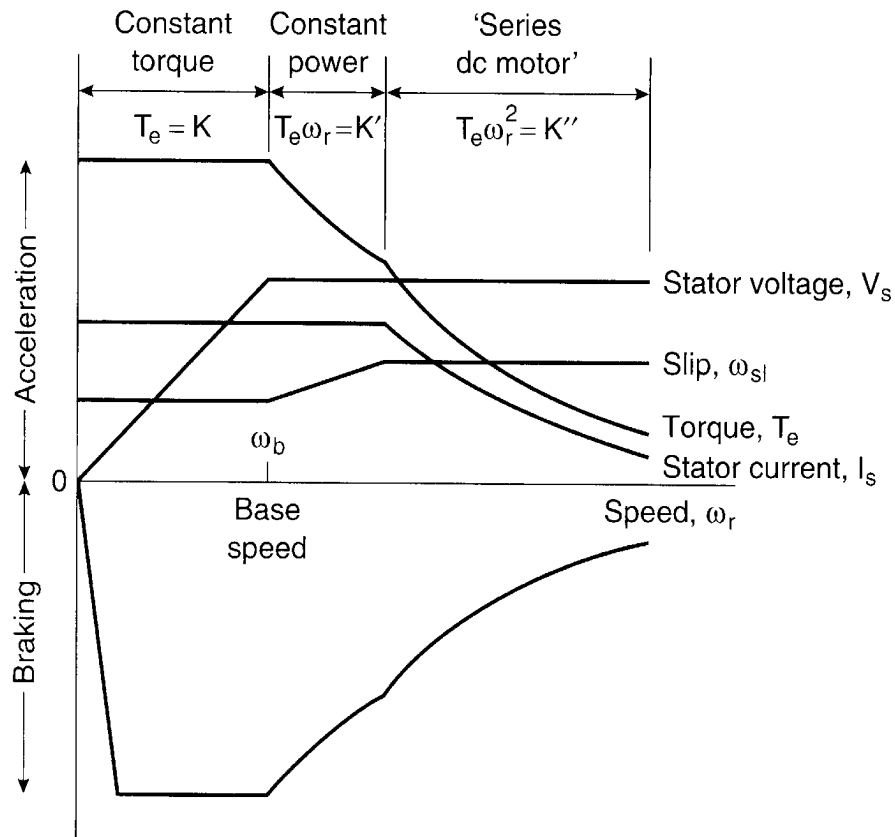


**Figure 8.13** Drive characteristics in acceleration and braking modes

available regenerative braking torque is diminished as the speed decreases and then vanishes at zero speed because of the circuit drops.

#### 8.3.1.6 Traction Drives with Parallel Machines

For a voltage-fed inverter system, multiple inverters can be operated in parallel with a single rectifier, or multiple machines can be operated in parallel with a single inverter. In many applications, such as conveyer lines, extruder mills, and subway and locomotive tractions, several identical induction motors are required to operate in parallel with one inverter. Figure 8.14 shows a typical IGBT converter locomotive drive where two identical machines of equal power rating operate in parallel with a single voltage-fed inverter, and each machine drives an axle of the locomotive. If the machines have matched torque-speed characteristics and their speeds are equal, each will offer identical impedance on the variable frequency supply line and their torque sharing will be equal at all operating conditions. In practice, there will be some amount of mismatch between machine characteristics, and speeds may not be identical because of mismatch between the wheel diameters.

Consider first some mismatch in machine characteristics, that is, machine 1 has lower slip than machine 2, as shown in Figure 8.15(a). The wheel diameters for each axle are identical so that the speed  $\omega_r$  is the same. With supply frequency  $\omega_e$ , the slip will be the same in both motoring and regenerative conditions. Machine 1, with lower slip characteristics, will share more torque than machine 2. With high-efficiency, low-slip machines, this torque-sharing inequality



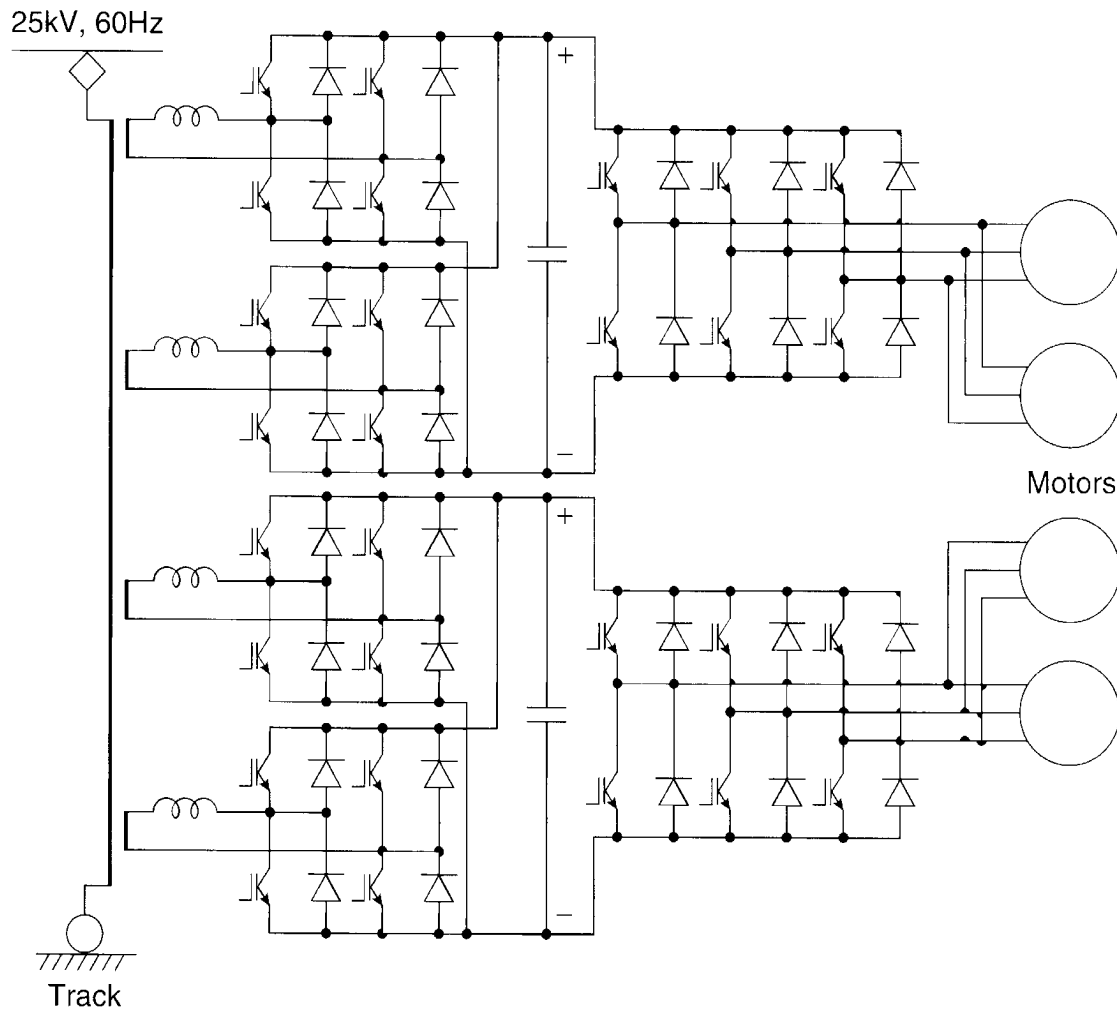


**Figure 8.14** Voltage-fed inverter locomotive drive with parallel machines

will be greater. The torque sharing of machine 1 in motoring mode may be excessive to induce slippage of the axle wheels. The incrementation of speed as a result of slippage will decrease its torque sharing, and therefore, will tend to have self-correction. In the regenerative mode, if there is a wheel slippage of machine 1, its speed incrementation will induce larger torque sharing, thus worsening the condition.

Consider now that the machines are exactly matched, but the wheel diameter of machine 2 is slightly shorter than that of machine 1, which will cause  $\omega_{r2} > \omega_{r1}$  for the same vehicle speed. This condition, as indicated in Figure 8.15(b), will cause higher torque sharing ( $T_{e1}$ ) for machine 1 in motoring condition, but lower torque sharing ( $T_{b1}$ ) in regenerative mode. The wheel slippage characteristics will be the same as before. Again, in practice, both machine mismatch and unequal wheel diameter problems may coexist. The composite problem is left as an exercise to the reader. Open loop volts/Hz speed control is very convenient in these applications. However, close loop high-performance control, such as vector control, is also possible by considering mean feedback signals in closely matched installations.

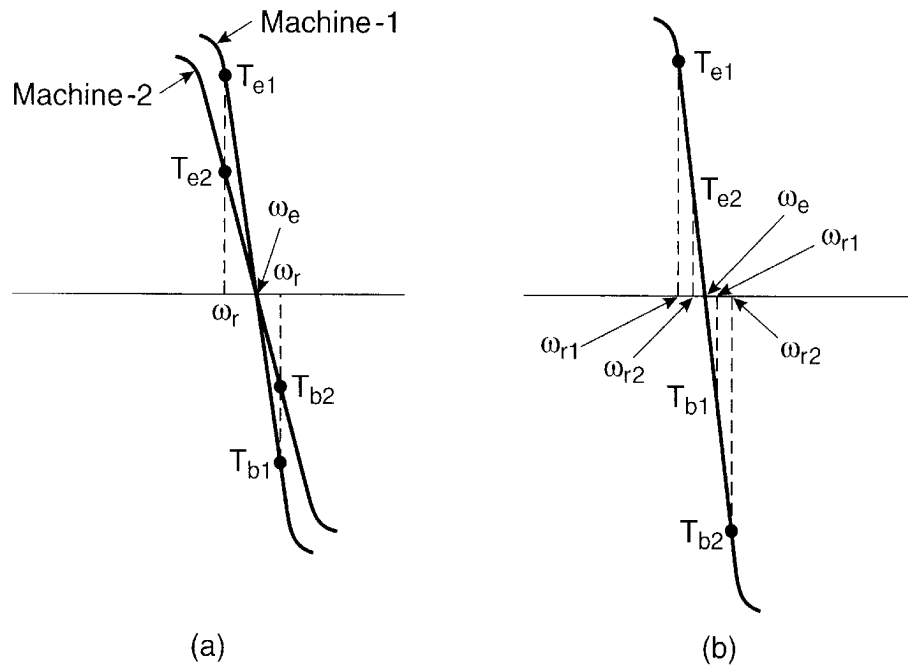


**Figure 8.15** (a) Characteristics of mismatched machines but equal wheel diameters, (b) Characteristics of matched machines but unequal wheel diameters

### 8.3.2 Current-Fed Inverter Control

Some of the control principles of voltage-fed inverter drives, as discussed above, are also applicable for current-fed inverter drives.

#### 8.3.2.1 Independent Current and Frequency Control

In a current-fed inverter drive, the dc link current and inverter frequency are the two control variables where the current can be controlled by varying the firing angle of the front-end thyristor rectifier. Unfortunately, a current-fed inverter system cannot be operated in an open loop like a voltage-fed inverter drive. A minimal close loop control system of a current-fed inverter system, where the dc link current  $I_d$  and slip  $\omega_{sl}$  are controlled independently, is shown in Figure 8.16(a). Figure 8.16(b) shows its performance characteristics [6]. The current  $I_d$  is controlled by a feedback loop that controls the rectifier output voltage  $V_d$ . The commanded slip is added with the speed signal  $\omega_r$  to generate the frequency command  $\omega_e^*$ . In acceleration mode, the slip is positive, but regeneration will be effective with a negative slip command when both  $V_d$  and  $V_f$  voltages become negative and power is fed back to the source. The main disadvantage of the system is that it has no flux control. The developed torque of the drive can be controlled either by the current  $I_d$  or the slip signal  $\omega_{sl}$ . Machine acceleration in constant torque from point 1 to point 2 with constant  $I_d$  and constant  $\omega_{sl}$  is shown in Figure 8.16(b). As explained in Figure 2.16, the machine is intentionally operated in a statically unstable region of the torque-speed curve so that the flux remains below saturation. At steady-state point 3, if the slip is reduced to balance developed torque with the load torque, saturation will occur. If, on the other hand, the current  $I_d$  is reduced at constant slip, the flux may be too low.

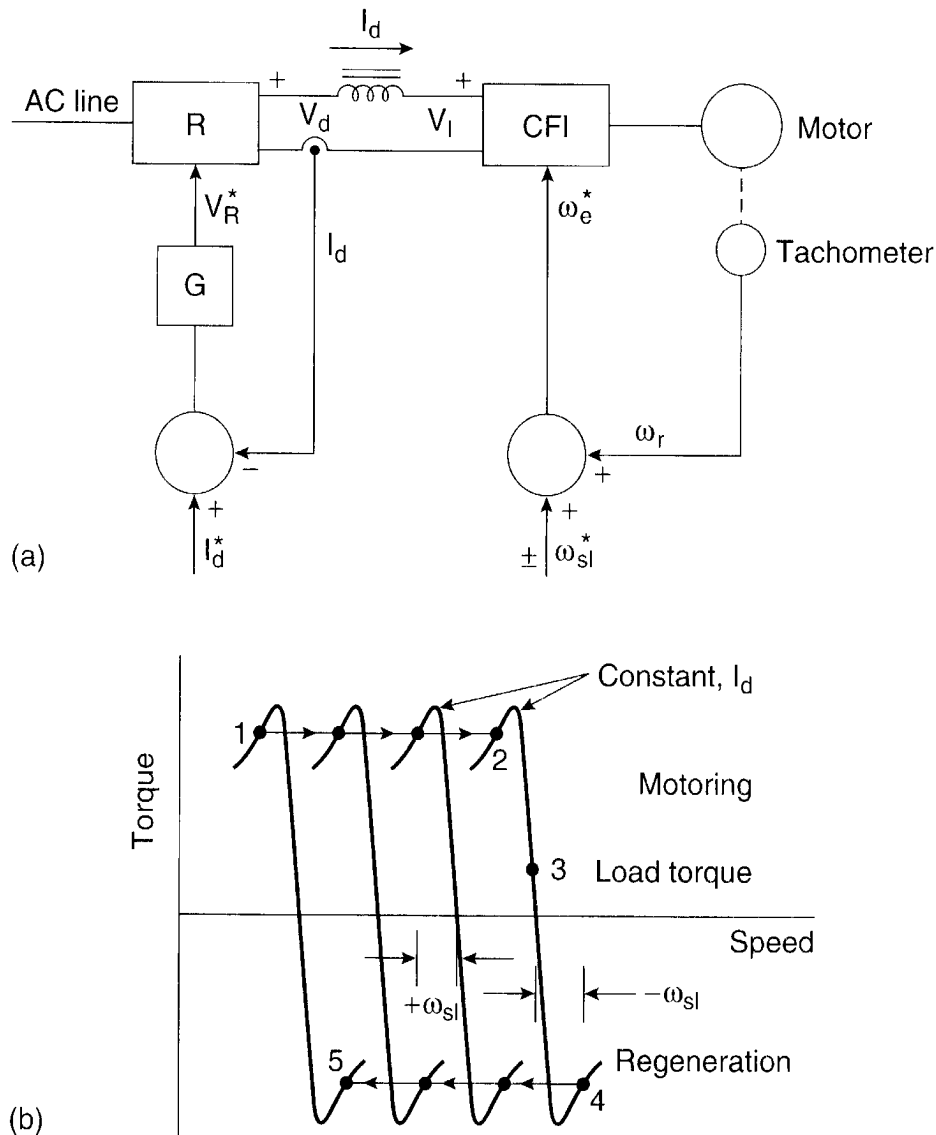


**Figure 8.16** (a) Independent current and slip control, (b) Torque-speed characteristics for acceleration and deceleration

### 8.3.2.2 Speed and Flux Control in Current-Fed Inverter Drive

A practical and much improved scalar control technique of a current-fed inverter drive is shown in Figure 8.17. Here, the speed control loop controls the torque by slip control as usual, but it also controls the current  $I_d^*$  through a pre-computed function generator to maintain a constant flux. At zero slip, the developed torque is zero, but the current has a minimum value that corresponds to the magnetizing current of the machine. The slip becomes negative in regenerative mode, but the  $I_d^* - \omega_{sl}^*$  relation is symmetrical with the motoring mode. The open loop, pre-programmed  $I_d^*$  control is satisfactory, but it has one disadvantage: machine flux may vary with parameter variation. An independent flux control loop outside the current control loop, as indicated in Figure 8.12, can be provided for tighter flux control.

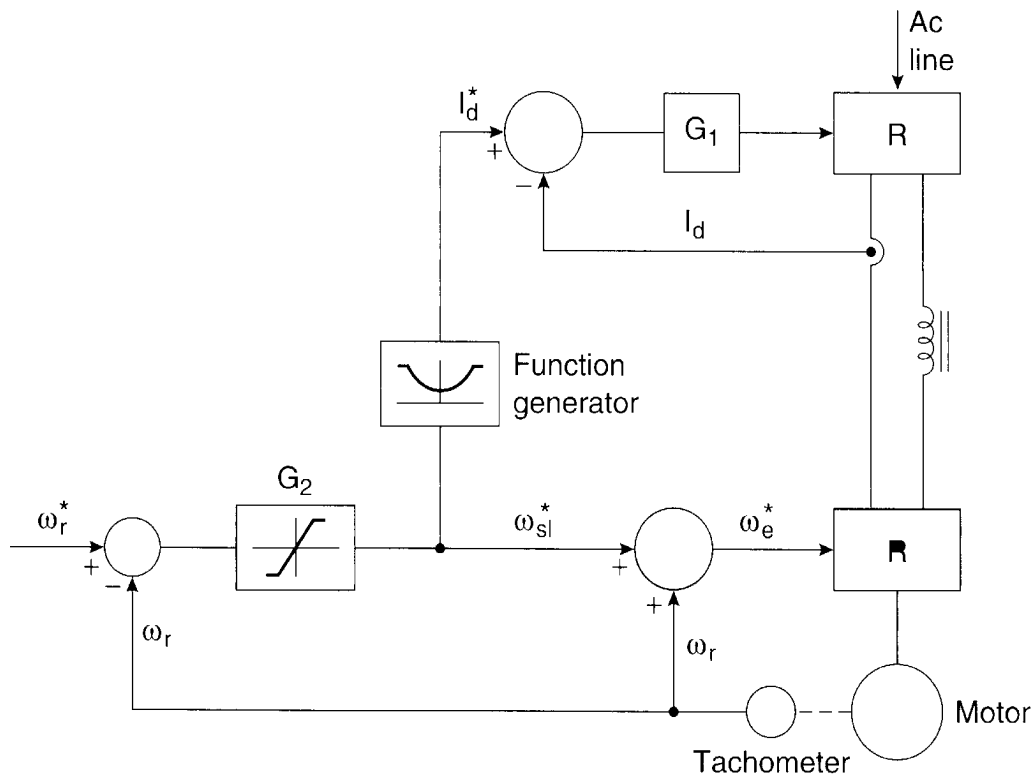


**Figure 8.17** Current-fed inverter drive with speed and flux control

### 8.3.2.3 Volts/Hz Control of Current-Fed Inverter Drive

As the current control mode of a voltage-fed inverter is possible, similarly, a current-fed inverter can also be controlled in voltage-fed mode. Figure 8.18 shows a volts/Hz-controlled drive with a current-fed inverter. In such a case, the features of a current-fed inverter, such as easy regeneration to the line and immunity to the shoot-through fault, can be retained. The command frequency  $\omega_e^*$  operates directly on the inverter as usual. The voltage command  $V_s^*$ , generated from  $\omega_e^*$  through the volts/Hz function generator, is compared with the machine terminal voltage. The resulting error controls the dc link current  $I_d$  in the inner loop, as shown. As the machine speed is increased by ramping up the frequency command, the current  $I_d$  changes to match the desired voltage. The drive goes to regenerative mode when the frequency command is ramped down. A particular advantage in the control strategy is that the fluctuation of the line voltage does not affect the machine flux because the current loop makes the desired correction.

### 8.3.3 Efficiency Optimization Control by Flux Program

Machines are normally operated at rated flux, as mentioned before, so that the developed torque/amp is high and transient response is fast. Industrial drives usually operate at light loads most of the time. If rated flux is maintained at a light load, it can be shown that the core loss (function of flux and frequency) is excessive, giving poor efficiency of the drive. For a certain steady-state, light-load torque condition and at a certain speed, the typical distribution of losses in a converter-machine system and its variation with a variation of flux is shown in Figure 8.19. As the flux  $\psi_r$  is reduced from the rated value, the core loss decreases, but the machine copper loss

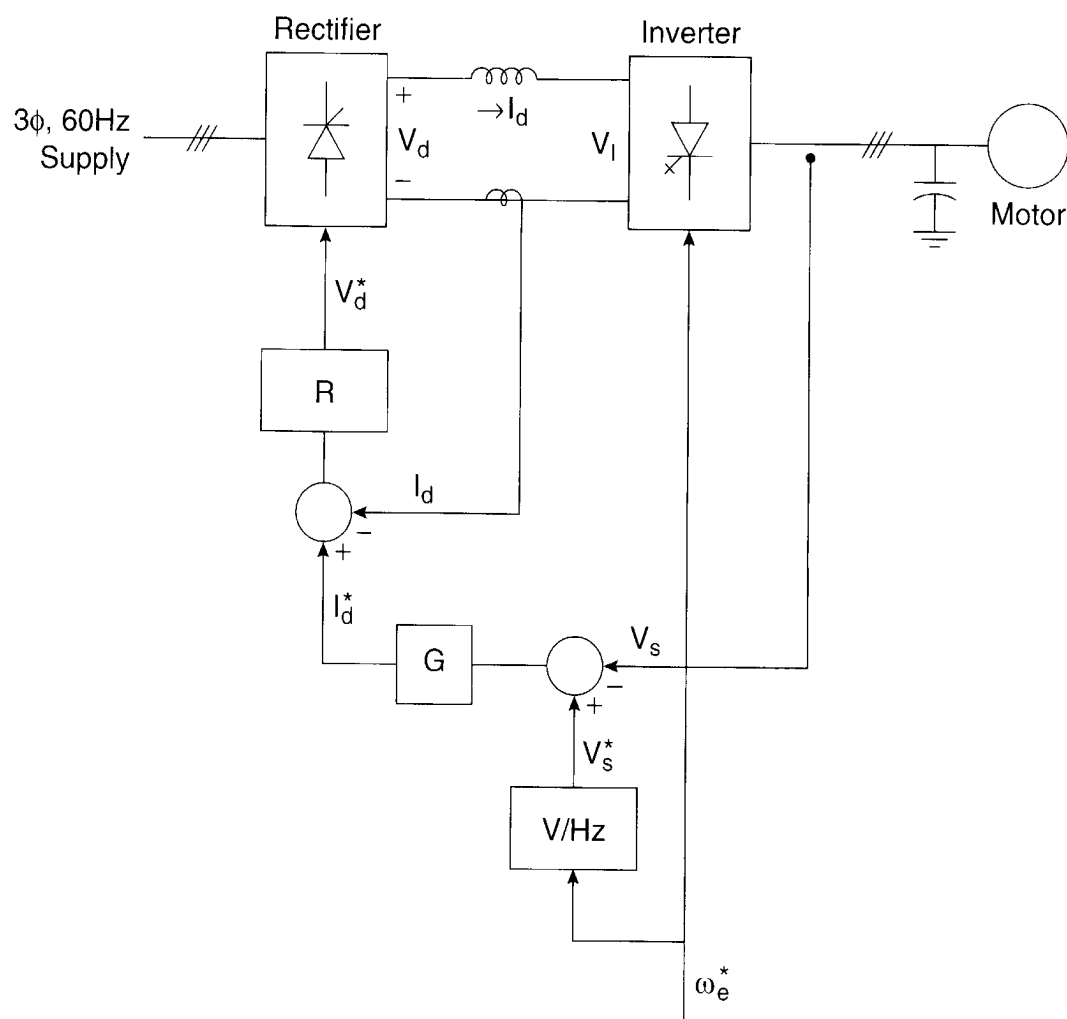


**Figure 8.18** Volts/Hz control of current-fed GTO PWM inverter drive

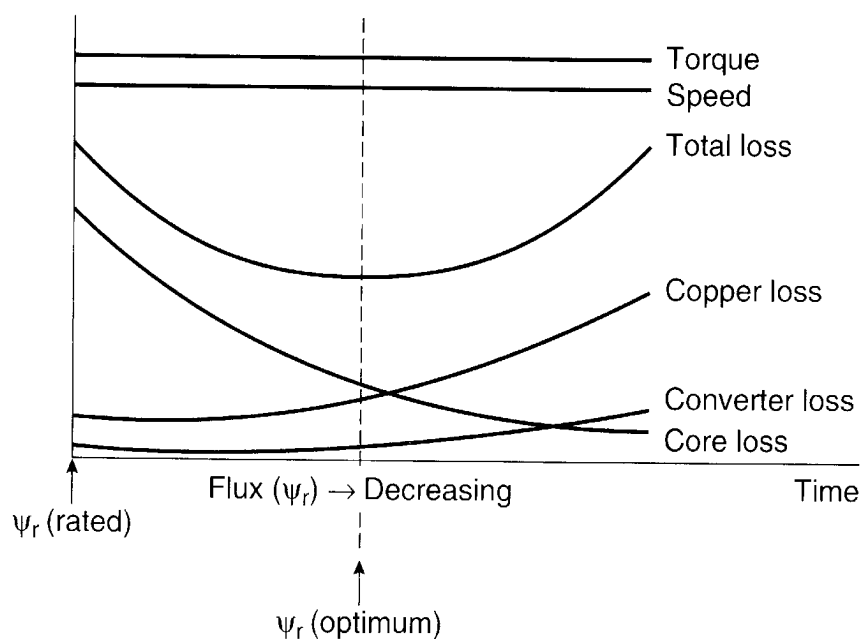


**Figure 8.19** Loss variation of converter-machine system with varying flux

and converter losses increase. However, the total loss decreases to a minimum value and then increases again. It is desirable to set the rotor flux at  $\psi_r$  (optimum) so that the converter-machine system efficiency is optimum. Figure 8.20 shows the typical optimum flux program for variable torque and constant speed, and compares the corresponding efficiency with that of the rated flux. The flux program is symmetrical for motoring and regenerative torque conditions. Note that at the rated torque, the flux should be at rated value and there is no efficiency improvement. The incremental efficiency improvement becomes larger as the torque is reduced. Figure 8.12 incorporates a similar flux program for efficiency optimization. With full commanded torque  $T_e^*$ , the rated flux is established for fast acceleration, but at steady-state, light load, the flux is reduced for efficiency improvement. Since core loss is also influenced by speed (i.e., frequency), the flux program should vary with the variation of speed. Figure 8.21 shows the simulation result of a 5 hp drive's efficiency improvement by using flux programs at three different speeds. Normally, a machine is designed to operate at best efficiency at the rated torque and speed (corner point). The efficiency decreases as speed and/or torque decrease. However, at a certain speed, the incremental efficiency improvement at light load can be substantial by flux programming. Note that Figure 8.21 shows efficiency curves for the total converter-machine system.

Figure 8.22 shows the open loop volts/Hz program for the optimum flux programming control of a pump-type drive, where the load torque as a function of speed is given in the figure. At each speed, the load torque is known and the corresponding optimum flux is shown in the figure. The flux determines the applied voltage. The drive starts with a rated flux and then settles down in the operating range where the optimum flux program is valid. Commercial drives with volts/Hz control are often available with a selectable volts/Hz program for efficiency optimization control. A more advanced method of efficiency optimization control by an on-line search method will be discussed in Chapter 11.

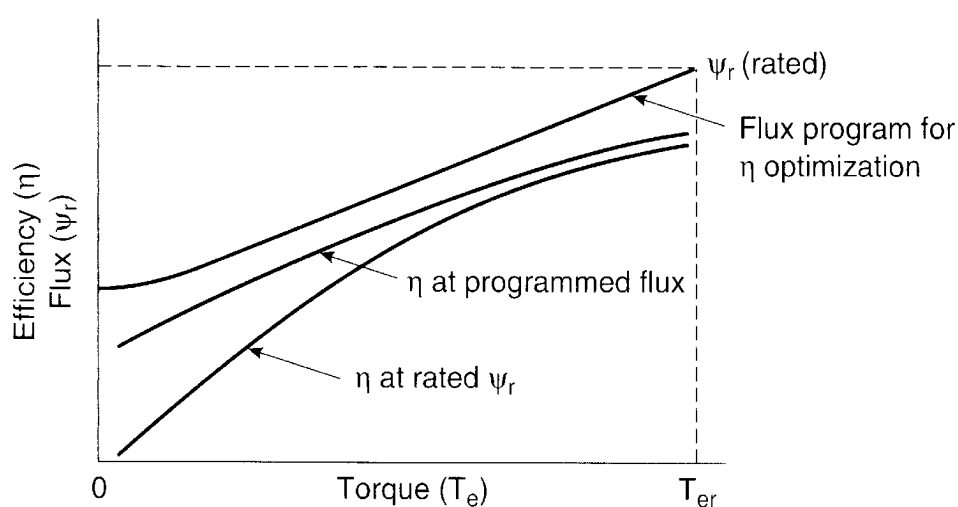


**Figure 8.20** Efficiency improvement by flux program at variable torque but constant speed

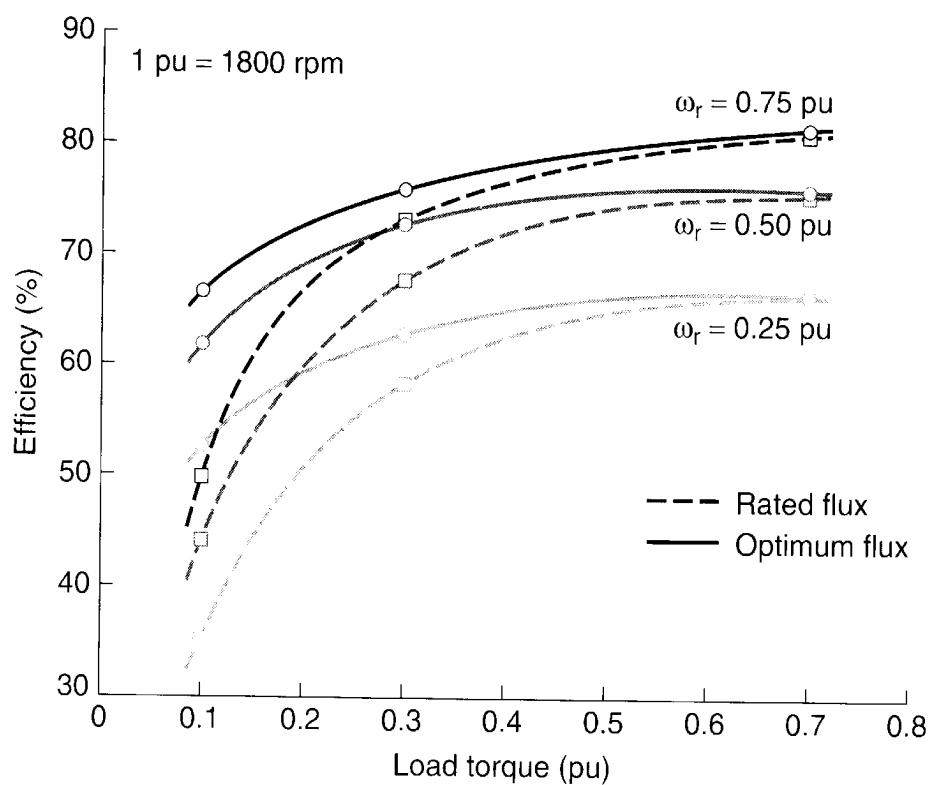


**Figure 8.21** Efficiency improvement by flux program at variable torque and different speeds

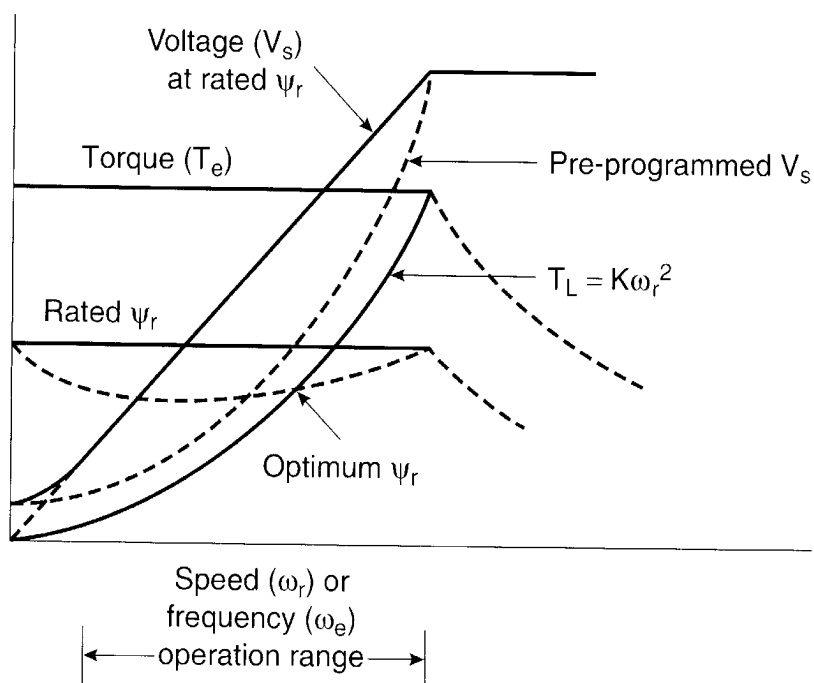


**Figure 8.22** Open loop volts/Hz program for optimal efficiency for pump load

## 8.4 VECTOR OR FIELD-ORIENTED CONTROL

So far, we have discussed scalar control techniques of voltage-fed and current-fed inverter drives. Scalar control is somewhat simple to implement, but the inherent coupling effect (i.e., both torque and flux are functions of voltage or current and frequency) gives sluggish response and the system is easily prone to instability because of a high-order (fifth-order) system effect. To make it more clear, if, for example, the torque is increased by incrementing the slip (i.e., the frequency), the flux tends to decrease. Note that the flux variation is always sluggish. The flux decrease is then compensated by the sluggish flux control loop feeding in additional voltage. This temporary dipping of flux reduces the torque sensitivity with slip and lengthens the response time. This explanation is also valid for current-fed inverter drives.

The foregoing problems can be solved by vector or field-oriented control. The invention of vector control in the beginning of 1970s, and the demonstration that an induction motor can be controlled like a separately excited dc motor, brought a renaissance in the high-performance control of ac drives. Because of dc machine-like performance, vector control is also known as decoupling, orthogonal, or transvector control. Vector control is applicable to both induction and synchronous motor drives, and the latter will be discussed in Chapter 9. Undoubtedly, vector control and the corresponding feedback signal processing, particularly for modern sensorless vector control, are complex and the use of powerful microcomputer or DSP is mandatory. It appears that eventually, vector control will oust scalar control, and will be accepted as the industry-standard control for ac drives.

### 8.4.1 DC Drive Analogy

Ideally, a vector-controlled induction motor drive operates like a separately excited dc motor drive, as mentioned above. Figure 8.23 explains this analogy. In a dc machine, neglecting the armature reaction effect and field saturation, the developed torque is given by

$$T_e = K_t' I_a I_f \quad (8.18)$$

where  $I_a$  = armature current and  $I_f$  = field current. The construction of a dc machine is such that the field flux  $\psi_f$  produced by the current  $I_f$  is perpendicular to the armature flux  $\psi_a$ , which is produced by the armature current  $I_a$ . These space vectors, which are stationary in space, are orthogonal or decoupled in nature. This means that when torque is controlled by controlling the current  $I_a$ , the flux  $\psi_f$  is not affected and we get the fast transient response and high torque/ampere ratio with the rated  $\psi_f$ . Because of decoupling, when the field current  $I_f$  is controlled, it affects the field flux  $\psi_f$  only, but not the  $\psi_a$  flux. Because of the inherent coupling problem, an induction motor cannot generally give such fast response.

DC machine-like performance can also be extended to an induction motor if the machine control is considered in a synchronously rotating reference frame ( $d^e$ - $q^e$ ), where the sinusoidal variables appear as dc quantities in steady state. In Figure 8.23(b), the induction motor with the inverter and vector control in the front end is shown with two control current inputs,  $i_{ds}^*$  and  $i_{qs}^*$ .



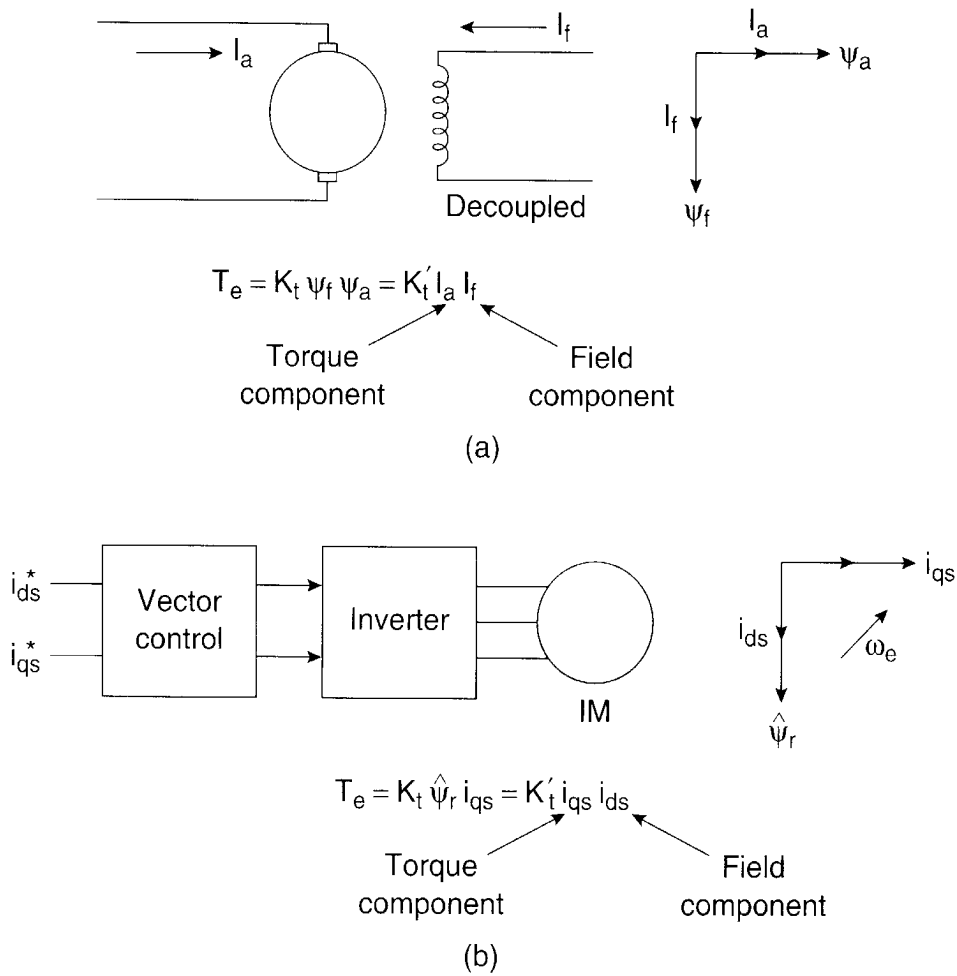


**Figure 8.23** (a) Separately excited dc motor, (b) Vector-controlled induction motor

These currents are the direct axis component and quadrature axis component of the stator current, respectively, in a synchronously rotating reference frame. With vector control,  $i_{ds}$  is analogous to field current  $I_f$  and  $i_{qs}$  is analogous to armature current  $I_a$  of a dc machine. Therefore, the torque can be expressed as

$$T_e = K_t \hat{\psi}_r i_{qs} \quad (8.19)$$

or

$$T_e = K'_t i_{ds} i_{qs} \quad (8.20)$$

where  $\hat{\psi}_r = \text{absolute } \bar{\psi}_r$  is the peak value of the sinusoidal space vector. This dc machine-like performance is only possible if  $i_{ds}$  is oriented (or aligned) in the direction of flux  $\hat{\psi}_r$  and  $i_{qs}$  is established perpendicular to it, as shown by the space-vector diagram on the right of Figure 8.23(b). This means that when  $i_{qs}^*$  is controlled, it affects the actual  $i_{qs}$  current only, but does not affect the flux  $\hat{\psi}_r$ . Similarly, when  $i_{ds}^*$  is controlled, it controls the flux only and does not affect the  $i_{qs}$  component of current. This vector or field orientation of currents is essential under all operating conditions in a vector-controlled drive. Note that when compared to dc machine space

vectors, induction machine space vectors rotate synchronously at frequency  $\omega_e$ , as indicated in the figure. In summary, vector control should assure the correct orientation and equality of command and actual currents.

### 8.4.2 Equivalent Circuit and Phasor Diagram

Let us now study the concept of vector orientation further with the help of equivalent circuit and phasor diagrams. Figure 8.24 shows the complex form of  $d^e$ - $q^e$  equivalent circuits in steady-state condition derived from Equations (2.109) and (2.110), where rms values  $V_s$  and  $I_s$  are replaced by corresponding peak values (sinusoidal vector variables), as shown. The rotor leakage inductance  $L_{lr}$  has been neglected for simplicity, which makes the rotor flux  $\hat{\psi}_r$  the same as the air gap flux  $\hat{\psi}_m$ . The stator current  $\hat{I}_s$  can be expressed as

$$\hat{I}_s = \sqrt{i_{ds}^2 + i_{qs}^2} \quad (8.21)$$

where  $i_{ds}$  = magnetizing component of stator current flowing through the inductance  $L_m$  and  $i_{qs}$  = torque component of stator current flowing in the rotor circuit. Figure 8.25 shows the phasor (or vector) diagrams in  $d^e$ - $q^e$  frame with peak values of sinusoids and air gap voltage  $\hat{V}_m$  aligned on the  $q^e$  axis. The phase position of the currents and flux is shown in the figure, and the corresponding developed torque expression is given by Equation (8.19). The terminal voltage  $\hat{V}_s$  is slightly leading because of the stator impedance drop. The in-phase or torque component of current  $i_{qs}$  contributes active power across the air gap, whereas the reactive or flux component of current  $i_{ds}$  contributes only reactive power. Figure 8.25(a) indicates an increase of the  $i_{qs}$  component of the stator current to increase the torque while maintaining the flux  $\psi_r$  constant, whereas (b) indicates a weakening of the flux by reducing the  $i_{ds}$  component. Note that although the operation is explained for the steady-state condition, the explanation is also valid for the transient condition in the  $qds$  equivalent circuit of Figure 2.24. After understanding the vector orientation principle, the next question is how to control the  $i_{ds}$  and  $i_{qs}$  components of stator current  $\hat{I}_s$  independently with the desired orientation. Instead of considering a cartesian form ( $i_{ds}$  and  $i_{qs}$ ) of control, it is also possible to consider control in a polar form ( $|I_s|$  and  $\theta$ ).

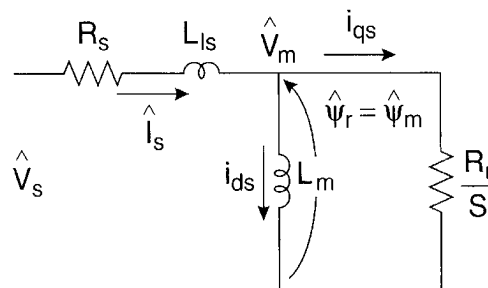


**Figure 8.24** Complex ( $qds$ ) equivalent circuit in steady state (rotor leakage inductance neglected)

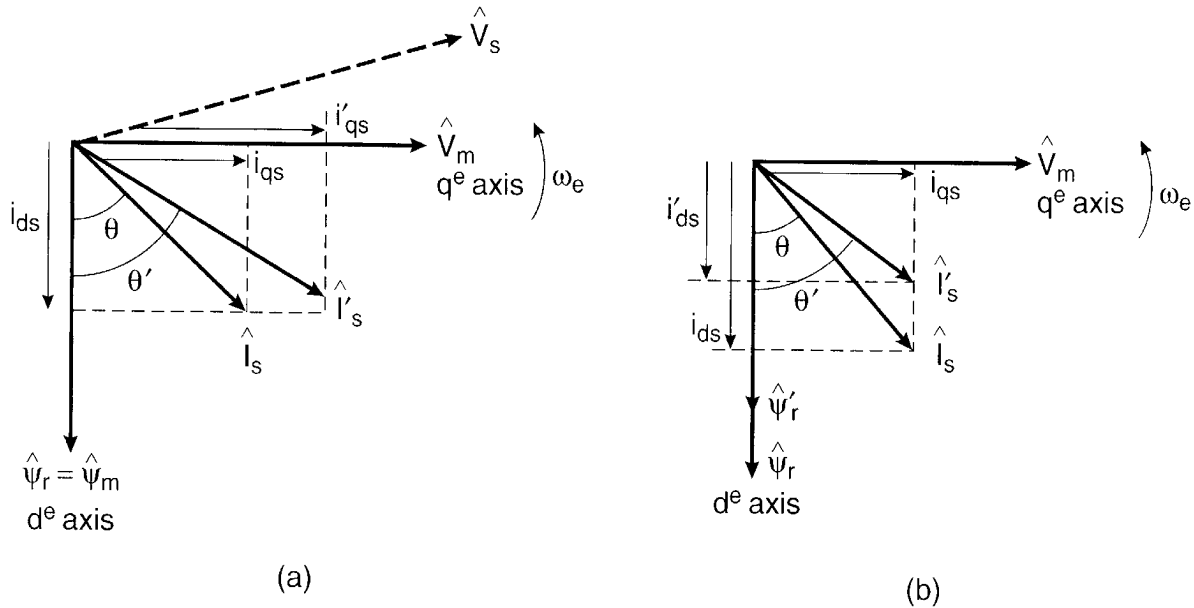


**Figure 8.25** Steady-state phasors (in terms of peak values) (a) Increase of torque component of current, (b) Increase of flux component of current

### 8.4.3 Principles of Vector Control

The fundamentals of vector control implementation can be explained with the help of Figure 8.26, where the machine model is represented in a synchronously rotating reference frame. The inverter is omitted from the figure, assuming that it has unity current gain, that is, it generates currents  $i_a$ ,  $i_b$ , and  $i_c$  as dictated by the corresponding command currents  $i_a^*$ ,  $i_b^*$ , and  $i_c^*$  from the controller. A machine model with internal conversions is shown on the right. The machine terminal phase currents  $i_a$ ,  $i_b$ , and  $i_c$  are converted to  $i_{ds}^s$  and  $i_{qs}^s$  components by  $3\phi/2\phi$  transformation. These are then converted to synchronously rotating frame by the unit vector

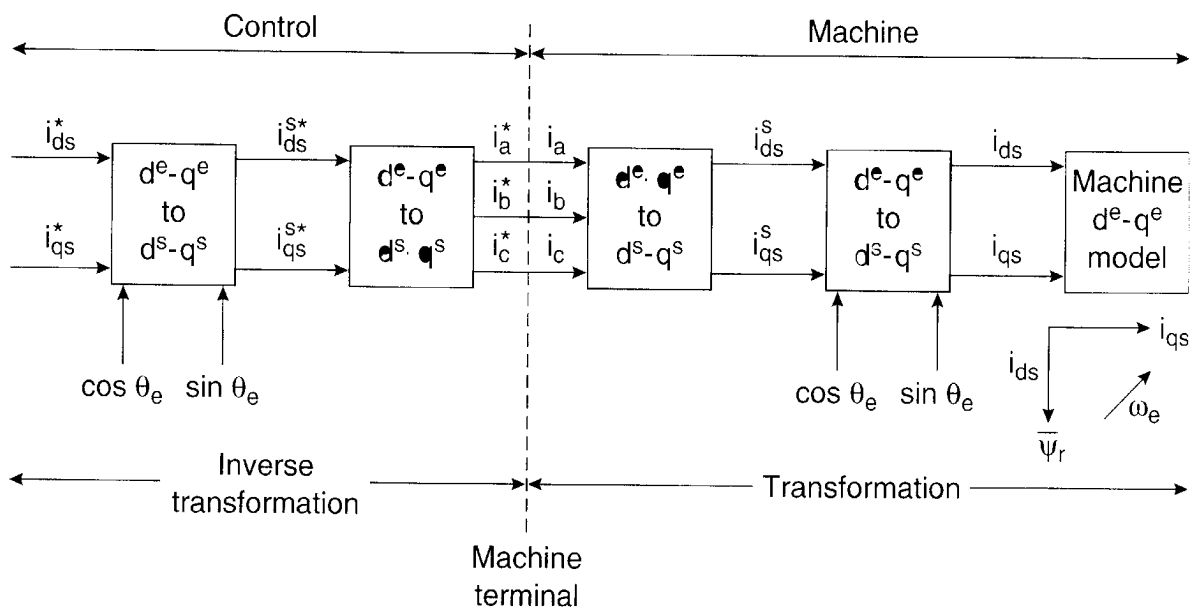


**Figure 8.26** Vector control implementation principle with machine  $d^e-q^e$  model

components  $\cos \theta_e$  and  $\sin \theta_e$  before applying them to the  $d^e$ – $q^e$  machine model as shown. The transformation equations are given in Chapter 2. The controller makes two stages of inverse transformation, as shown, so that the control currents  $i_{ds}^*$  and  $i_{qs}^*$  correspond to the machine currents  $i_{ds}$  and  $i_{qs}$ , respectively. In addition, the unit vector assures correct alignment of  $i_{ds}$  current with the flux vector  $\bar{\psi}_r$  and  $i_{qs}$  perpendicular to it, as shown. Note that the transformation and inverse transformation including the inverter ideally do not incorporate any dynamics, and therefore, the response to  $i_{ds}$  and  $i_{qs}$  is instantaneous (neglecting computational and sampling delays).

There are essentially two general methods of vector control. One, called the direct or feedback method, was invented by Blaschke [9], and the other, known as the indirect or feedforward method, was invented by Hasse [10]. The methods are different essentially by how the unit vector ( $\cos \theta_e$  and  $\sin \theta_e$ ) is generated for the control. It should be mentioned here that the orientation of  $i_{ds}$  with rotor flux  $\psi_r$ , air gap flux  $\psi_m$ , or stator flux ( $\psi_s$ ) is possible in vector control [11]. However, rotor flux orientation gives natural decoupling control, whereas air gap or stator flux orientation gives a coupling effect which has to be compensated by a decoupling compensation current. This is discussed later.

#### 8.4.4 Direct or Feedback Vector Control

The basic block diagram of the direct vector control method for a PWM voltage-fed inverter drive is shown in Figure 8.27. The principal vector control parameters,  $i_{ds}^*$  and  $i_{qs}^*$ , which are dc values in synchronously rotating frame, are converted to stationary frame (defined as vector rotation (VR)) with the help of a unit vector ( $\cos \theta_e$  and  $\sin \theta_e$ ) generated from flux vector signals  $\psi_{dr}^s$  and  $\psi_{qr}^s$ . The resulting stationary frame signals are then converted to phase current commands for the inverter. The flux signals  $\psi_{dr}^s$  and  $\psi_{qr}^s$  are generated from the machine terminal voltages and currents with the help of the voltage model estimator, which will be discussed later. A flux control loop has been added for precision control of flux. The torque component of current  $i_{qs}^*$  is generated from the speed control loop through a bipolar limiter (not shown). The torque, proportional to  $i_{qs}$  (with constant flux), can be bipolar. It is negative with negative  $i_{qs}$ , and correspondingly, the phase position of  $i_{qs}$  becomes negative in Figure 8.25. An additional torque control loop can be added within the speed loop, if desired. Figure 8.27 can be extended to field-weakening mode by programming the flux command as a function of speed so that the inverter remains in PWM mode. Vector control by current regulation is lost if the inverter attains the square-wave mode of operation.

The correct alignment of current  $i_{ds}$  in the direction of flux  $\hat{\psi}_r$  and the current  $i_{qs}$  perpendicular to it are crucial in vector control. This alignment, with the help of stationary frame rotor flux vectors  $\psi_{dr}^s$  and  $\psi_{qr}^s$ , is explained in Figure 8.28. In this figure, the  $d^e$ – $q^e$  frame is rotating at synchronous speed  $\omega_e$  with respect to stationary frame  $d^s$ – $q^s$ , and at any instant, the angular position of the  $d^e$ -axis with respect to the  $d^s$ -axis is  $\theta_e$ , where  $\theta_e = \omega_e t$ . From the figure, we can write the following equations:

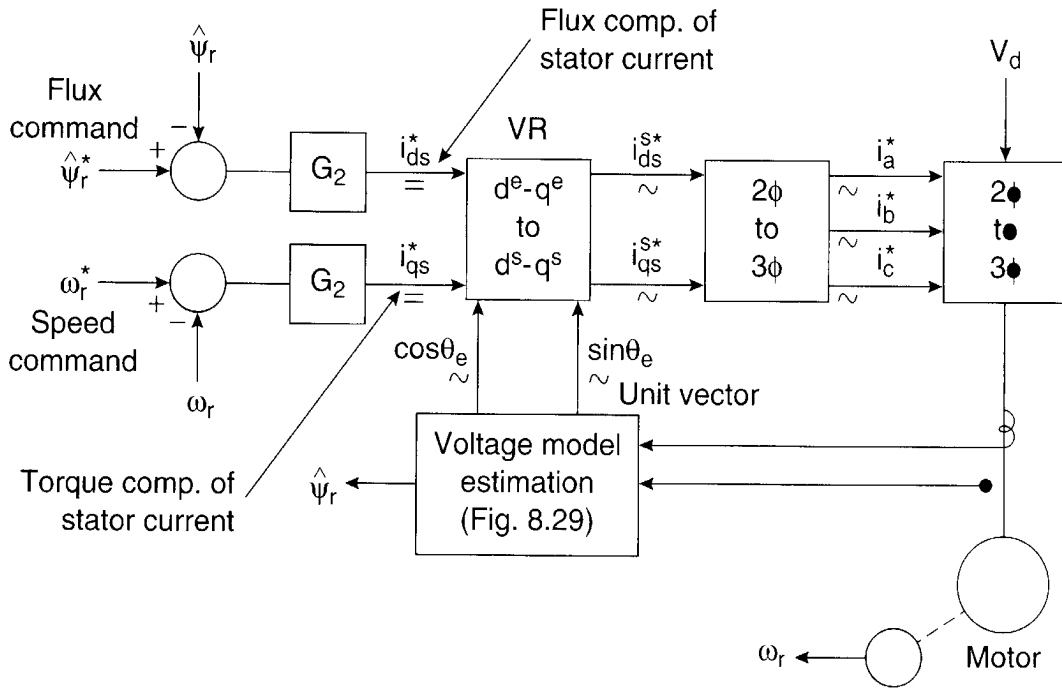


**Figure 8.27** Direct vector control block diagram with rotor flux orientation

$$\psi_{dr}^s = \hat{\psi}_r \cos\theta_e \quad (8.22)$$

$$\psi_{qr}^s = \hat{\psi}_r \sin\theta_e \quad (8.23)$$

In other words,

$$\cos\theta_e = \frac{\psi_{dr}^s}{\hat{\psi}_r} \quad (8.24)$$

$$\sin\theta_e = \frac{\psi_{qr}^s}{\hat{\psi}_r} \quad (8.25)$$

$$\hat{\psi}_r = \sqrt{\psi_{dr}^{s^2} + \psi_{qr}^{s^2}} \quad (8.26)$$

where vector  $\vec{\psi}_r$  is represented by magnitude  $\hat{\psi}_r$ . Signals  $\cos\theta_e$  and  $\sin\theta_e$  have been plotted in correct phase position in Figure 8.28(b). These unit vector signals, when used for vector rotation in Figure 8.27, give a ride of current  $i_{ds}$  on the  $d^e$ -axis (direction of  $\hat{\psi}_r$ ) and current  $i_{qs}$  on the  $q^e$ -axis as shown. At this condition,  $\psi_{qr} = 0$  and  $\psi_{dr} = \hat{\psi}_r$ , as indicated in the figure, and the corresponding torque expression is given by Equation (8.19) like a dc machine. When the  $i_{qs}$  polarity is reversed by the speed loop, the  $i_{qs}$  position in Figure 8.28(a) also reverses, giving negative torque. The generation of a unit vector signal from feedback flux vectors gives the name “direct vector control.”



the speed. At zero speed, the phase sequence of the unit vector automatically reverses, giving reverse motoring operation.

### 8.4.5 Flux Vector Estimation

In the direct vector control method, as discussed above, it is necessary to estimate the rotor flux components  $\psi_{dr}^s$  and  $\psi_{qr}^s$  so that the unit vector and rotor flux can be calculated by Equations (8.24)–(8.26). Two commonly used methods of flux estimation are discussed below.

#### 8.4.5.1 Voltage Model

In this method, the machine terminal voltages and currents are sensed and the fluxes are computed from the stationary frame ( $d^s$ - $q^s$ ) equivalent circuit shown in Figure 2. 27. These equations are:

$$i_{qs}^s = \frac{2}{3}i_a - \frac{1}{3}i_b - \frac{1}{3}i_c = i_a \quad (8.27)$$

$$i_{ds}^s = -\frac{1}{\sqrt{3}}i_b + \frac{1}{\sqrt{3}}i_c \quad (8.28)$$

$$= -\frac{1}{\sqrt{3}}(i_a + 2i_b) \quad (8.29)$$

since  $i_c = -(i_a + i_b)$  for isolated neutral load.

$$v_{qs}^s = \frac{2}{3}v_a - \frac{1}{3}v_b - \frac{1}{3}v_c \quad (2.72)$$

$$= \frac{1}{3}(v_{ab} + v_{ac}) \quad (8.30)$$

$$v_{ds}^s = -\frac{1}{\sqrt{3}}v_b + \frac{1}{\sqrt{3}}v_c \quad (2.73)$$

$$= -\frac{1}{\sqrt{3}}v_{bc} \quad (8.31)$$

$$\psi_{ds}^s = \int (v_{ds}^s - R_s i_{ds}^s) dt \quad (8.32)$$

$$\psi_{qs}^s = \int (v_{qs}^s - R_s i_{qs}^s) dt \quad (8.33)$$

$$\hat{\psi}_s = \sqrt{\psi_{ds}^{s^2} + \psi_{qs}^{s^2}} \quad (8.34)$$

$$\psi_{dm}^s = \psi_{ds}^s - L_{ls} i_{ds}^s = L_m (i_{ds}^s + i_{dr}^s) \quad (8.35)$$

$$\psi_{qm}^s = \psi_{qs}^s - L_{ls} i_{qs}^s = L_m (i_{qs}^s + i_{qr}^s) \quad (8.36)$$

$$\psi_{dr}^s = L_m i_{ds}^s + L_r i_{dr}^s \quad (8.37)$$

$$\psi_{qr}^s = L_m i_{qs}^s + L_r i_{qr}^s \quad (8.38)$$

Eliminating  $i_{dr}^s$  and  $i_{qr}^s$  from Equations (8.37)–(8.38) with the help of Equations (8.35)–(8.36), respectively, gives the following:

$$\psi_{dr}^s = \frac{L_r}{L_m} \psi_{dm}^s - L_{lr} i_{ds}^s \quad (8.39)$$

$$\psi_{qr}^s = \frac{L_r}{L_m} \psi_{qm}^s - L_{lr} i_{qs}^s \quad (8.40)$$

which can also be written in the following form with the help of Equations (8.35) and (8.36):

$$\psi_{dr}^s = \frac{L_r}{L_m} (\psi_{ds}^s - \sigma L_s i_{ds}^s) \quad (8.41)$$

$$\psi_{qr}^s = \frac{L_r}{L_m} (\psi_{qs}^s - \sigma L_s i_{qs}^s) \quad (8.42)$$

where  $\sigma = 1 - L_m^2 / L_r L_s$ .

Substituting Equations (8.39)–(8.40) in the torque equation (2.113), in stationary frame and simplifying, we get

$$T_e = \frac{3}{2} \left( \frac{P}{2} \right) \frac{L_m}{L_r} (\psi_{dr}^s i_{qs}^s - \psi_{qr}^s i_{ds}^s) \quad (8.43)$$

Figure 8.29 shows the block diagram for feedback signal estimation with the help of a microcomputer, where the estimation of additional signals, such as stator fluxes, air gap fluxes, and torque, are also shown. In the front end, there is some hardware low-pass filtering and  $3\phi/2\phi$  conversion with the help of op amps before conversion by the A/D converter, which is not shown in detail. Note that machines are normally isolated neutral load, and therefore, only two current sensors are needed. The vector drive uses a current-controlled PWM inverter. The current control is logical, as mentioned before, because both the flux and torque are directly related to currents. The inverter can have hysteresis-band current control, or some type of voltage control within the current control loop (such as synchronous current control, as discussed in Figure



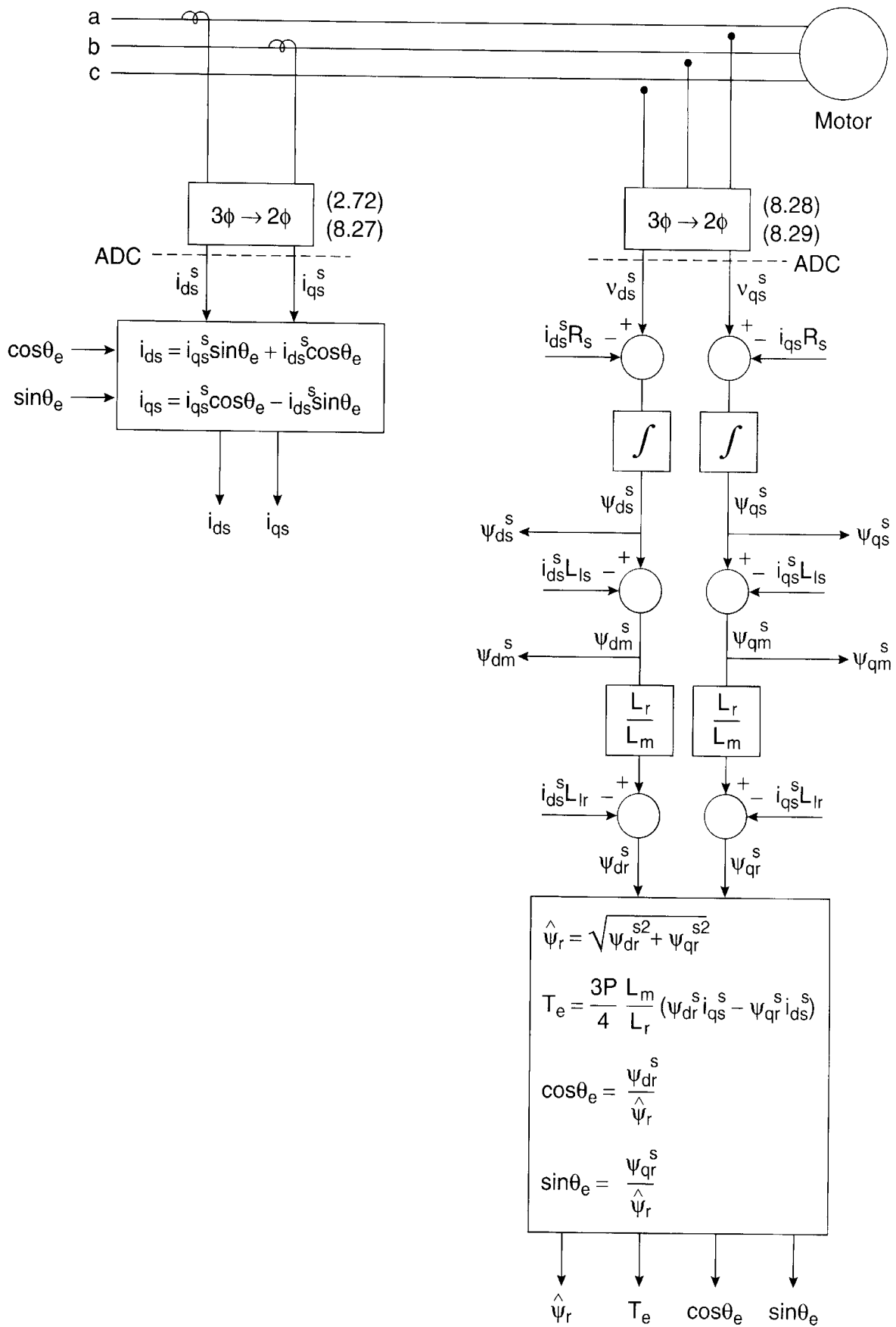


**Figure 8.29** Voltage model feedback signal estimation block diagram

8.34). The current estimation equations for  $i_{ds}$  and  $i_{qs}$  using Equations (2.74)–(2.75) are also included in Figure 8.29. Note that any error in the unit vector or distortion associated with the feedback signals will affect the performance of the drive.

The direct method of vector control discussed so far is difficult to operate successfully at very low frequency (including zero speed) because of the following problems:

- At low frequency, voltage signals  $v_{ds}^s$  and  $v_{qs}^s$  are very low. In addition, ideal integration becomes difficult because dc offset tends to build up at the integrator output.
- The parameter variation effect of resistance  $R_s$  and inductances  $L_{ls}$ ,  $L_{lr}$ , and  $L_m$  tend to reduce accuracy of the estimated signals. Particularly, temperature variation of  $R_s$  becomes more dominant. However, compensation of  $R_s$  is somewhat easier, which will be discussed later. At higher voltage, the effect of parameter variation can be neglected.

In industrial applications, vector drives are often required to operate from zero speed (including zero speed start-up). Here, direct vector control with voltage model signal estimation cannot be used.

#### 8.4.5.2 Current Model

In the low-speed region, the rotor flux components can be synthesized more easily with the help of speed and current signals. The rotor circuit equations of  $d^s$ - $q^s$  equivalent circuits (Figure 2.27) can be given as

$$\frac{d\psi_{dr}^s}{dt} + R_r i_{dr}^s + \omega_r \psi_{qr}^s = 0 \quad (8.44)$$

$$\frac{d\psi_{qr}^s}{dt} + R_r i_{qr}^s - \omega_r \psi_{dr}^s = 0 \quad (8.45)$$

Adding terms  $(L_m R_r / L_r) i_{ds}^s$  and  $(L_m R_r / L_r) i_{qs}^s$ , respectively, on both sides of the above equations, we get

$$\frac{d\psi_{dr}^s}{dt} + \frac{R_r}{L_r} (L_m i_{ds}^s + L_r i_{dr}^s) + \omega_r \psi_{qr}^s = \frac{L_m R_r}{L_r} i_{ds}^s \quad (8.46)$$

$$\frac{d\psi_{qr}^s}{dt} + \frac{R_r}{L_r} (L_m i_{qs}^s + L_r i_{qr}^s) - \omega_r \psi_{dr}^s = \frac{L_m R_r}{L_r} i_{qs}^s \quad (8.47)$$

Substituting Equations (8.37) and (8.38), respectively, and simplifying, we get

$$\frac{d\psi_{dr}^s}{dt} = \frac{L_m}{T_r} i_{ds}^s - \omega_r \psi_{qr}^s - \frac{1}{T_r} \psi_{dr}^s \quad (8.48)$$

$$\frac{d\psi_{qr}^s}{dt} = \frac{L_m}{T_r} i_{qs}^s + \omega_r \psi_{dr}^s - \frac{1}{T_r} \psi_{qr}^s \quad (8.49)$$

where  $T_r = L_r/R_r$  is the rotor circuit time constant. Equations (8.48) and (8.49) give rotor fluxes as functions of stator currents and speed. Therefore, knowing these signals, the fluxes and corresponding unit vector signals can be estimated. These equations are defined as the current model for flux estimation, which was originally formulated by Blaschke (often called Blaschke equation). It is shown in block diagram form in Figure 8.30, where the estimation of the  $\hat{\psi}_r$ ,  $\cos \theta_e$ , and  $\sin \theta_e$  signals are shown on the right. Other feedback signals, such as  $T_e$ ,  $i_{ds}$ , and  $i_{qs}$ , as well as stator and air gap fluxes, indicated in Figure 8.29, can easily be estimated from the current model. Flux estimation by this model requires a speed encoder, but the advantage is that the drive operation can be extended down to zero speed. However, note that the estimation accuracy is affected by the variation of machine parameters. Particularly, the rotor resistance variation (may be more than 50 percent) becomes dominant by temperature and skin effect. Compensation of this parameter is difficult because of inaccessibility.

Since the voltage model flux estimation is better at higher speed ranges, whereas the current model estimation can be made at any speed, it is possible to have a hybrid model [14].

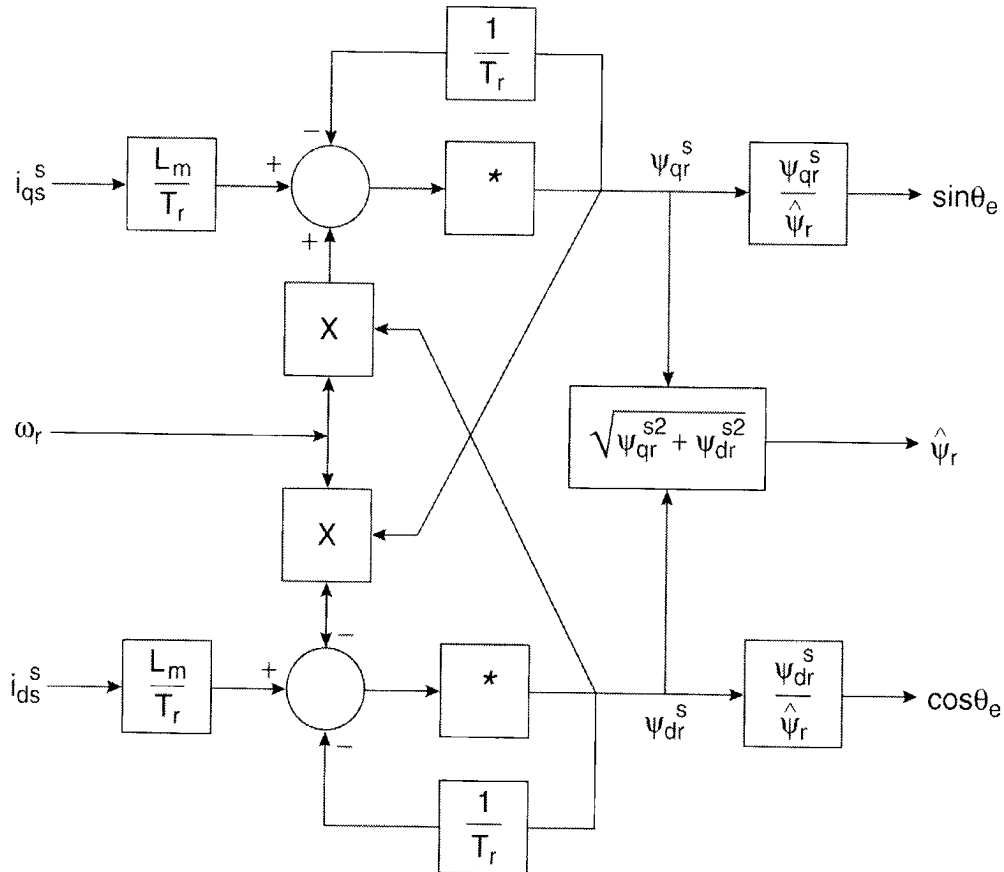


**Figure 8.30** Current model (Blaschke equation) flux estimation

where the voltage model becomes effective at higher speed ranges, but transitions smoothly to the current model at lower speed ranges.

#### 8.4.6 Indirect or Feedforward Vector Control

The indirect vector control method is essentially the same as direct vector control, except the unit vector signals ( $\cos \theta_e$  and  $\sin \theta_e$ ) are generated in feedforward manner. Indirect vector control is very popular in industrial applications. Figure 8.31 explains the fundamental principle of indirect vector control with the help of a phasor diagram. The  $d^s$ - $q^s$  axes are fixed on the stator, but the  $d^r$ - $q^r$  axes, which are fixed on the rotor, are moving at speed  $\omega_r$  as shown. Synchronously rotating axes  $d^e$ - $q^e$  are rotating ahead of the  $d^r$ - $q^r$  axes by the positive slip angle  $\theta_{sl}$  corresponding to slip frequency  $\omega_{sl}$ . Since the rotor pole is directed on the  $d^e$  axis and  $\omega_e = \omega_r + \omega_{sl}$ , we can write

$$\theta_e = \int \omega_e dt = \int (\omega_r + \omega_{sl}) dt = \theta_r + \theta_{sl} \quad (8.50)$$

Note that the rotor pole position is not absolute, but is slipping with respect to the rotor at frequency  $\omega_{sl}$ . The phasor diagram suggests that for decoupling control, the stator flux component of current  $i_{ds}$  should be aligned on the  $d^e$  axis, and the torque component of current  $i_{qs}$  should be on the  $q^e$  axis, as shown.

For decoupling control, we can now make a derivation of control equations of indirect vector control with the help of  $d^e$ - $q^e$  equivalent circuits (Figure 2.23). The rotor circuit equations can be written as

$$\frac{d\psi_{dr}}{dt} + R_r i_{dr} - (\omega_e - \omega_r) \psi_{qr} = 0 \quad (8.51)$$

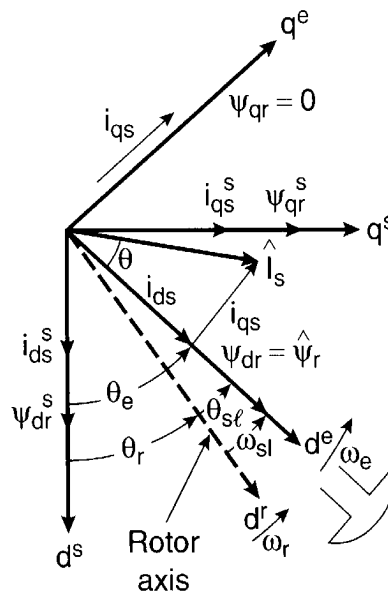


**Figure 8.31** Phasor diagram explaining indirect vector control

$$\frac{d\psi_{qr}}{dt} + R_r i_{qr} + (\omega_e - \omega_r) \psi_{dr} = 0 \quad (8.52)$$

The rotor flux linkage expressions can be given as

$$\psi_{dr} = L_r i_{dr} + L_m i_{ds} \quad (8.53)$$

$$\psi_{qr} = L_r i_{qr} + L_m i_{qs} \quad (8.54)$$

From the above equations, we can write

$$i_{dr} = \frac{1}{L_r} \psi_{dr} - \frac{L_m}{L_r} i_{ds} \quad (8.55)$$

$$i_{qr} = \frac{1}{L_r} \psi_{qr} - \frac{L_m}{L_r} i_{qs} \quad (8.56)$$

The rotor currents in Equations (8.51) and (8.52), which are inaccessible, can be eliminated with the help of Equations (8.55) and (8.56) as

$$\frac{d\psi_{dr}}{dt} + \frac{R_r}{L_r} \psi_{dr} - \frac{L_m}{L_r} R_r i_{ds} - \omega_{sl} \psi_{qr} = 0 \quad (8.57)$$

$$\frac{d\psi_{qr}}{dt} + \frac{R_r}{L_r} \psi_{qr} - \frac{L_m}{L_r} R_r i_{qs} + \omega_{sl} \psi_{dr} = 0 \quad (8.58)$$

where  $\omega_{sl} = \omega_e - \omega_r$  has been substituted.

For decoupling control, it is desirable that

$$\psi_{qr} = 0 \quad (8.59)$$

that is,

$$\frac{d\psi_{qr}}{dt} = 0 \quad (8.60)$$

so that the total rotor flux  $\hat{\psi}_r$  is directed on the  $d^e$  axis.

Substituting the above conditions in Equations (8.57) and (8.58), we get

$$\frac{L_r}{R_r} \frac{d\hat{\psi}_r}{dt} + \hat{\psi}_r = L_m i_{ds} \quad (8.61)$$

$$\omega_{sl} = \frac{L_m R_r}{\hat{\psi}_r L_r} i_{qs} \quad (8.62)$$

where  $\hat{\psi}_r = \psi_{dr}$  has been substituted.

If rotor flux  $\hat{\psi}_r = \text{constant}$ , which is usually the case, then from Equation (8.61),

$$\hat{\psi}_r = L_m i_{ds} \quad (8.63)$$

In other words, the rotor flux is directly proportional to current  $i_{ds}$  in steady state.

To implement the indirect vector control strategy, it is necessary to take Equations (8.50), (8.61), and (8.62) into consideration. Figure 8.32 shows a four-quadrant position servo system using the indirect vector control method. The power circuit consists of a front-end diode rectifier and a PWM inverter with a dynamic brake in the dc link. A hysteresis-band current control PWM is shown, but synchronous current control voltage PWM (see Figure 8.34) can also be used. The speed control loop generates the torque component of current  $i_{qs}^*$ , as usual. The flux component of current  $i_{ds}^*$  for the desired rotor flux  $\hat{\psi}_r$  is determined from Equation (8.63), and is maintained constant here in the open loop manner for simplicity. The variation of magnetizing inductance  $L_m$  will cause some drift in the flux. The slip frequency  $\omega_{sl}^*$  is generated from  $i_{qs}^*$  in feedforward manner from Equation (8.62) to satisfy the phasor diagram in Figure 8.31. The corresponding expression of slip gain  $K_s$  is given as

$$K_s = \frac{\omega_{sl}^*}{i_{qs}^*} = \frac{L_m R_r}{L_r \hat{\psi}_r} \quad (8.64)$$

Signal  $\omega_{sl}^*$  is added with speed signal  $\omega_r$  to generate frequency signal  $\omega_e$ . The unit vector signals  $\cos \theta_e$  and  $\sin \theta_e$  are then generated from  $\omega_e$  by integration and look-up tables, as indicated in the figure. The VR and  $2\phi/3\phi$  transformation are the same as in Figure 8.27. The speed signal from an incremental-position encoder is mandatory in indirect vector control because the slip signal locates the pole with respect to the rotor  $d^r$  axis in feedforward manner, which is moving at speed  $\omega_r$ . An absolute pole position on the rotor is not required in this case like a synchronous motor. If the polarity of  $i_{qs}^*$  becomes negative for negative torque, the phasor  $i_{qs}$  in Figure 8.31 will be reversed, and correspondingly,  $\omega_{sl}$  will be negative (i.e.,  $\theta_{sl}$  is negative), which will shift the rotor pole position ( $d^e$  axis) below the  $d^r$  axis. The speed control range in indirect vector control can easily be extended from stand-still (zero speed) to the field-weakening region. The addition of field-weakening control is shown by the dotted block diagram and the corresponding operation is explained in Figure 8.33. In this case, close loop flux control is necessary. In the constant torque region, the flux is constant. However, in the field-weakening region, the flux is programmed such that the inverter always operates in PWM mode, as explained before. The loss of torque and power for field-weakening vector control are indicated in the figure. The same principle of field-weakening control is also valid for direct vector control in Figure 8.27.

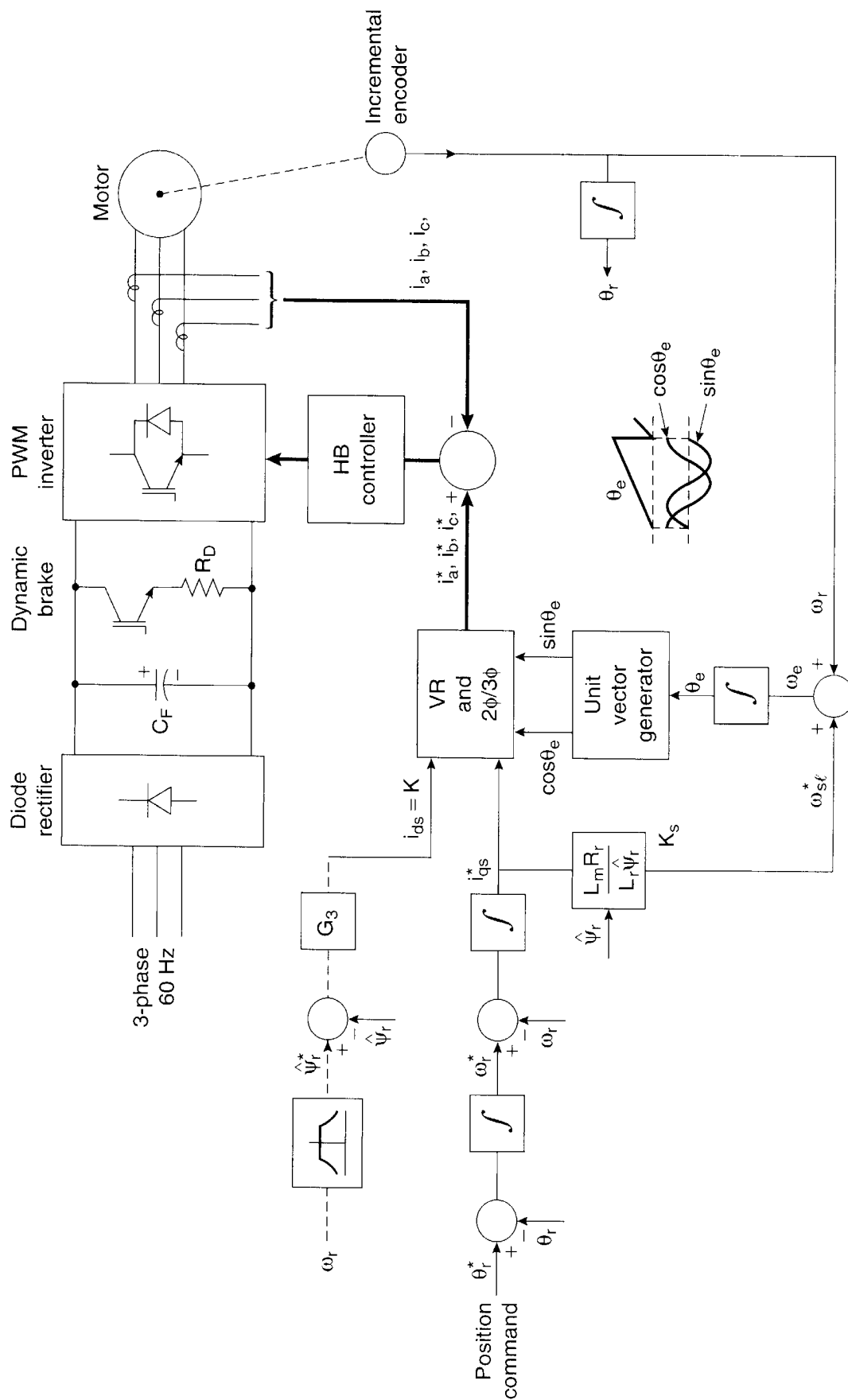
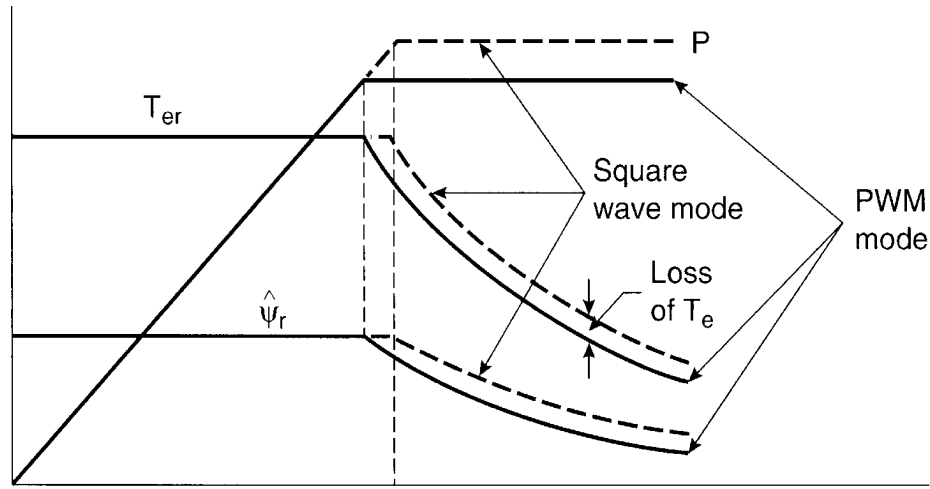


Figure 8.32 Indirect vector control block diagram with open loop flux control



**Figure 8.33** Torque-speed curves including field-weakening mode

In both the direct and indirect vector control methods discussed so far, instantaneous current control of the inverter is necessary. Hysteresis-band PWM current control can be used, as indicated in Figure 8.32, but its harmonic content is not optimum. Besides, at higher speeds, the current controller will tend to saturate in part of the cycle (quasi-PWM) because of higher CEMF. In this condition, the fundamental current magnitude and its phase will lose tracking with the command current, and thus, vector control will not be valid. These problems can be solved by synchronous current control (often called dc current control), which is shown in Figure 8.34. Command currents  $i_{ds}^*$  and  $i_{qs}^*$  in the vector control are compared with the respective  $i_{ds}$  and  $i_{qs}$  currents generated by the transformation of phase currents ( $3\phi/2\phi$  conversion and inverse vector rotation  $VR^{-1}$ ) with the help of the unit vector. The respective errors generate the voltage command signals  $v_{ds}^*$  and  $v_{qs}^*$  through the P-I compensators, as shown. These voltage commands are then converted into stationary frame phase voltages. The synchronous frame current control with a P-I controller assure amplitude and phase tracking of currents, even when the PWM controller goes into overmodulation range.

Of course, the introduction of feedback loops brings with it a small amount of coupling effect. To enhance the loop response, feedforward CEMF signals (see Figure 2.23) are injected in the respective loops. Signal  $\omega_e \psi_{ds}$  is added in the  $i_{qs}$  loop, whereas signal  $\omega_e \psi_{qs}$  subtracts from the  $i_{ds}$  loop signal. Often, the later signal is deleted. The block diagram for estimating the CEMF signals is added in the figure. The estimations of stator fluxes  $\psi_{ds}^s$  and  $\psi_{qs}^s$  are shown in Figure 8.29. The frequency signal  $\omega_e$  can be estimated as follows:

$$\cos \theta_e = \frac{\psi_{ds}^s}{\sqrt{\psi_{ds}^{s^2} + \psi_{qs}^{s^2}}} = \frac{\psi_{ds}^s}{\hat{\psi}_s} \quad (8.65)$$

$$\sin \theta_e^* = \frac{\psi_{qs}^s}{\hat{\psi}_s} \quad (8.66)$$



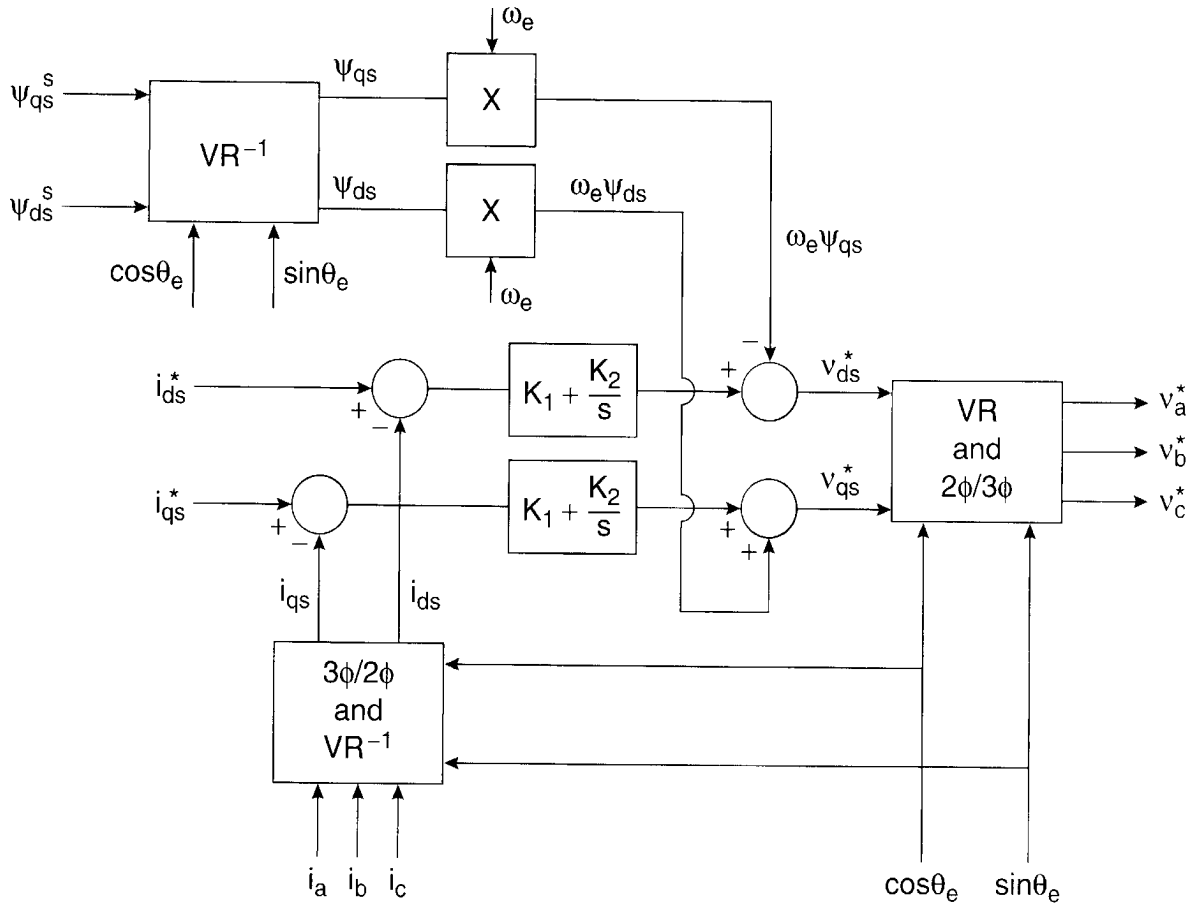


**Figure 8.34** Synchronous current control with feedforward CEMF compensation

$$\tan \theta_e^* = \frac{\psi_{qs}^s}{\psi_{ds}^s} \quad (8.67)$$

Differentiating Equation (8.67), we get

$$\sec^2 \theta_e \cdot \frac{d\theta_e^*}{dt} = \frac{\psi_{ds}^s \dot{\psi}_{qs}^s - \psi_{qs}^s \dot{\psi}_{ds}^s}{\psi_{ds}^s{}^2} \quad (8.68)$$

where

$$\sec^2 \theta_e = \frac{\hat{\psi}_s^2}{\psi_{ds}^s{}^2} \quad (8.69)$$

Substituting Equation (8.69) in Equation (8.68), we get

$$\omega_e = \frac{d\theta_e}{dt} = \frac{(v_{qs}^s - i_{qs}^s R_s) \psi_{ds}^s - (v_{ds}^s - i_{ds}^s R_s) \psi_{qs}^s}{\hat{\psi}_s^2} \quad (8.70)$$

where the voltage expressions behind the stator resistance drops have been substituted for the flux derivatives. Frequency  $\omega_e$  can also be derived as a function of the rotor fluxes by following a similar procedure.

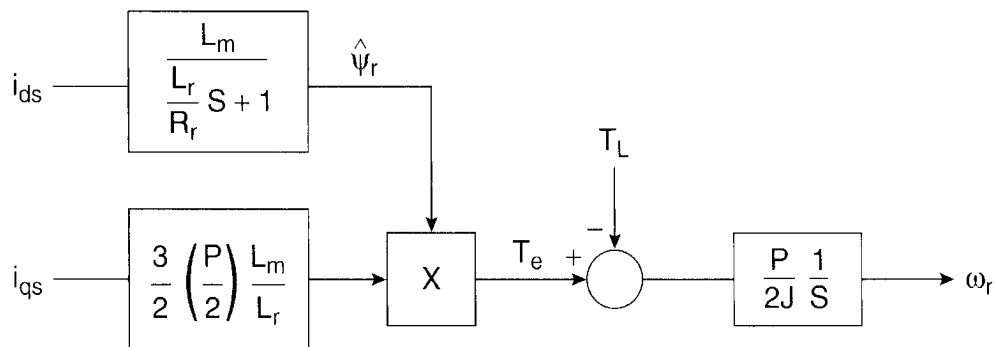
A dc machine-like electro-mechanical model of an ideal vector-controlled drive can be derived using Equation (8.61) and the following equations:

$$T_e = \frac{3}{2} \left( \frac{P}{2} \right) \frac{L_m}{L_r} \hat{\psi}_r i_{qs} \quad (8.71)$$

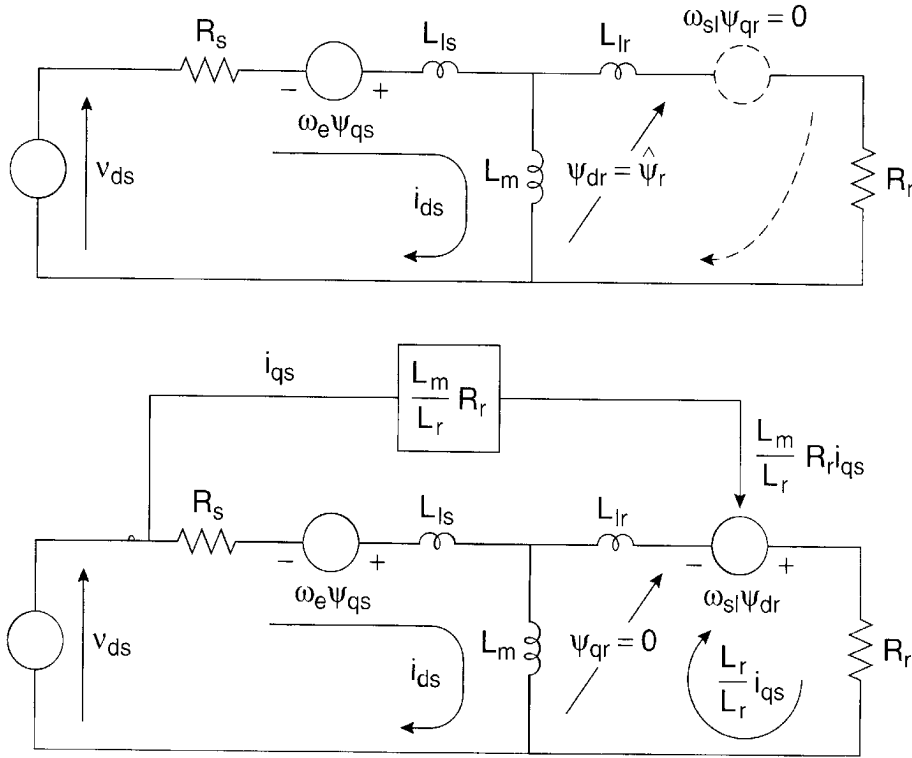
$$T_e - T_L = \left( \frac{2}{P} \right) J \frac{d\omega_r}{dt} \quad (2.105)$$

Figure 8.35 shows the corresponding transfer function block diagram, where the delay between the command and actual currents has been neglected. The developed torque  $T_e$  responds instantaneously with the current  $i_{qs}$ , but the flux response has first-order delay (with time constant  $L_r/R_r$ ), similar to a dc machine. It can be shown that direct vector control also has a similar transfer function model.

The physical principle of vector control can be understood more clearly with the help of the  $d^e$ - $q^e$  circuits shown in Figure 8.36. Since currents  $i_{ds}$  and  $i_{qs}$  are being controlled, ideally, the stator-side Thevenin impedance is infinity, that is, the stator-side circuit parameters and EMFs are of no consequence. With  $\psi_{qr} = 0$  under all conditions, EMF  $\omega_{sl} \psi_{qr} = 0$  in the  $d^e$  circuit. This indicates that at steady state, current  $i_{ds}$  will flow through the magnetizing branch only to establish the rotor flux  $\psi_r$ , but transiently, the current will be shared by the rotor circuit also and the time constant can be easily seen as  $L_r/R_r$ . In the  $q^e$  circuit, when torque is controlled



**Figure 8.35** Transfer function block diagram of vector-controlled drive



**Figure 8.36** Explanation of vector control with the help of  $d^e$ - $q^e$  circuits

by  $i_{qs}$ , EMF  $\omega_{sl} \psi_{dr}$  in the rotor circuit is modified instantly because  $\omega_{sl} \psi_{dr} = L_m R_r i_{qs} / L_r$  as dictated by Equation (8.62). Since  $\psi_{qr} = 0$ , this EMF establishes the current  $(L_m / L_r) i_{qs}$  through the resistance  $R_r$ . To verify that this current satisfies  $\psi_{qr} = 0$ , we can write

$$\begin{aligned}
 \psi_{qr} &= \psi_m + \psi_{lr} \\
 &= L_m \left( \frac{L_m}{L_r} i_{qs} - i_{qs} \right) + \left( \frac{L_m}{L_r} i_{qs} \right) L_{lr} \\
 &= i_{qs} \left( \frac{L_m^2}{L_r} - L_m + \frac{L_m L_{lr}}{L_r} \right) = 0
 \end{aligned} \tag{8.72}$$

If  $L_{lr}$  is neglected for simplicity and flux  $\hat{\psi}_r$  is considered as constant, it can easily be seen that magnetizing current component  $i_{ds}$  flows through  $L_m$  only, whereas the torque component of current  $i_{qs}$  is constrained to flow to the rotor side only. This was the original hypothesis in explaining vector control with the help of Figs. 8.24 and 8.25.

#### 8.4.6.1 Indirect Vector Control Slip Gain ( $K_s$ ) Tuning

The slip gain  $K_s$  in indirect vector control (Figure 8.32) is a function of the machine's parameters. It is desirable that these parameters match the actual parameters of the machine at all operating conditions to achieve decoupling control of the machine. The slip gain detuning

problem is a serious disadvantage of indirect vector control. Of course, the problem is similar to direct vector control at low speeds, where the current model flux estimation is used.

With the close loop flux control shown in Figure 8.32, the estimated value of  $\hat{\psi}_r$  (input to  $K_s$ ) is known; therefore, the variation of three parameters, ( $L_m$ ,  $L_r$ , and  $R_r$ ), is of concern. The saturation effect of magnetizing inductance  $L_m$  almost cancels the variation of  $L_m/L_r$ , thus leaving the dominant effect of rotor resistance variation on  $K_s$ . With open loop flux control at steady-state condition,  $\hat{\psi}_r = i_{ds} L_m$ . Therefore,  $K_s$  becomes a function of rotor time constant  $T_r = L_r/R_r$  only.

The effect of rotor resistance detuning and the corresponding coupling effect are explained in Figure 8.37, where  $R_r$  = actual resistance of the machine and  $\hat{R}_r$  = estimated resistance used in the  $K_s$  parameter. If  $\hat{R}_r$  is lower than  $R_r$ , the slip frequency  $\omega_{sl}^*$  will be lower than the actual (see Figs. 8.32 and 8.36), giving backward alignment of the  $i_{ds}' - i_{qs}'$  current pair, as shown in Figure 8.37(a). With such misalignment, if torque is increased by a step of  $i_{qs}'$ , a component of this current on the  $d^e$  axis will increase the flux (overfluxing). The resulting torque and flux responses in both the transient and steady-state conditions are shown in Figure 8.37(b). On the other hand, the effect of higher than actual resistance ( $\hat{R}_r/R_r = 1.3$ ) will cause underfluxing, and the corresponding performance is indicated in Figure 8.37(b).

The initial tuning of slip gain is straightforward if the parameters of the machine are known a-priori. Conversely, an automated measurement of parameters can be made initially by injecting signals in the machine through the inverter and then estimating the parameters with the help of a DSP. This will be discussed later in self-commissioning of the drive. The initial tuning of  $K_s$  can also be done by giving a square-wave torque (or  $i_{qs}^*$ ) command and then matching the actual torque wave with the predicted torque wave under a tuned condition.

The continuous on-line tuning of  $K_s$  is very complex and demands rigorous computation by a DSP. A number of methods for slip gain tuning have been suggested in the literature. Unfortunately, most of these algorithms are also dependent on machine parameters. Fortunately, however, the temperature variation of  $R_r$  is somewhat slow, and this permits adequate computation time required by the DSP. The extended Kalman filter (EKF) method of parameter (or state) estimation based on the full-order dynamic machine model is an elegant and powerful method, and it will be discussed later for speed estimation.

Another method that is more acceptable is based on the model referencing adaptive control (MRAC) and is shown in general block diagram form in Figure 8.38 [16]. The MRAC principle will be discussed later in this chapter. Here, the reference model output signal  $X^*$  that satisfies the tuned vector control is usually a function of command currents  $i_{ds}^*$  and  $i_{qs}^*$ , machine inductances, and operating frequency. The adaptive model  $X$  is usually estimated by the machine feedback voltages and currents, as shown. The reference model output is compared with that of the adaptive model and the resulting error generates the estimated slip gain  $\hat{K}_s$ .



(b)

(b)

(8.73)

ng t

(8.74)

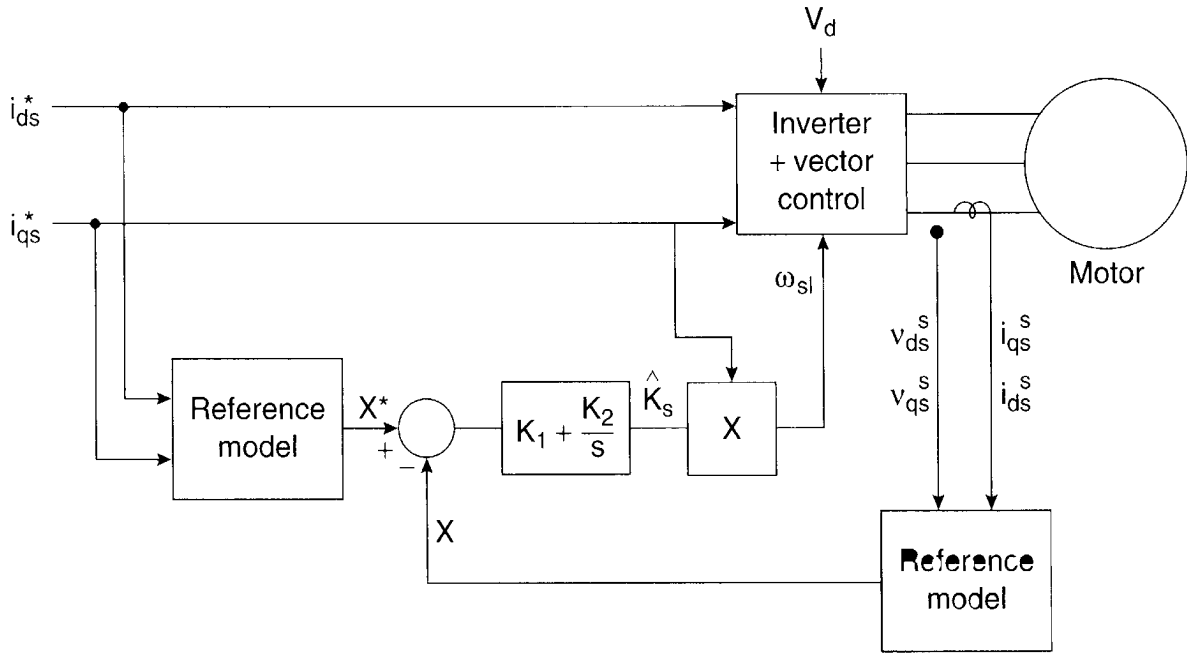


**Figure 8.38** Slip gain tuning by model referencing adaptive control principle

The actual torque  $T_e(X)$  can be estimated from stationary frame variables as follows:

$$X = T_e = \frac{3}{2} \left( \frac{P}{2} \right) (\psi_{ds}^s i_{qs}^s - \psi_{qs}^s i_{ds}^s) \quad (2.121)$$

Note that the  $L_m$  and  $L_r$  parameter variations affect the estimation accuracy of  $X^*$ . Additionally, at low speeds, the estimation accuracy of  $X$  will be affected by the variation of stator resistance  $R_s$ . Other MRAC-based slip gain tuning methods with fuzzy logic will be discussed in Chapter 11.

#### 8.4.7 Vector Control of Line-Side PWM Rectifier

The line-side converter in a double-sided PWM converter system (see Figure 5.60) can be vector-controlled to regulate the active  $I_P$  and reactive  $I_Q$  currents independently. In this case, the unit vector can be generated from the line voltage vector to orient  $I_P$  in phase and  $I_Q$  in quadrature, respectively. Figure 8.39 shows the control block diagram for the unity line power factor operation, and Figure 8.40 explains the operation's principle. The line voltage vector  $\bar{V}_s$  (of magnitude  $\hat{V}_s$ ) is oriented on the  $d^e$  axis so that

$$v_{ds}^s = \hat{V}_s \cos \theta_e \quad (8.75)$$

$$v_{qs}^s = \hat{V}_s \sin \theta_e \quad (8.76)$$

$$\cos \theta_e = \frac{v_{ds}^s}{\hat{V}_s} \quad (8.77)$$

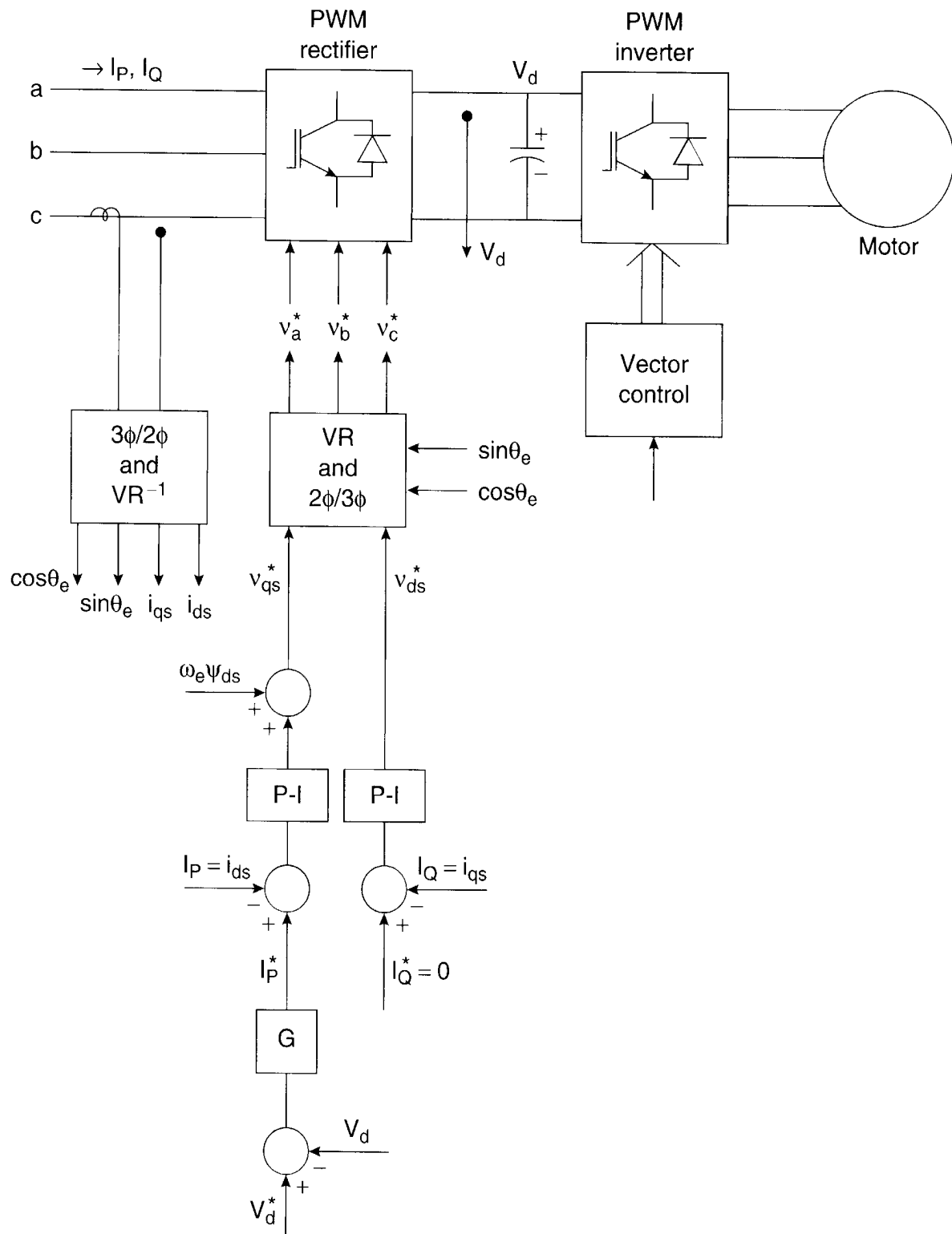


**Figure 8.39** Direct vector control of line-side PWM rectifier

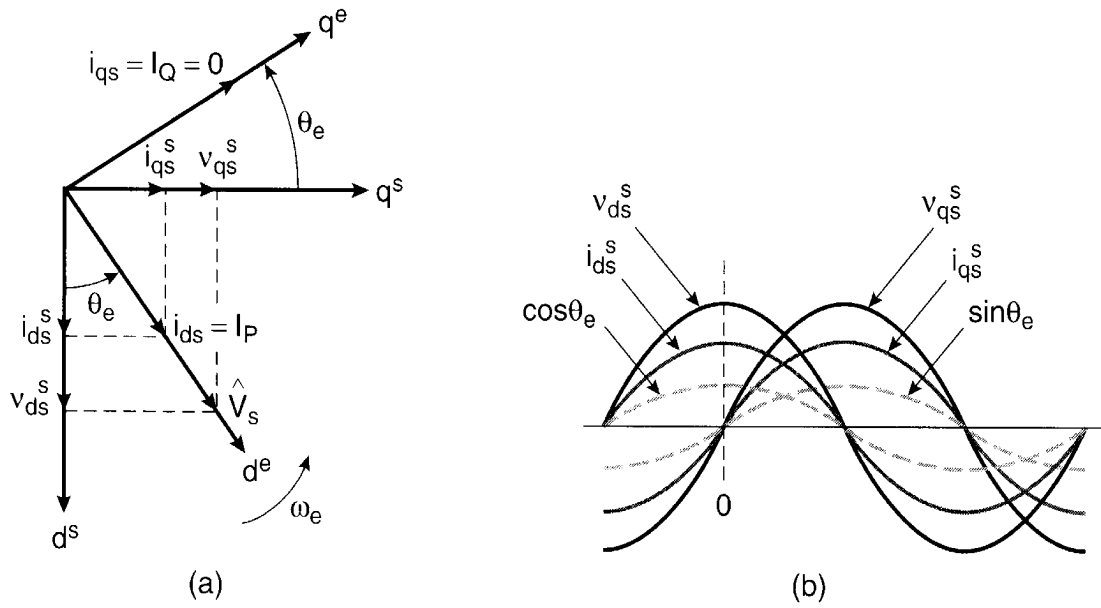


**Figure 8.40** Phasor diagram and waveforms for vector control

$$\sin \theta_e = \frac{v_{qs}^s}{\hat{V}_s} \quad (8.78)$$

where

$$\hat{V}_s = \sqrt{v_{ds}^{s^2} + v_{qs}^{s^2}} \quad (2.88)$$

Since  $i_{ds} = I_P$  and  $i_{qs} = I_Q = 0$ ,

$$i_{ds}^s = I_P \cos \theta_e \quad (8.79)$$

$$i_{qs}^s = I_P \sin \theta_e \quad (8.80)$$

Figure 8.40(b) shows the time-domain plot of the voltage and current waves, indicating the unity line power factor condition. In the control block diagram, the phase voltages are sensed, filtered, and converted to  $v_{ds}^s$  and  $v_{qs}^s$  variables. The unit vector signals  $\cos \theta_e$  and  $\sin \theta_e$  are then calculated by Equations (8.77)–(8.78). These are also used to generate  $i_{ds}$  and  $i_{qs}$  currents as shown in Figure 8.29. The line-side converter controls the dc link voltage  $V_d$  by a feedback loop. The loop error generates the active current command  $I_P^*$  with  $I_Q^* = 0$ . A synchronous current control loop (with CEMF injection in the  $I_P$  loop) and vector rotator then generate the phase voltage commands as shown. Note that if  $I_Q^*$  is positive, the line current will be at a leading power factor.



### 8.4.8 Stator Flux-Oriented Vector Control

So far, we have discussed rotor flux-oriented vector control only. It was mentioned before that vector control is also possible with air gap flux or stator flux orientation, but at the cost of a coupling effect that demands decoupling compensation. Stator flux-oriented direct vector control has the advantage that flux vector estimation accuracy is affected by the stator resistance ( $R_s$ ) variation only. In this section, we will develop a strategy for stator flux-oriented direct vector control by manipulating equations derived from  $d^e$ - $q^e$  equivalent circuits.

Multiplying Equations (8.57) and (8.58) by  $T_r = L_r/R_r$  we get

$$(1 + ST_r)\psi_{dr} - L_m i_{ds} - T_r \omega_{sl} \psi_{qr} = 0 \quad (8.81)$$

$$(1 + ST_r)\psi_{qr} - L_m i_{qs} + T_r \omega_{sl} \psi_{dr} = 0 \quad (8.82)$$

In these equations,  $\psi_{dr}$  and  $\psi_{qr}$  are to be eliminated and replaced by  $\psi_{qs}$  and  $\psi_{ds}$ . The stator flux expressions can be written from  $d^e$ - $q^e$  equivalent circuits as

$$\psi_{ds} = L_s i_{ds} + L_m i_{dr} \quad (8.83)$$

$$\psi_{qs} = L_s i_{qs} + L_m i_{qr} \quad (8.84)$$

or

$$i_{dr} = \frac{\psi_{ds}}{L_m} - \frac{L_s}{L_m} i_{ds} \quad (8.85)$$

$$i_{qr} = \frac{\psi_{qs}}{L_m} - \frac{L_s}{L_m} i_{qs} \quad (8.86)$$

Substituting Equations (8.85) and (8.86) in Equations (8.53) and (8.54), respectively, we get

$$\psi_{dr} = \frac{L_r}{L_m} \psi_{ds} + (L_m - \frac{L_r L_s}{L_m}) i_{ds} \quad (8.87)$$

$$\psi_{qr} = \frac{L_r}{L_m} \psi_{qs} + (L_m - \frac{L_r L_s}{L_m}) i_{qs} \quad (8.88)$$

These equations relate stator and rotor fluxes with stator currents. Substituting Equations (8.87) and (8.88) in Equations (8.81) and (8.82), respectively, then multiplying both sides by  $L_m/L_r$  and simplifying, we get

$$(1 + ST_r)\psi_{ds} = (1 + \sigma ST_r)L_s i_{ds} + \omega_{sl} T_r [\psi_{qs} - \sigma L_s i_{qs}] \quad (8.89)$$

$$(1 + ST_r)\psi_{qs} = (1 + \sigma ST_r)L_s i_{qs} - \omega_{sl} T_r [\psi_{ds} - \sigma L_s i_{ds}] \quad (8.90)$$

where  $\sigma = 1 - L_m^2 / L_s L_r$ .

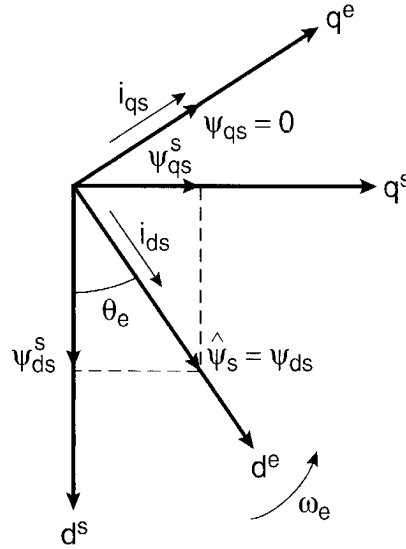


**Figure 8.41** Phasor diagram with stator flux-oriented vector control

With stator flux-oriented vector control, as shown in the phasor diagram of Figure 8.41,  $\psi_{qs} = 0$ ,  $\psi_{ds} = \hat{\psi}_s$ . Therefore, Equations (8.89) and (8.90) can be written, respectively, as

$$(1 + ST_r)\psi_{ds} = (1 + \sigma ST_r)L_s i_{ds} - \sigma L_s T_r \omega_{sl} i_{qs} \quad (8.91)$$

$$(1 + \sigma ST_r)L_s i_{qs} = \omega_{sl} T_r [\psi_{ds} - \sigma L_s i_{ds}] \quad (8.92)$$

These equations indicate that stator flux  $\psi_{ds}$  is a function of both the  $i_{ds}$  and  $i_{qs}$  currents; in other words, there is coupling effect. This means that if the torque is changed by  $i_{qs}$ , it will also change the flux. Therefore, this coupling effect must be eliminated by the feedforward control method.

Consider the decoupler block diagram in Figure 8.42, where the decoupling signal  $i_{dq}$  as shown is being added in the flux control loop to generate the  $i_{ds}^*$  command signal. From Figure 8.42, we can write

$$i_{ds}^* = G(\psi_{ds}^* - \psi_{ds}) + i_{dq} \quad (8.93)$$

where  $G = K_1 + K_2/S$ . Substituting Equation (8.93) in (8.91), we get

$$(1 + ST_r)\psi_{ds} = L_s \left[ (1 + \sigma ST_r)G(\psi_{ds}^* - \psi_{ds}) + (1 + \sigma ST_r)i_{dq} - \sigma T_r \omega_{sl} i_{qs} \right] \quad (8.94)$$

For decoupling control of  $\psi_{ds}$  with the help of  $i_{dq}$ , terms  $(1 + \sigma ST_r)i_{dq} - \sigma T_r \omega_{sl} i_{qs} = 0$ , that is,

$$i_{dq} = \frac{\sigma T_r \omega_{sl} i_{qs}}{(1 + \sigma ST_r)} \quad (8.95)$$

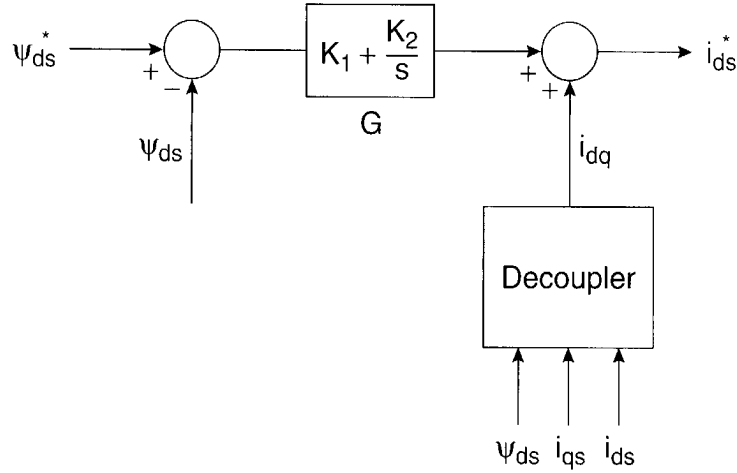


**Figure 8.42** Feedforward decoupling signal injection in stator flux-oriented vector control

where  $\omega_{sl}$  can be written from Equation (8.92) as

$$\omega_{sl} = \frac{(1 + \sigma ST_r) L_s i_{qs}}{T_r (\psi_{ds} - \sigma L_s i_{ds})} \quad (8.96)$$

Combining Equations (8.95) and (8.96), we get

$$i_{dq} = \frac{\sigma L_s i_{qs}^2}{(\psi_{ds} - \sigma L_s i_{ds})} \quad (8.97)$$

which indicates that decoupling current  $i_{dq}$  is a function of  $\psi_{ds}$ ,  $i_{qs}$ , and  $i_{ds}$ . This functionality is indicated in the block diagram of Figure 8.42. The general expression of developed torque is

$$T_e = \frac{3}{2} \left( \frac{P}{2} \right) (\psi_{ds} i_{qs} - \psi_{qs} i_{ds}) \quad (2.114)$$

With vector control,  $\psi_{qs} = 0$ , or

$$T_e = \frac{3}{2} \left( \frac{P}{2} \right) \psi_{ds} i_{qs} \quad (8.98)$$

Figure 8.43 shows a block diagram with a stator flux-oriented vector control, where the feedback estimation block computes Equations (8.32), (8.33), (8.34), (8.65), (8.66), (8.70), (8.99), and (8.100). Since the stator resistance  $R_s$  is a function of the stator winding temperature only, it can easily be compensated. Note that  $i_{dq}$  accuracy can be affected by parameter variation.



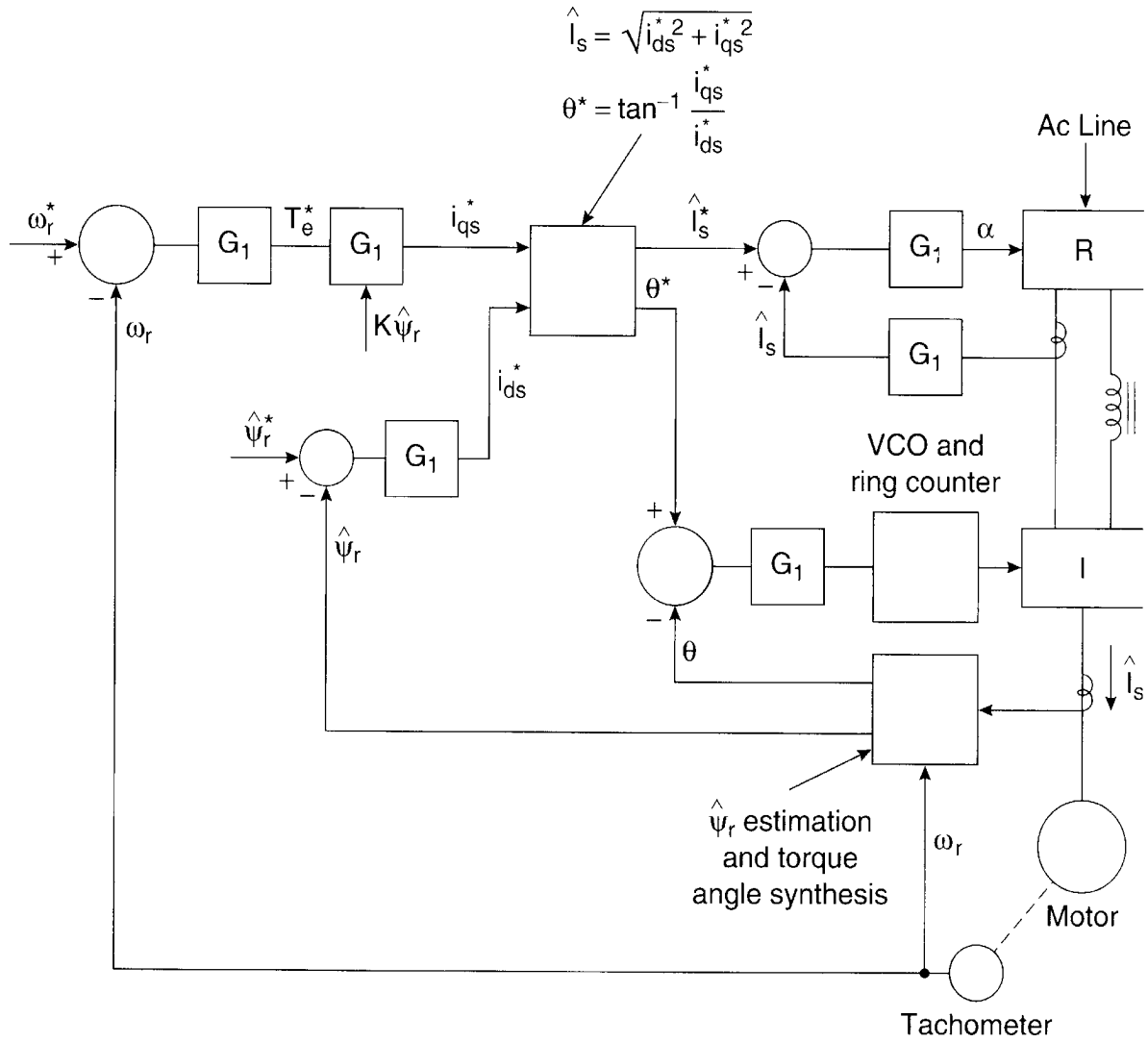


Figure 8.44 Vector-controlled, current-fed inverter drive

$$i_{qs} = i_{qs}^s \cos \theta_e - i_{ds}^s \sin \theta_e \quad (8.99)$$

$$i_{ds} = i_{qs}^s \sin \theta_e + i_{ds}^s \cos \theta_e \quad (8.100)$$

$$\angle \theta = \tan^{-1} \frac{i_{qs}}{i_{ds}} \quad (8.101)$$

The control scheme remains valid from zero speed and in all quadrants.

#### 8.4.10 Vector Control of Cycloconverter Drive

The direct and indirect methods of vector control which have been discussed so far can easily be applied to cycloconverter-controlled induction motor drives, where the inverter is replaced by a cycloconverter, and all other signal processing remains the same. With direct vec-

tor control using an instantaneous current-controlled cycloconverter, either the voltage model (Figure 8.27) or current model (Figure 8.30) flux vector ( $\psi_{dr}^s, \psi_{qr}^s$ ) estimation can be used. The indirect vector control shown in Figure 8.32 can also be used. In either type of vector control, the instantaneous phase current control can be replaced by the voltage control within synchronous current control loops (Figure 8.34). The signals can also be processed in polar form instead of cartesian form. Vector control of a cycloconverter-fed synchronous motor drive will be discussed in Chapter 9.

In this section, we will review vector control of a Scherbius drive, which was discussed in Chapter 7. The cycloconverter is placed in the rotor circuit of a wound-rotor induction motor as shown in Figure 8.45. In this figure, the cycloconverter is required to send slip energy ( $+SP_g$ ) to the line in subsynchronous motoring and supersynchronous regeneration, and to feed slip energy to the rotor ( $-SP_g$ ) in subsynchronous regeneration and supersynchronous motoring. Currents  $I_P$  and  $I_Q$  are the in-phase and quadrature components of the rotor current, respectively, with respect to slip voltage  $V_r$ . The positive direction of  $I_P$  is shown in the figure. The error from the speed control loop generates the current command  $I_P^*$ . The current  $I_Q^*$  can be set to zero or to an arbitrary value. The polarity of  $I_P^*$  depends on the error polarity. The signal goes through a polarity reverser, as shown, where the signal polarity is reversed if the speed is in supersynchronous range, but otherwise remains the same. The unit vector signals  $\cos \theta_{sl}$  and  $\sin \theta_{sl}$  are obtained from the following relations:

$$\cos \theta_{sl} = \cos(\theta_e - \theta_r) = \cos \theta_e \cos \theta_r + \sin \theta_e \sin \theta_r \quad (8.102)$$

$$\sin \theta_{sl} = \sin(\theta_e - \theta_r) = \sin \theta_e \cos \theta_r - \cos \theta_e \sin \theta_r \quad (8.103)$$

where  $\theta_e$  = line unit vector obtained from Equations (8.77)–(8.78) (see Figure 8.40(a)), and  $\theta_r$  = rotor position signal obtained from the speed encoder. The cycloconverter phase current commands at slip frequency are then obtained by standard vector rotation of  $I_P^*$  and  $I_Q^*$  and  $2\phi/3\phi$  transformation, as usual. If the machine speed changes from a subsynchronous to supersynchronous ( $\omega_r > \omega_e$ ) range, the slip voltage phase sequence will change from positive to negative. The corresponding reversal of the phase sequence of the  $\cos \theta_{sl}$  and  $\sin \theta_{sl}$  signals will also reverse the phase sequence of the rotor currents. At true synchronous speed, the machine operates as a synchronous motor or generator, and in this condition, the cycloconverter operates as a rectifier, supplying dc excitation current to the machine rotor winding. At this condition, signals  $\cos \theta_{sl}$  and  $\sin \theta_{sl}$  freeze to dc values, and correspondingly, dc phase current commands are generated for the cycloconverter.

To understand drive operation clearly, consider, for example, a drive that is accelerating from subsynchronous speed with the command speed at a supersynchronous value. At subsynchronous motoring,  $I_P^*$  is positive because  $I_P^{*'} is positive and the polarity reverser is in a non-reversing mode. With  $+\omega_{sl}$ , the phase sequence of rotor currents is positive and  $I_P$  is in phase with  $V_r$  so that slip power  $SP_g$  is positive. At synchronous speed,  $\theta_{sl} = 0$ , that is,  $I_P$  is dc current. At supersynchronous speed motoring,  $I_P^*$  becomes negative due to the negative polarity of the$



## 8.5 SENSORLESS VECTOR CONTROL

Sensorless vector control of an induction motor drive essentially means vector control without any speed sensor. An incremental shaft-mounted speed encoder (usually an optical type) is required for close loop speed or position control in both vector- and scalar-controlled drives. A speed signal is also required in indirect vector control in the whole speed range, and in direct vector control for the low-speed range, including the zero speed start-up operation. A speed encoder is undesirable in a drive because it adds cost and reliability problems, besides the need for a shaft extension and mounting arrangement. It is possible to estimate the speed signal from machine terminal voltages and currents with the help of a DSP. However, the estimation is normally complex and heavily dependent on machine parameters. Although sensorless vector-controlled drives are commercially available at this time, the parameter variation problem, particularly near zero speed, imposes a challenge in the accuracy of speed estimation.

### 8.5.1 Speed Estimation Methods

The induction motor speed estimation techniques proposed in the literature can generally be classified as follows:

- Slip calculation
- Direct synthesis from state equations
- Model referencing adaptive system (MRAS)
- Speed adaptive flux observer (Luenberger observer)
- Extended Kalman filter (EKF)
- Slot harmonics
- Injection of auxiliary signal on salient rotor

Detailed descriptions and historical reviews of all these methods [18] are beyond the scope of this book. However, the methods will be reviewed briefly and a few selected methods will be described in some detail.

#### 8.5.1.1 Slip Calculation

Speed can be calculated from slip frequency  $\omega_{sl}$  from the relation  $\omega_r = \omega_e - \omega_{sl}$ , where  $\omega_e$  = stator frequency (r/s). The  $\omega_{sl}$  signal was calculated before in stator flux-oriented direct vector control (Figure 8.43) as

$$\omega_{sl} = \frac{(1 + \sigma S T_r) L_s i_{qs}}{T_r (\psi_{ds} - \sigma L_s i_{ds})} \quad (8.96)$$

where  $\sigma = 1 - L_m^2 / L_s L_r$ ,  $T_r = L_r / R_r$ , and  $i_{ds}$ ,  $i_{qs}$ , and  $\psi_{ds}$  are the signals corresponding to stator flux orientation. Equation (8.96) can also be expressed with variables for rotor flux-oriented vector control. The expression for stator frequency is given as



$$\omega_e = \frac{(v_{qs}^s - i_{qs}^s R_s) \psi_{ds}^s - (v_{ds}^s - i_{ds}^s R_s) \psi_{qs}^s}{\hat{\psi}_s^2} \quad (8.70)$$

The speed  $\omega_r$  can be calculated from Equations (8.96) and (8.70). For scalar and indirect vector control, the  $\omega_e$  signal can be available directly as a control variable. The signal can also be calculated by processing the waveform. An accurate calculation of slip frequency for a high-efficiency machine, particularly near synchronous speed, is difficult because the signal magnitude is small and highly dependent on machine parameters. Besides, there is the problem of direct integration of machine terminal voltages (see Figure 8.29) at low speeds to synthesize the  $\omega_{sl}$  and  $\omega_e$  signals.

#### 8.5.1.2 Direct Synthesis from State Equations

The dynamic  $d^s$ - $q^s$  frame state equations of a machine can be manipulated to compute the speed signal directly. The method described here is essentially similar to the slip calculation method discussed previously. The stator voltage equation for  $v_{ds}^s$  in a  $d^s$ - $q^s$  equivalent circuit can be written as

$$v_{ds}^s = i_{ds}^s R_s + L_{ls} \frac{d}{dt}(i_{ds}^s) + \frac{d}{dt}(\psi_{dm}^s) \quad (8.104)$$

Substituting Equation (8.39) in (8.104) gives

$$v_{ds}^s = \frac{L_m}{L_r} \frac{d}{dt}(\psi_{dr}^s) + (R_s + \sigma L_s S) i_{ds}^s \quad (8.105)$$

where  $\sigma = 1 - L_m^2/L_r L_s$

or

$$\frac{d}{dt}(\psi_{dr}^s) = \frac{L_r}{L_m} v_{ds}^s - \frac{L_r}{L_m} (R_s + \sigma L_s S) i_{ds}^s \quad (8.106)$$

Similarly, the  $\psi_{qr}^s$  expression can be derived as

$$\frac{d}{dt}(\psi_{qr}^s) = \frac{L_r}{L_m} v_{qs}^s - \frac{L_r}{L_m} (R_s + \sigma L_s S) i_{qs}^s \quad (8.107)$$

The rotor flux equations in a  $d^s$ - $q^s$  frame can be given as

$$\frac{d}{dt}(\psi_{dr}^s) = \frac{L_m}{T_r} i_{ds}^s - \omega_r \psi_{qr}^s - \frac{1}{T_r} \psi_{dr}^s \quad (8.48)$$

$$\frac{d}{dt}(\psi_{qr}^s) = \frac{L_m}{T_r} i_{qs}^s + \omega_r \psi_{dr}^s - \frac{1}{T_r} \psi_{qr}^s \quad (8.49)$$

From Figure 8.31, we can write

$$\angle \theta_e = \tan^{-1} \frac{\psi_{qr}^s}{\psi_{dr}^s} \quad (8.108)$$

Differentiating Equation (8.108), we get

$$\frac{d\theta_e}{dt} = \frac{\psi_{dr}^s \dot{\psi}_{qr}^s - \psi_{qr}^s \dot{\psi}_{dr}^s}{\hat{\psi}_r^2} \quad (8.109)$$

Combining Equations (8.46), (8.47), and (8.109) [19] and simplifying, we get

$$\omega_r = \frac{d\theta_e}{dt} - \frac{L_m}{T_r} \left[ \frac{\psi_{dr}^s i_{qs}^s - \psi_{qr}^s i_{ds}^s}{\hat{\psi}_r^2} \right] \quad (8.110)$$

or

$$\omega_r = \frac{1}{\hat{\psi}_r^2} \left[ (\psi_{dr}^s \dot{\psi}_{qr}^s - \psi_{qr}^s \dot{\psi}_{dr}^s) - \frac{L_m}{T_r} (\psi_{dr}^s i_{qs}^s - \psi_{qr}^s i_{ds}^s) \right] \quad (8.111)$$

Figure 8.46 gives a block diagram for speed estimation where the voltage model equations, (8.106) and (8.107), have been used to estimate the rotor fluxes. Evidently, the synthesis is highly machine parameter-sensitive and will tend to give poor accuracy of estimation.

### 8.5.1.3 Model Referencing Adaptive System (MRAS)

The speed can be calculated by the model referencing adaptive system (MRAS), where the output of a reference model is compared with the output of an adjustable or adaptive model until the errors between the two models vanish to zero. A block diagram for speed estimation by the MRAS technique is shown in Figure 8.47. Consider the voltage model's stator-side equations, (8.106) and (8.107), which are defined as a reference model in Figure 8.47. The model receives the machine stator voltage and current signals and calculates the rotor flux vector signals, as indicated. The current model flux equations, (8.46) and (8.47), are defined as an adaptive model in Figure 8.47. This model can calculate fluxes from the input stator currents only if the speed signal  $\omega_r$  (shown in the coefficient matrix) is known. With the correct speed signal, ideally, the fluxes calculated from the reference model and those calculated from the adaptive model will match, that is,  $\psi_{dr}^s = \hat{\psi}_{dr}^s$  and  $\psi_{qr}^s = \hat{\psi}_{qr}^s$ , where  $\hat{\psi}_{dr}^s$  and  $\hat{\psi}_{qr}^s$  are the adaptive model out-

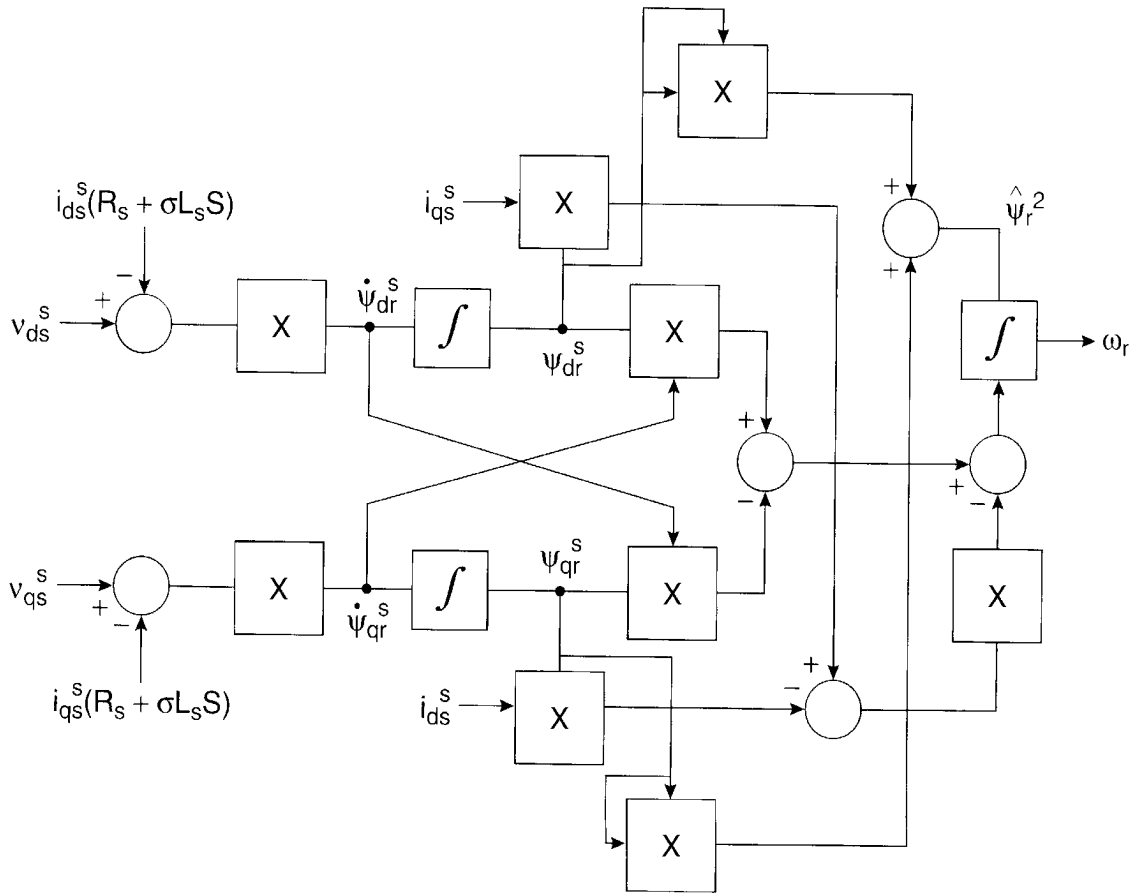


**Figure 8.46** Speed estimation by direct synthesis from state equations

puts. An adaptation algorithm with P-I control, as indicated, can be used to tune the speed  $\hat{\omega}_r$  so that the error  $\xi = 0$ .

In designing the adaptation algorithm for the MRAS, it is important to take account of the overall stability of the system and to ensure that the estimated speed will converge to the desired value with satisfactory dynamic characteristics. Using Popov's criteria for hyperstability [29] for a globally asymptotically stable system, we can derive the following relation for speed estimation:

$$\hat{\omega}_r = \xi \left( K_P + \frac{K_I}{S} \right) \quad (8.112)$$

where

$$\xi = X - Y = \hat{\psi}_{dr}^s \psi_{qr}^s - \psi_{dr}^s \hat{\psi}_{qr}^s \quad (8.113)$$

In steady state,  $\xi = 0$ , balancing the fluxes; in other words,  $\psi_{dr}^s = \hat{\psi}_{dr}^s$  and  $\psi_{qr}^s = \hat{\psi}_{qr}^s$ . The MRAS in Figure 8.47 can be interpreted as a vector PLL in which the output flux vector from the reference model is the reference vector and the adjustable model is a vector phase shifter controlled by  $\hat{\omega}_r$ .

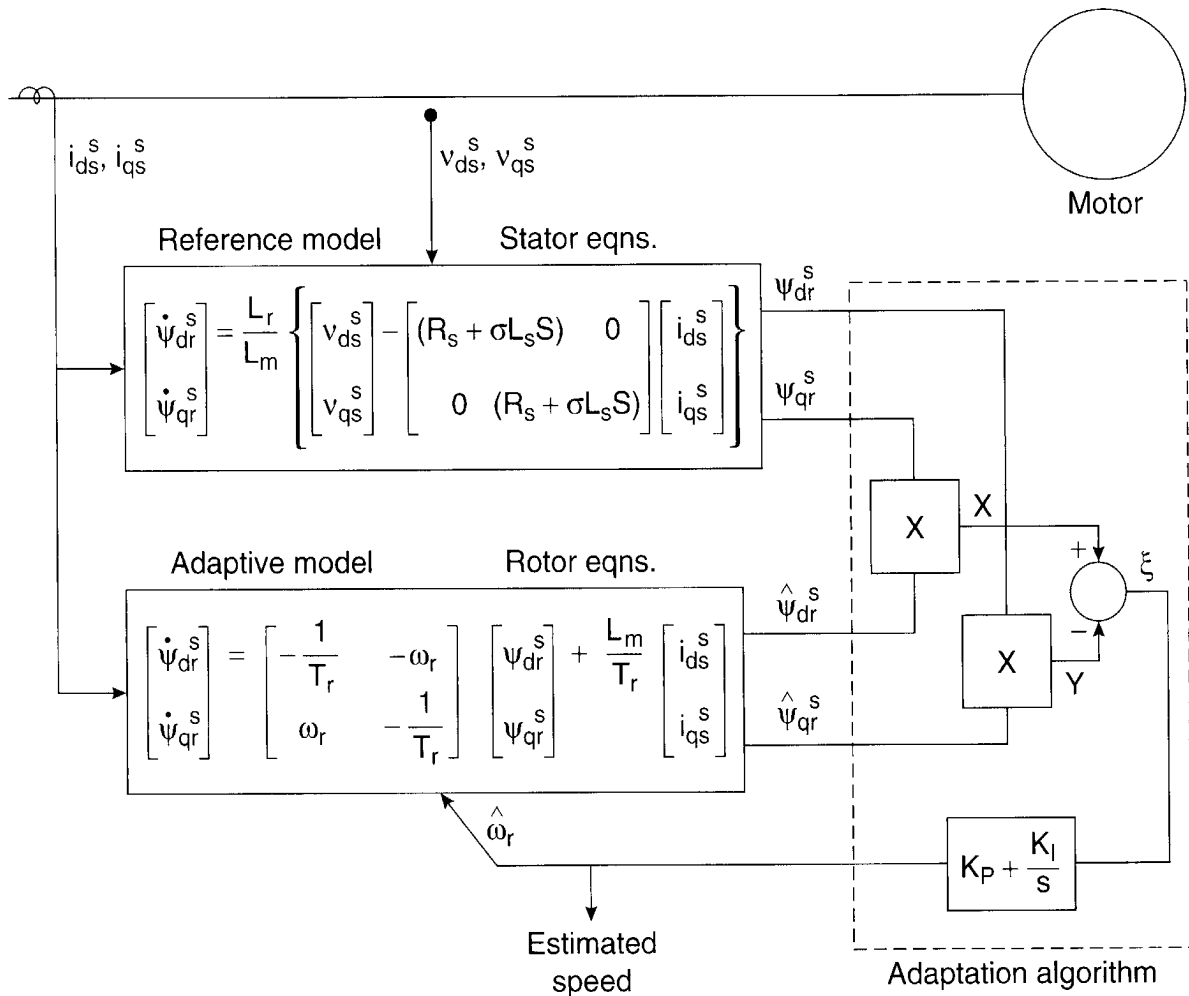


**Figure 8.47** Speed estimation by model referencing adaptive control (MRAC) principle

In practice, the rotor flux synthesis based on the reference model is difficult to implement, particularly at low speeds, because of the pure integration of the voltage signals. The MRAS speed estimation algorithm remains valid if, instead of integration, the corresponding CEMF signals are compared directly through some low-pass filters. Estimation accuracy can be good if machine parameters are considered as constant. However, accuracy, particularly at low speeds, deteriorates due to parameter variation.

#### 8.5.1.4 Speed Adaptive Flux Observer (Luenberger Observer)

An improved method of speed estimation that operates on the principle of a speed adaptive flux observer has been proposed in [20]. An observer is basically an estimator that uses a plant model (full or partial) and a feedback loop with measured plant variables. Here, the full-order observer uses the machine electrical model in  $d^s$ - $q^s$  frame, where the state variables are stator currents  $i_{ds}^s$  and  $i_{qs}^s$  and the rotor fluxes are  $\psi_{dr}^s$  and  $\psi_{qr}^s$ . Let us first derive this model from the  $d^s$ - $q^s$  equivalent circuits shown in Figure 2. 27.

The rotor voltage equations can be written as

$$i_{dr}^s R_r + \frac{d}{dt}(\psi_{dr}^s) + \omega_r \psi_{qr}^s = 0 \quad (8.114)$$

$$i_{qr}^s R_r + \frac{d}{dt}(\psi_{qr}^s) - \omega_r \psi_{dr}^s = 0 \quad (8.115)$$

Eliminating  $i_{dr}^s$  from Equation (8.114) with the help of Equation (8.37) yields

$$\frac{d}{dt}(\psi_{dr}^s) = -\frac{R_r}{L_r} \psi_{dr}^s - \omega_r \psi_{qr}^s + \frac{L_m R_r}{L_r} i_{ds}^s \quad (8.116)$$

Similarly, from the  $q^s$  circuit,

$$\frac{d}{dt}(\psi_{qr}^s) = -\frac{R_r}{L_r} \psi_{qr}^s + \omega_r \psi_{dr}^s + \frac{L_m R_r}{L_r} i_{qs}^s \quad (8.117)$$

Substituting Equations (8.116) and (8.117) in (8.106) and (8.107), respectively, and simplifying, we get

$$\frac{d}{dt}(i_{ds}^s) = -\frac{(L_m^2 R_r + L_r^2 R_s)}{\sigma L_s L_r^2} i_{ds}^s + \frac{L_m R_r}{\sigma L_s L_r^2} \psi_{dr}^s + \frac{L_m \omega_r}{\sigma L_s L_r} \psi_{qr}^s + \frac{1}{\sigma L_s} v_{ds}^s \quad (8.118)$$

$$\frac{d}{dt}(i_{qs}^s) = -\frac{(L_m^2 R_r + L_r^2 R_s)}{\sigma L_s L_r^2} i_{qs}^s - \frac{L_m \omega_r}{\sigma L_s L_r} \psi_{dr}^s + \frac{L_m R_r}{\sigma L_s L_r^2} \psi_{qr}^s + \frac{1}{\sigma L_s} v_{qs}^s \quad (8.119)$$

where  $\sigma = 1 - L_m^2/L_s L_r$ , and  $L_{ls}$  and  $L_{lr}$  have been substituted by  $L_s - L_m$  and  $L_r - L_m$ , respectively.

Equations (8.116)–(8.119) constitute the desired state equations, which can be written in the form

$$\frac{d}{dt}(X) = AX + BV_s \quad (8.120)$$

where

$$X = \begin{bmatrix} i_{ds}^s & i_{qs}^s & \psi_{dr}^s & \psi_{qr}^s \end{bmatrix}^T \quad (8.121)$$

$$V_s = \begin{bmatrix} v_{ds}^s & v_{qs}^s & 0 & 0 \end{bmatrix}^T \quad (8.122)$$

$$A = \begin{bmatrix} \frac{(L_m^2 R_r + L_r^2 R_s)}{\sigma L_s L_r^2} & 0 & \frac{L_m R_r}{\sigma L_s L_r^2} & \frac{L_m \omega_r}{\sigma L_s L_r} \\ 0 & -\frac{(L_m^2 R_r + L_r^2 R_s)}{\sigma L_s L_r^2} & -\frac{L_m \omega_r}{\sigma L_s L_r} & \frac{L_m R_r}{\sigma L_s L_r^2} \\ \frac{L_m R_r}{L_r} & 0 & -\frac{R_r}{L_r} & -\omega_r \\ 0 & \frac{L_m R_r}{L_r} & \omega_r & \frac{R_r}{L_r} \end{bmatrix} \quad (8.123)$$

$$B = \begin{bmatrix} \frac{1}{\sigma L_s} & 0 \\ 0 & \frac{1}{\sigma L_s} \\ 0 & 0 \\ 0 & 0 \end{bmatrix} \quad (8.124)$$

Note that parameter matrix  $A$  contains the speed signal  $\omega_r$ , which is to be estimated.

Figure 8.48 shows the block diagram of the speed adaptive flux observer using the above machine model, where the symbol “^” means the estimated value. The output current signals  $\hat{i}_{ds}^s$  and  $\hat{i}_{qs}^s$  are derived through the following  $C$  matrix:

$$C = \begin{bmatrix} 1 & 0 & 0 & 0 \\ 0 & 1 & 0 & 0 \end{bmatrix} \quad (8.125)$$

Input voltage signals  $v_{ds}^s$  and  $v_{qs}^s$  are measured from the machine terminal. If speed signal  $\omega_r$  in parameter matrix  $A$  is known, the fluxes and currents can be solved from the state equations. However, if the  $\omega_r$  signal is not correct, there will be a deviation between the estimated states and the actual states. In the figure, the estimated currents are compared with the actual machine terminal currents, and the errors inject the auxiliary corrective signals  $eG$  through gain matrix  $G$ , as shown, so that matrix  $e$  tends to vanish. The observer equation can be given as

$$\frac{d}{dt}(\hat{X}) = \hat{A}\hat{X} + BV_s + G(\hat{i}_s - i_s) \quad (8.126)$$

where  $\hat{i}_s = [i_{ds}^s \ i_{qs}^s]$  and  $G$  = observer gain matrix. The observer also gives an estimation of the flux vector, as shown in the figure.

The speed adaptive flux observer permits estimation of the unknown speed  $\omega_r$  (which is considered a parameter) in matrix  $A$ . To derive the speed adaptation algorithm, Lyapunov's

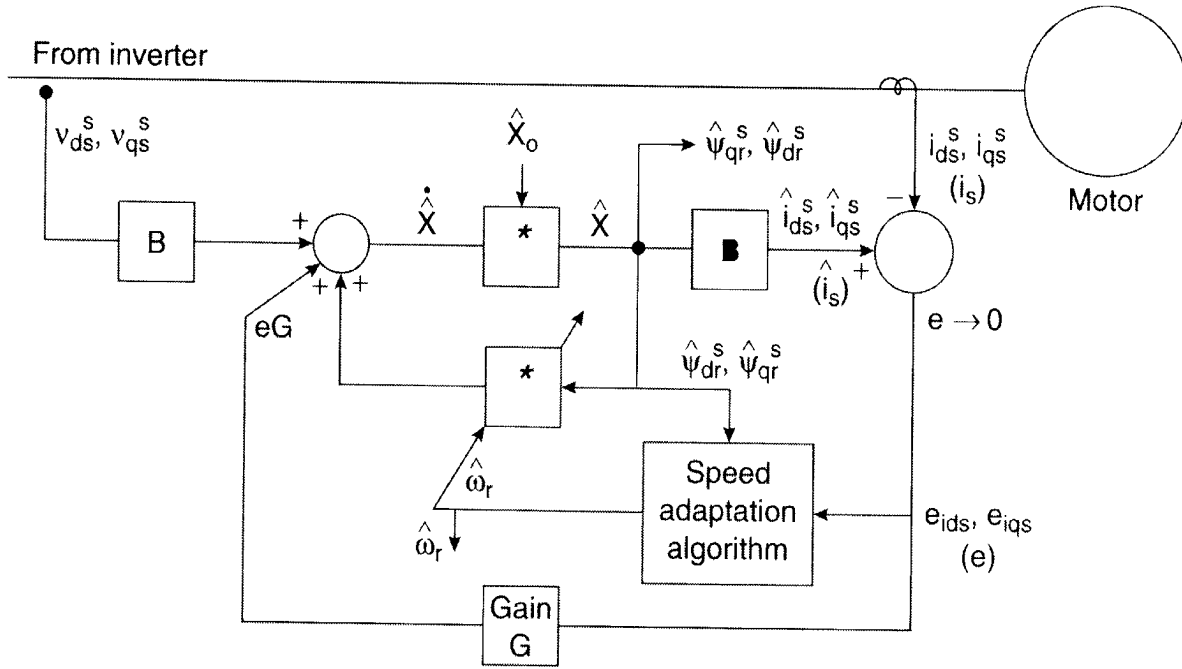


**Figure 8.48** Speed adaptive flux observer

theorem is utilized. In general, the estimation error of the stator currents and rotor fluxes is described by the following equation:

$$\frac{d}{dt}(e) = (A + GC)e - \Delta A \hat{X} \quad (8.127)$$

where

$$e = X - \hat{X} \quad (8.128)$$

$$\Delta A = \hat{A} - A = \begin{bmatrix} 0 & -\frac{\Delta \omega_r j}{c} \\ 0 & \Delta \omega_r j \end{bmatrix} \quad (8.129)$$

$$j = \begin{bmatrix} 0 & -1 \\ 1 & 0 \end{bmatrix} \quad (8.130)$$

$$\Delta \omega_r = \hat{\omega}_r - \omega_r \quad (8.131)$$

$$c = \frac{\sigma L_s L_r}{L_m} \quad (8.132)$$

Let us define the following Lyapunov function candidate:

$$V = e^T e + \frac{(\hat{\omega}_r - \omega_r)^2}{\lambda} \quad (8.133)$$

where  $\lambda$  is a positive constant.

The time derivative of  $V$  becomes

$$\frac{dV}{dt} = e^T \left[ (A + GC)^T + (A + GC) \right] e - 2\Delta\omega_r (e_{ids}\hat{\psi}_{qr}^s - e_{iqs}\hat{\psi}_{dr}^s) / c + \frac{2\Delta\omega_r}{\lambda} \frac{d\hat{\omega}_r}{dt} \quad (8.134)$$

where  $e_{ids}^s = i_{ds}^s - \hat{i}_{ds}^s$  and  $e_{iqs}^s = i_{qs}^s - \hat{i}_{qs}^s$ .

From the above equation, we can derive the following adaptation scheme for speed estimation by equalizing the second term with the third term, that is,

$$\frac{d\hat{\omega}_r}{dt} = \lambda (e_{ids}\hat{\psi}_{qr}^s - e_{iqs}\hat{\psi}_{dr}^s) / c \quad (8.135)$$

If the observer gain matrix  $G$  is chosen such that the first term of Equation (8.134) is negative-semidefinite, the speed adaptive flux observer is stable. Since the speed  $\omega_r$  can change quickly, the following proportional and integral adaptive scheme is used in the speed adaptation algorithm to improve the response of the speed estimation:

$$\hat{\omega}_r = K_P (e_{ids}\hat{\psi}_{qr}^s - e_{iqs}\hat{\psi}_{dr}^s) + K_I \int (e_{ids}\hat{\psi}_{qr}^s - e_{iqs}\hat{\psi}_{dr}^s) dt \quad (8.136)$$

where  $K_P$  and  $K_I$  are arbitrary positive gains.

Although the speed estimation accuracy is improved by the observer, there is a finite parameter variation (particularly in the stator and rotor resistances) effect. The estimation error tends to be more dominant as the speed approaches zero.

#### 8.5.1.5 Extended Kalman Filter (EKF)

The extended Kalman filter (EKF) is basically a full-order stochastic observer for the recursive optimum state estimation of a nonlinear dynamical system in real time by using signals that are corrupted by noise. The EKF can also be used for unknown parameter estimation (such as rotor resistance  $R_r$ ) or joint state and parameter estimation. The Luenberger observer, as discussed previously, is a deterministic observer (without noise) in comparison with the EKF, and is applicable to linear time-invariant systems. The noise sources in EKF take into account mea-



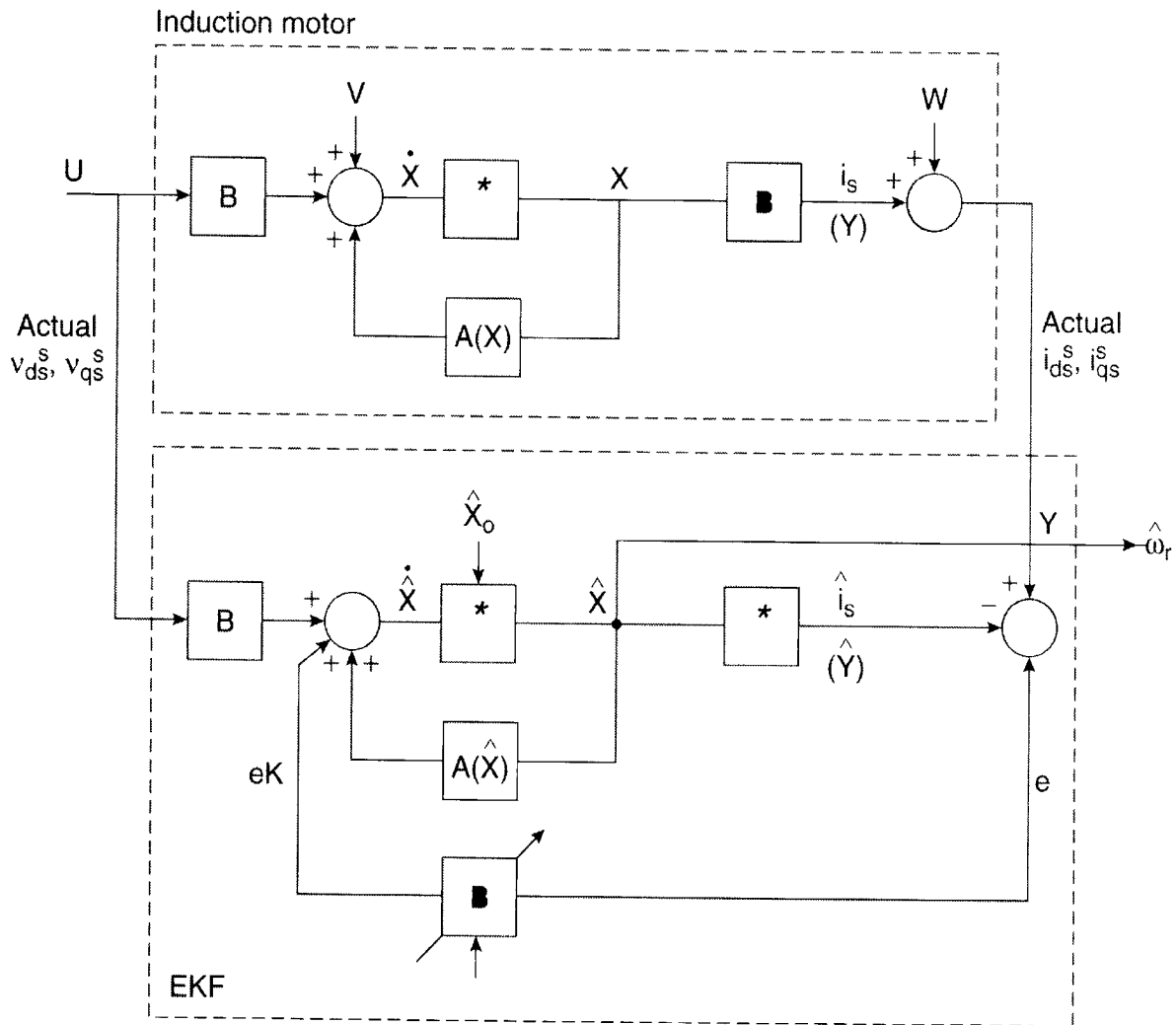


**Figure 8.49** Extended Kalman filter for estimation of speed

surement and modeling inaccuracies. The original Kalman filter is applicable only to a linear system. Figure 8.49 shows the block diagram of the EKF algorithm, where the machine model is indicated on the top. The EKF algorithm uses the full machine dynamic model, where the speed  $\omega_r$  is considered a parameter as well as a state. The augmented machine model can be given as [see Equations (8.120)–(8.124)]

$$\frac{dX}{dt} = AX + BV_s \quad (8.137)$$

$$Y = CX \quad (8.138)$$

where

$$A = \begin{bmatrix} \frac{(L_m^2 R_r + L_r^2 R_s)}{\sigma L_s L_r^2} & 0 & \frac{L_m R_r}{\sigma L_s L_r^2} & \frac{L_m \omega_r}{\sigma L_s L_r} & 0 \\ 0 & \frac{(L_m^2 R_r + L_r^2 R_s)}{\sigma L_s L_r^2} & \frac{L_m \omega_r}{\sigma L_s L_r} & \frac{L_m R_r}{\sigma L_s L_r^2} & 0 \\ \frac{L_m R_r}{L_r} & 0 & -\frac{R_r}{L_r} & -\omega_r & 0 \\ 0 & \frac{L_m R_r}{L_r} & \omega_r & -\frac{R_r}{L_r} & 0 \\ 0 & 0 & 0 & 0 & 0 \end{bmatrix} \quad (8.139)$$

$$X = \begin{bmatrix} i_{ds}^s & i_{qs}^s & \psi_{dr}^s & \psi_{qr}^s & \omega_r \end{bmatrix}^T \quad (8.140)$$

$$B = \begin{bmatrix} \frac{1}{\sigma L_s} & 0 \\ 0 & \frac{1}{\sigma L_s} \\ 0 & 0 \\ 0 & 0 \\ 0 & 0 \end{bmatrix} \quad (8.141)$$

$$C = \begin{bmatrix} 1 & 0 & 0 & 0 & 0 \\ 0 & 1 & 0 & 0 & 0 \end{bmatrix} \quad (8.142)$$

$$Y = \begin{bmatrix} i_{ds}^s & i_{qs}^s \end{bmatrix}^T = i_s \quad (8.143)$$

and  $V_s = [v_{ds}^s v_{qs}^s]^T$  is the input vector. Equation (8.137) is of the fifth order, where speed  $\omega_r$  is a state as well as a parameter. If speed variation is considered negligible, then  $d\omega_r/dt = 0$ . This is a valid consideration if the computational sampling time is small or load inertia is high. With speed  $\omega_r$  as a constant parameter, the machine model used in the EKF is linear. For digital implementation of an EKF, the model must be discretized in the following form:

$$X(k+1) = A_d X(k) + B_d U(k) \quad (8.144)$$

$$Y(k) = C_d X(k) \quad (8.145)$$

The induction motor model in Figure 8.49 is shown with two noise sources,  $V$  and  $W$ , which correspondingly give the model equations in discrete form as

$$X(k+1) = A_d X(k) + B_d U(k) + V(k) \quad (8.146)$$

$$Y(k) = C_d X(k) + W(k) \quad (8.147)$$

where  $V(k)$  and  $W(k)$  are zero-mean, white Gaussian noise vectors of  $X(k)$  and  $Y(k)$ , respectively. Both  $V(k)$  and  $W(k)$  are independent of  $X(k)$  and  $Y(k)$ , respectively. The statistics of noise and measurements are given by three covariance matrices,  $Q$ ,  $R$ , and  $P$ , where  $Q$  = system noise vector covariance matrix (5X5),  $R$  = measurement noise vector covariance matrix (2X2), and  $P$  = system state vector covariance matrix (5X5).

The sequence of the EKF algorithm implementation by a flow diagram is shown in Figure 8.50, which also includes the basic computational expressions. Basically, it has two main stages: prediction stage and filtering stage. In prediction stage, the next predicted values of states  $X^*(k+1)$  are calculated by the machine model and the previous values of the estimated states. In addition, the predicted state covariance matrix  $P^*(k+1)$  is also calculated using the covariance vector  $Q$ . In the filtering stage, the next estimated states  $\hat{X}(k+1)$  are obtained from the predicted states  $X^*(k+1)$  by adding the correction term  $eK$  where  $e = Y(k+1) - \hat{Y}(k+1)$  and  $K$  = Kalman gain. The Kalman gain is optimized for the state estimation errors. The EKF computations are done in recursive manner so that  $e$  approaches 0.

Due to high complexity, the computation time, even with a powerful DSP, is long and difficult to apply in real time, particularly for fast-speed variations. Besides, there is also a parameter variation problem, which makes accuracy poor at low speeds.

#### 8.5.1.6 Slot Harmonics

This is one of the simplest methods for the estimation of rotor speed. In an induction motor, the slots on the surface of the rotor provide reluctance modulation, which produces space harmonics in the air gap flux. The slot-induced ripple flux is superimposed on the fundamental flux wave. Therefore, induced stator voltage waves will contain a ripple voltage component, the frequency and magnitude of which are proportional to the rotor speed. The speed can be estimated by identifying the ripple frequency through a signal processing circuit. Due to the finite number of rotor slots and small reluctance variation, the ripple frequency and voltage magnitude become very low at low motor speeds and speed estimation becomes difficult.

#### 8.5.1.7 Injection of Auxiliary Signal on Salient Rotor

The speed estimation techniques discussed so far become impossible at zero stator frequency, that is, the dc condition when the machine speed is zero at zero torque. At pure dc condition, the rotor conditions become unobservable. However, recently, the position and speed estimation of the induction motor, which are based on the injection of an auxiliary carrier frequency signal from the stator side of a custom-designed rotor have been proposed [21]. In the proposed scheme, the machine rotor slots are to be specially designed to get spatial variation of

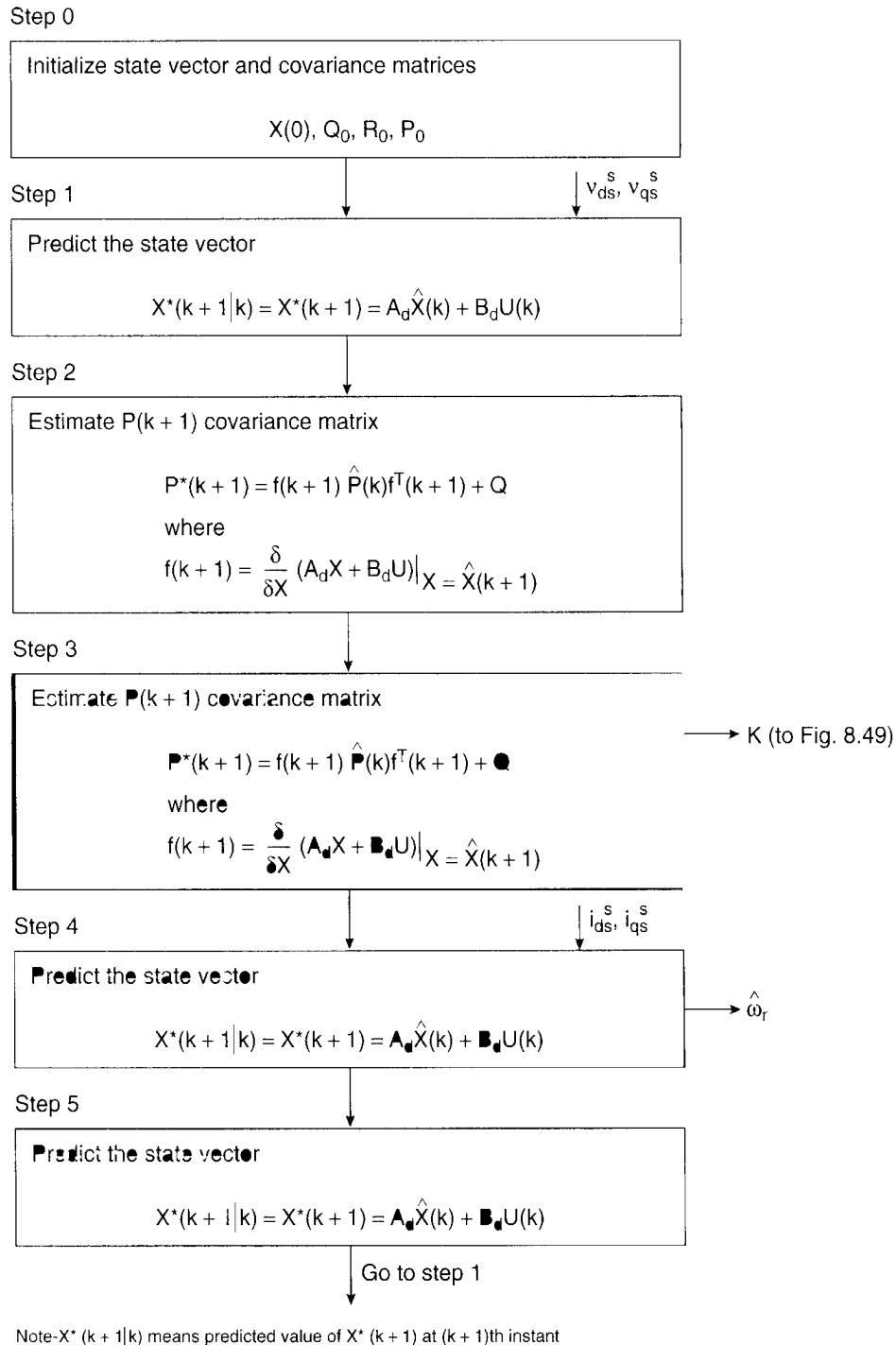


**Figure 8.50** EKF algorithm flow diagram

magnetic saliency. This is possible by a number of methods, such as variation of resistance of outer conductors, variation of depth of rotor bars, or variation of conductor heights in slot openings. The saliency of the rotor position is to be tracked by the position estimation algorithm. In this method, a carrier frequency signal (typically 250 Hz) is mixed with the usual three-phase modulating voltage signals of the inverter. The carrier does not essentially affect the drive's

performance. The high-frequency machine model with modulating leakage inductance (due to rotor anisotropy) indicates the generation of a negative sequence current component at carrier frequency that is modulated by the machine position. The machine stator currents are sensed, passed through a band-pass filter, and are then fed to a PLL system to estimate the incremental position and speed signals. The PLL system consists of a salient machine model, low-pass filter, P-I-D controller, and mechanical subsystem model with estimated load torque. The estimation algorithm is obviously very complex. The accuracy of estimation is affected by the parameter variation of the machine model, the load torque estimation error, and the inertia variation error. There is also a skin effect problem in the rotor bars due to carrier frequency. In addition, the finite phase shift in the low-pass filter to retrieve the fundamental frequency phase currents will tend to degrade the vector control. Custom designing of the rotor for speed and position estimation may not be acceptable by drive manufacturers.

### 8.5.2 Direct Vector Control without Speed Signal

In a torque-controlled drive with direct vector control, such as in electric/hybrid vehicle applications, it is possible to control the drive from zero speed (including the start-up) without using the speed signal. Such control will be described [23] with stator flux orientation.

#### 8.5.2.1 Programmable Cascaded Low-Pass Filter (PCLPF) Stator Flux Estimation

The use of the voltage model for rotor flux vector estimation was discussed before. The method uses an ideal integrator, where the dc offset voltage tends to build up at the output. The problem becomes particularly serious at the low-frequency condition. If, on the other hand, the single-stage integrator is replaced by a number of cascaded low-pass filters with short time constants for integration, the dc offset can be sharply attenuated. Consider a first-order, low-pass filter with transfer characteristics as follows:

$$\frac{Y}{X} = \frac{1}{(1 + j\tau\omega_e)} \quad (8.148)$$

where  $\tau$  = filter time constant and  $\omega_e$  = frequency. The phase lag and gain (or attenuation) of the filter at frequency  $\omega_e$  can be given, respectively, as

$$\phi = \tan^{-1}(\tau\omega_e) \quad (8.149)$$

$$K = \left| \frac{Y}{X} \right| = \frac{1}{\sqrt{1 + (\tau\omega_e)^2}} \quad (8.150)$$

If  $n$  number of filters are cascaded, the total phase shift angle and gain are given, respectively, as

$$\varphi_T = \varphi_1 + \varphi_2 + \dots + \varphi_n = \tan^{-1}(\tau_1 \omega_e) + \tan^{-1}(\tau_2 \omega_e) + \dots + \tan^{-1}(\tau_n \omega_e) \quad (8.151)$$

$$K_T = K_1 K_2 \dots K_n = \frac{1}{\sqrt{[1 + (\tau_1 \omega_e)^2][1 + (\tau_2 \omega_e)^2] \dots [1 + (\tau_n \omega_e)^2]}} \quad (8.152)$$

If all the filter stages are identical, the corresponding expressions are

$$\varphi_T = n\varphi = n \cdot \tan^{-1}(\tau \omega_e) \quad (8.153)$$

$$K_T = nK = \frac{1}{\sqrt{[1 + (\tau \omega_e)^2]^n}} \quad (8.154)$$

If the cascaded filter is required to perform integration of a sinusoidal voltage at frequency  $\omega_e$ , then  $\varphi_T = \pi/2$  and  $G \cdot K_T = 1/\omega_e$ , where  $G$  = gain compensation needed for the integration. Substituting these conditions in Equations (8.153) and (8.154), respectively,

$$\tau = \left(\frac{1}{\omega_e}\right) \tan\left(\frac{\pi}{2n}\right) \quad (8.155)$$

$$G = \left(\frac{1}{\omega_e}\right) \sqrt{[1 + (\tau \omega_e)^2]^n} \quad (8.156)$$

The above equations give the parameters  $\tau$  and  $G$  as functions of frequency. Figure 8.51 gives the equivalent op amp representation of the cascaded low-pass filter for integration, where  $\varphi_1 = \varphi_2 = \dots = \varphi_n = \pi/2n$ .

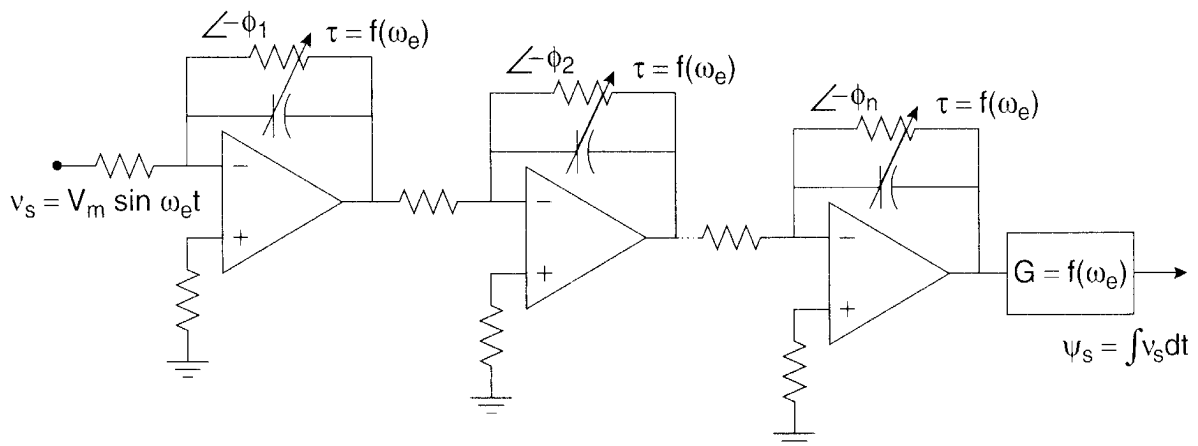


**Figure 8.51** Op amp representation of PCLPF for integration

A large number for  $n$  is desirable, but in digital implementation, the software computation burden becomes heavy. Figure 8.52 shows a three-stage PCLPF for the synthesis of stator fluxes  $\psi_{ds}^s$  and  $\psi_{qs}^s$  by solving the following equations:

$$\psi_{ds}^s = \int (v_{ds}^s - i_{ds}^s R_s) dt \quad (8.32)$$

$$\psi_{qs}^s = \int (v_{qs}^s - i_{qs}^s R_s) dt \quad (8.33)$$

Note that identical low-pass analog hardware filters are used in the front end for both the current and voltage signals (not shown here), but their effects are compensated in the PCLPF. The correct time constant and gain expressions can be derived as

$$\tau = \left( \frac{1}{\omega_e} \right) \tan \left[ \frac{1}{n} \left[ \tan^{-1}(\tau_h \omega_e) + \frac{\pi}{2} \right] \right] = f(\cdot) \omega_e \quad (8.157)$$

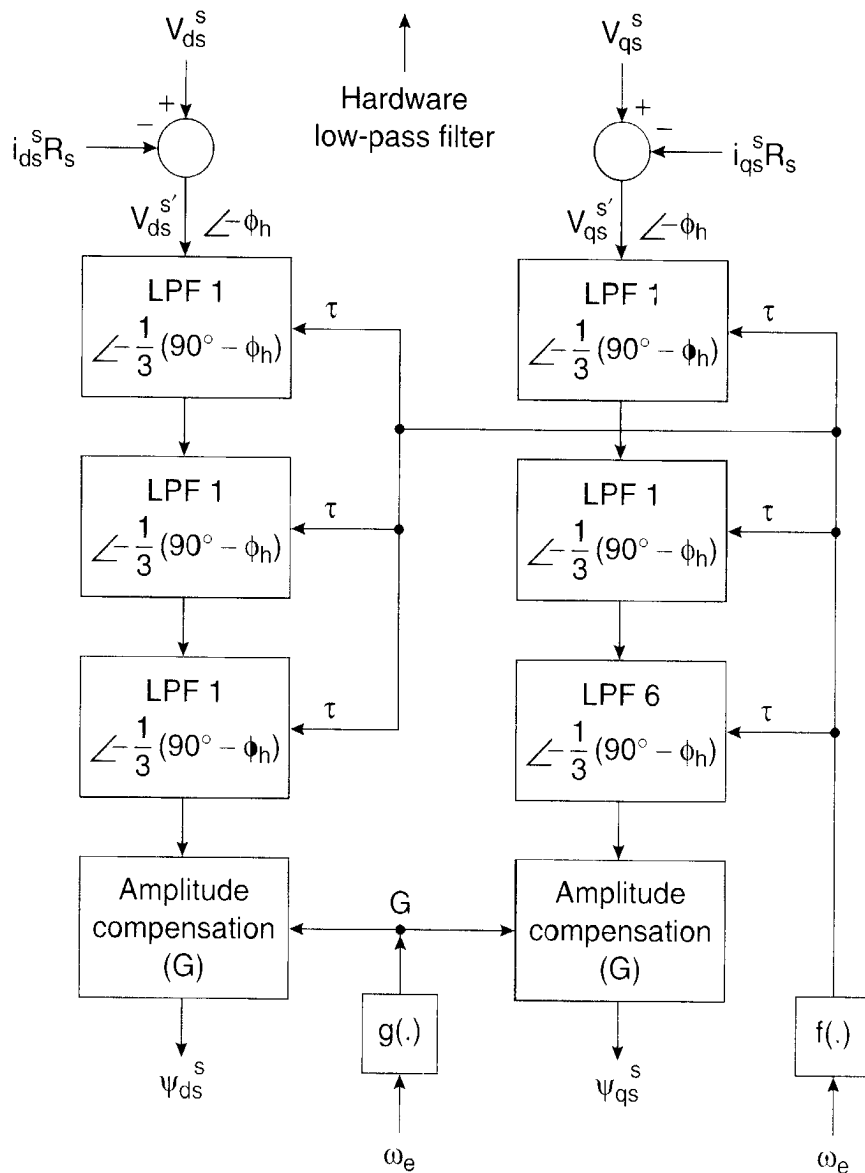


**Figure 8.52** Three-stage PCLPF based stator flux vector synthesis

$$G = \left(\frac{1}{\omega_e}\right) \sqrt{\left[1 + (\tau\omega_e)^2\right]^n \left[1 + (\tau_h\omega_e)^2\right]} = g(\cdot)\omega_e \quad (8.158)$$

where  $\tau_h$  = hardware filter time constant and  $\tan^{-1}(\tau_h\omega_e) = -\phi_h$  (phase lag due to hardware filter) is shown in the figure. If, for example,  $\phi_h = 3^\circ$  at a certain frequency, each low-pass filter (LPF) gives a phase shift angle of  $29^\circ$ , irrespective of the stator frequency variation. Since the hardware filter phase shift angle and attenuation are compensated at all frequencies, it can be designed conservatively to clean the harmonics without fear of phase drift and attenuation of signals.

Figure 8.53 shows the plot of  $\tau$  and  $G$  signals from Equations (8.157) and (8.158) for a particular value of  $\tau_h$  (in this case,  $\tau_h = 0.16$  ms). In Figure 8.52, the frequency  $\omega_e$  is solved in a circulatory manner from the equation

$$\omega_e = \frac{\left[(v_{qs}^s - i_{qs}^s R_s)\psi_{ds}^s - (v_{ds}^s - i_{ds}^s R_s)\psi_{qs}^s\right]}{\sqrt{\psi_{ds}^{s^2} + \psi_{qs}^{s^2}}} \quad (8.70)$$

and is applied to the PCLPFs for solving estimated fluxes. Note that stator resistance  $R_s$  will tend to vary with temperature and will cause an error in the estimation. The parameter can be estimated reasonably accurately using stator-mounted thermistor probes. A fuzzy logic method of  $R_s$  estimation is discussed in Chapter 11. The PCLPF method of flux vector estimation is satisfactory, typically down to a fraction of a hertz.

#### 8.5.2.2 Drive Machine Start-up with Current Model Equations

The stator flux-oriented direct vector control using PCLPF, as discussed above, is satisfactory from a fraction of a hertz of stator frequency up to the field-weakening region. However, a separate start-up control is required from zero speed stand-still condition. This is possible with the help of a current model or Blaschke equations without any speed signal as discussed below.

The stationary frame current model equations with rotor fluxes are given with standard symbols as

$$\frac{d}{dt}(\psi_{dr}^s) = \frac{L_m}{T_r} i_{ds}^s - \omega_r \psi_{qr}^s - \frac{1}{T_r} \psi_{dr}^s \quad (8.48)$$

$$\frac{d}{dt}(\psi_{qr}^s) = \frac{L_m}{T_r} i_{qs}^s + \omega_r \psi_{dr}^s - \frac{1}{T_r} \psi_{qr}^s \quad (8.49)$$

These equations are to be transformed for stator flux vector estimation so that the stator flux-oriented vector control can be used at start-up condition. Substituting the following equation pairs:

$$\psi_{dr}^s = \frac{L_r}{L_m} \psi_{dm}^s - L_{lr} i_{ds}^s \quad (8.39)$$



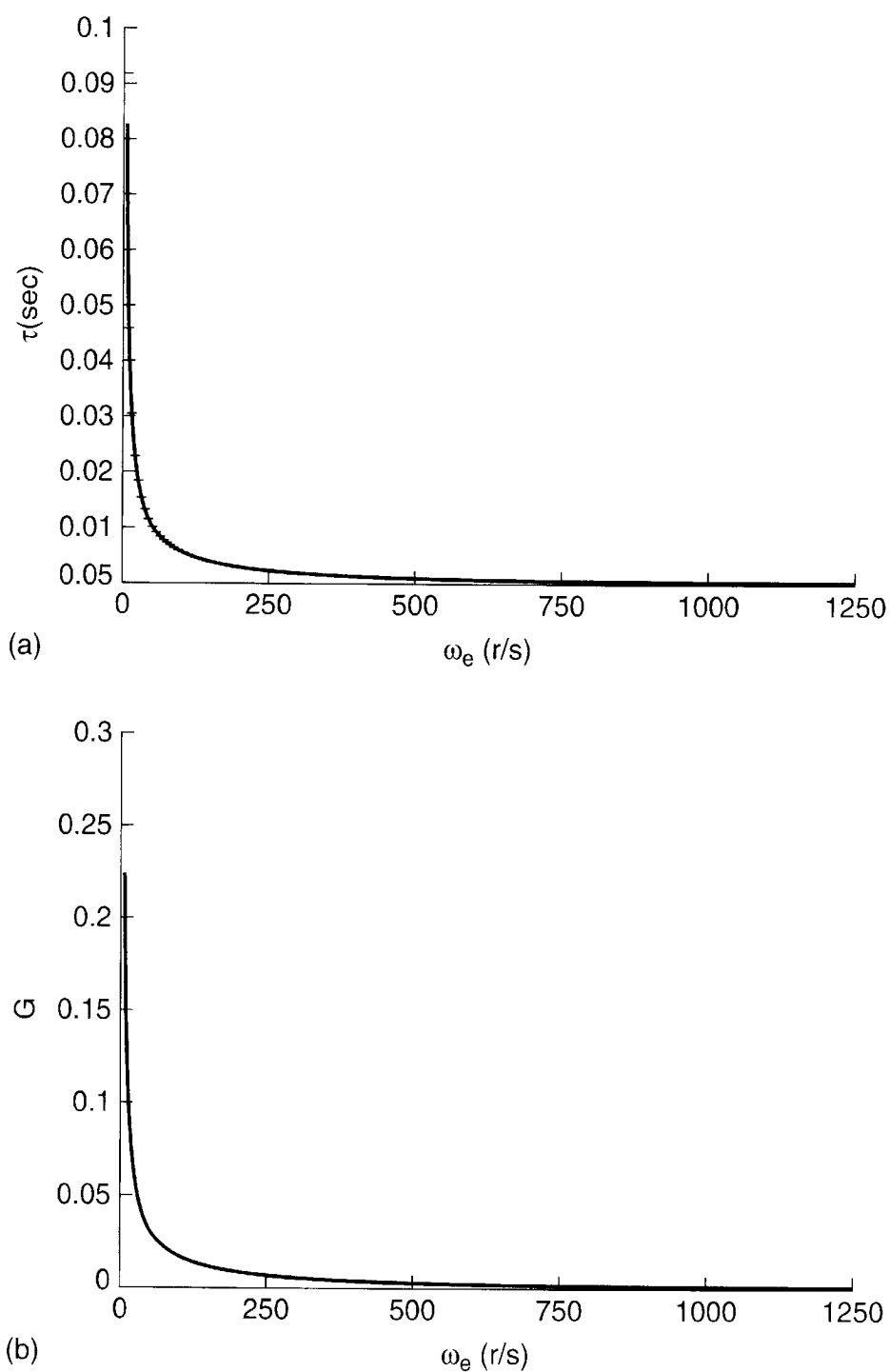


**Figure 8.53** Time constant ( $\tau$ ) and gain ( $G$ ) as function of frequency for PCLPF ( $n=3$ ) ( $\tau_h = 0.16$  ms)

$$\psi_{ds}^s = \psi_{dm}^s + L_{ls} i_{ds}^s \quad (8.159)$$

and

$$\psi_{qr}^s = \frac{L_r}{L_m} \psi_{qm}^s - L_{lr} i_{qs}^s \quad (8.160)$$

$$\psi_{qs}^s = \psi_{qm}^s + L_{ls} i_{qs}^s$$

in Equations (8.48) and (8.49) and simplifying, we get

$$\frac{d}{dt}(\psi_{ds}^s) = -\frac{1}{T_r}\psi_{ds}^s + A\frac{d}{dt}(i_{ds}^s) + Bi_{ds}^s - \omega_r(\psi_{qs}^s - Ai_{qs}^s) \quad (8.161)$$

$$\frac{d}{dt}(\psi_{qs}^s) = -\frac{1}{T_r}\psi_{qs}^s + A\frac{d}{dt}(i_{qs}^s) + Bi_{qs}^s - \omega_r(\psi_{ds}^s - Ai_{ds}^s) \quad (8.162)$$

where  $A = L_{ls} + (L_m L_{lr})/L_r$  and  $B = L_s R_r/L_r$

Equations (8.161) and (8.162) give Blaschke equations for stator flux vector estimation. These equations can be used without the speed signal at zero speed to start the machine. Substituting  $\omega_r = 0$  in the above equations, we get

$$\frac{d}{dt}(\psi_{ds}^s) = -\frac{1}{T_r}\psi_{ds}^s + A\frac{d}{dt}(i_{ds}^s) + Bi_{ds}^s \quad (8.163)$$

$$\frac{d}{dt}(\psi_{qs}^s) = -\frac{1}{T_r}\psi_{qs}^s + A\frac{d}{dt}(i_{qs}^s) + Bi_{qs}^s \quad (8.164)$$

A block diagram to solve the stator flux vectors  $\psi_{ds}^s$  and  $\psi_{qs}^s$  is shown in Figure 8.54.

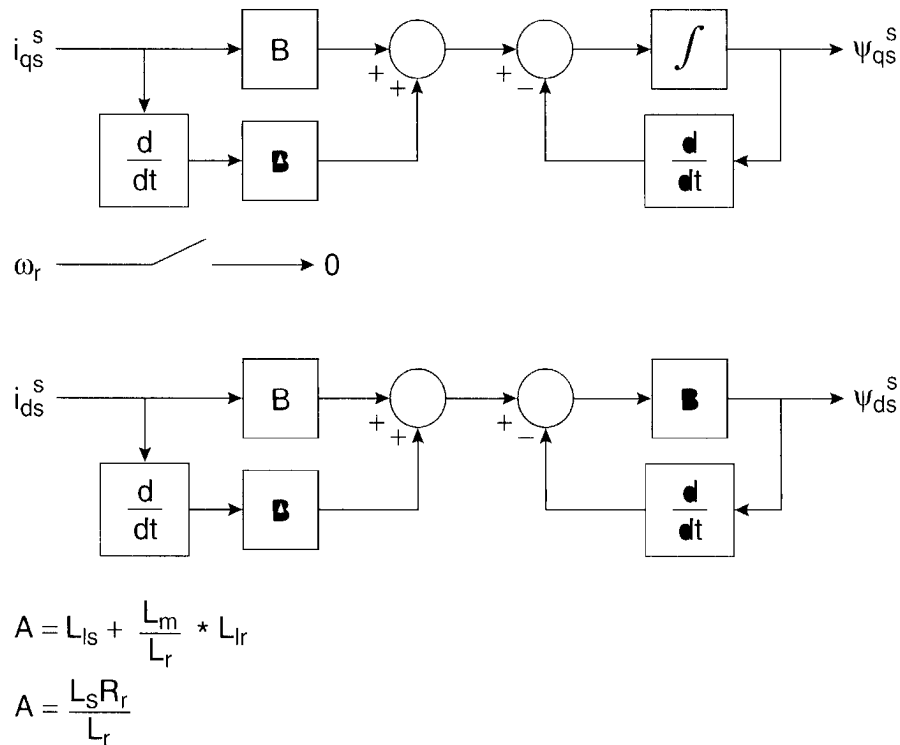


**Figure 8.54** Block diagram to solve  $\psi_{ds}^s$  and  $\psi_{qs}^s$  from Blaschke equations for start-up of drive without speed sensor

The current derivatives shown can be actually implemented with the DSP in real time, where the derivative is basically considered an increment (or decrement) in a sampling time interval for a heavily filtered current signal. Note that the models in Figure 8.54 are strictly valid at  $\omega_r = 0$ . Figure 8.55 shows the complete control block diagram, incorporating the PCLPFs and Blaschke equation start-up, as discussed above. The additional unit vector signals  $\cos \theta_e'$  and  $\sin \theta_e'$  used for the inverse rotation of stator currents are constructed with hardware filter ( $\tau_h$ ) compensation as follows:

$$\psi_{ds}^{s'} = \frac{1}{(1 + \tau_h S)} \psi_{ds}^s \quad (8.165)$$

$$\psi_{qs}^{s'} = \frac{1}{(1 + \tau_h S)} \psi_{qs}^s \quad (8.166)$$

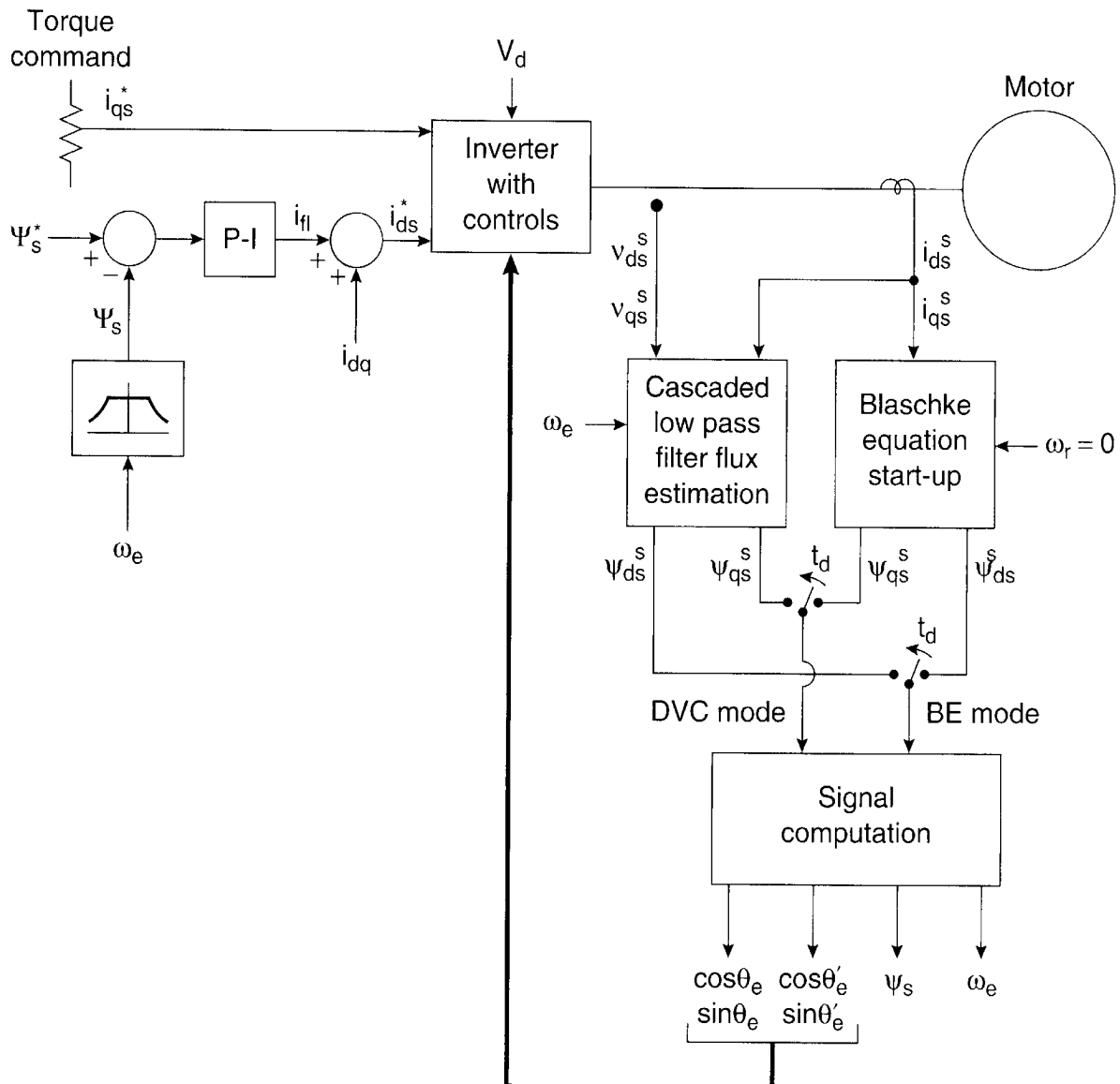


**Figure 8.55** Control block diagram of speed sensorless stator flux-oriented vector control incorporating PCLPF flux estimator and Blaschke equation start-up

$$\cos \theta_e' = \frac{\psi_{ds}^{s'}}{\sqrt{\psi_{ds}^{s'^2} + \psi_{qs}^{s'^2}}} \quad (8.167)$$

$$\sin \theta_e' = \frac{\psi_{qs}^{s'}}{\sqrt{\psi_{ds}^{s'^2} + \psi_{qs}^{s'^2}}} \quad (8.168)$$

In the beginning, the drive is in Blaschke equation (BE) mode at stand-still condition when the rated stator fluxes are established with dc stator current before applying any command torque ( $i_{qs}^*$ ). As the torque command is established at stand-still condition, the slip frequency is developed and the speed tends to develop with finite torque. The drive is transitioned to direct vector control (DVC) mode at slip frequency with a time delay (depending on the command torque) before any finite speed is developed. Figure 8.55 can also be modified for rotor flux-oriented vector control.

## 8.6 DIRECT TORQUE AND FLUX CONTROL (DTC)

In the mid-1980s, an advanced scalar control technique, known as direct torque and flux control (DTFC or DTC) or direct self-control (DSC) [24], was introduced for voltage-fed PWM inverter drives. This technique was claimed to have nearly comparable performance with vector-controlled drives. Recently, the scheme was introduced in commercial products by a major company and therefore created wide interest. The scheme, as the name indicates, is the direct control of the torque and stator flux of a drive by inverter voltage space vector selection through a lookup table. Before explaining the control principle, we will first develop a torque expression as a function of the stator and rotor fluxes.

### 8.6.1 Torque Expression with Stator and Rotor Fluxes

The torque expression given in Equation (2.121) can be expressed in the vector form as

$$\bar{T}_e = \frac{3}{2} \left( \frac{P}{2} \right) \bar{\psi}_s \times \bar{I}_s \quad (8.169)$$

where  $\bar{\psi}_s = \psi_{qs}^s - j \psi_{ds}^s$  and  $\bar{I}_s = i_{qs}^s - j i_{ds}^s$ . In this equation,  $\bar{I}_s$  is to be replaced by rotor flux  $\bar{\psi}_r$ . In the complex form,  $\bar{\psi}_s$  and  $\bar{\psi}_r$  can be expressed as functions of currents (see Figure 2.28) as

$$\bar{\psi}_s = L_s \bar{I}_s + L_m \bar{I}_r \quad (8.170)$$

$$\bar{\psi}_r = L_r \bar{I}_r + L_m \bar{I}_s \quad (8.171)$$

Eliminating  $\bar{I}_r$  from Equation (8.170), we get

$$\bar{\psi}_s = \frac{L_m}{L_r} \bar{\psi}_r + L_s' \bar{I}_s \quad (8.172)$$

where  $L_s' = L_s L_r - L_m^2$ . The corresponding expression of  $\bar{I}_s$  is

$$\bar{I}_s = \frac{1}{L_s'} \bar{\psi}_s - \frac{L_m}{L_r L_s'} \bar{\psi}_r \quad (8.173)$$

Substituting Equation (8.173) in (8.169) and simplifying yields

$$\bar{T}_e = \frac{3}{2} \left( \frac{P}{2} \right) \frac{L_m}{L_r L_s'} \bar{\psi}_r \times \bar{\psi}_s \quad (8.174)$$

that is, the magnitude of torque is

$$T_e = \frac{3}{2} \left( \frac{P}{2} \right) \frac{L_m}{L_r L_s'} |\bar{\psi}_r| |\bar{\psi}_s| \sin \gamma \quad (8.175)$$

where  $\gamma$  is the angle between the fluxes. Figure 8.56 shows the phasor (or vector) diagram for Equation (8.174), indicating the vectors  $\bar{\psi}_s$ ,  $\bar{\psi}_r$ , and  $\bar{I}_s$  for positive developed torque. If the rotor flux remains constant and the stator flux is changed incrementally by stator voltage  $\bar{V}_s$  as shown, and the corresponding change of  $\gamma$  angle is  $\Delta\gamma$ , the incremental torque  $\Delta T_e$  expression is given as

$$\Delta T_e = \frac{3}{2} \left( \frac{P}{2} \right) \frac{L_m}{L_r L_s'} |\bar{\psi}_r| |\bar{\psi}_s + \Delta \bar{\psi}_s| \sin \Delta\gamma \quad (8.176)$$

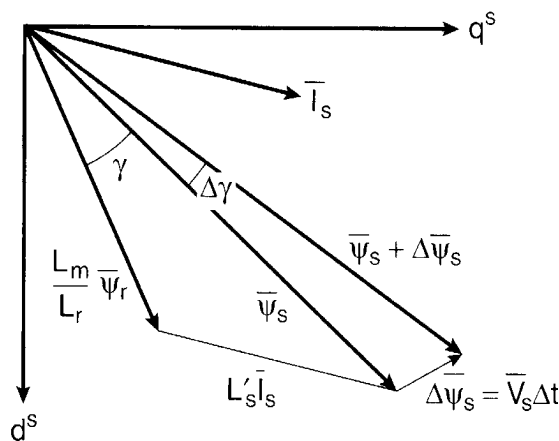


**Figure 8.56** Stator flux, rotor flux, and stator current vectors on  $d^s - q^s$  plane (stator resistance is neglected)

### 8.6.2 Control Strategy of DTC

The block diagram for direct torque and flux control is shown in Figure 8.57, and Figure 8.58 explains the control strategy. The speed control loop and the flux program as a function of speed are shown as usual and will not be discussed. The command stator flux  $\hat{\psi}_s^*$  and torque  $T_e^*$  magnitudes are compared with the respective estimated values, and the errors are processed through hysteresis-band controllers, as shown. The flux loop controller has two levels of digital output according to the following relations:

$$H_\psi = 1 \quad \text{for} \quad E_\psi > +HB_\psi \quad (8.177)$$

$$H_\psi = -1 \quad \text{for} \quad E_\psi < -HB_\psi \quad (8.178)$$

where  $2HB_\psi$  = total hysteresis-band width of the flux controller. The circular trajectory of the command flux vector  $\bar{\psi}_s^*$  with the hysteresis band rotates in an anti-clockwise direction, as shown in Figure 8.58(a). The actual stator flux  $\bar{\psi}_s$  is constrained within the hysteresis band and

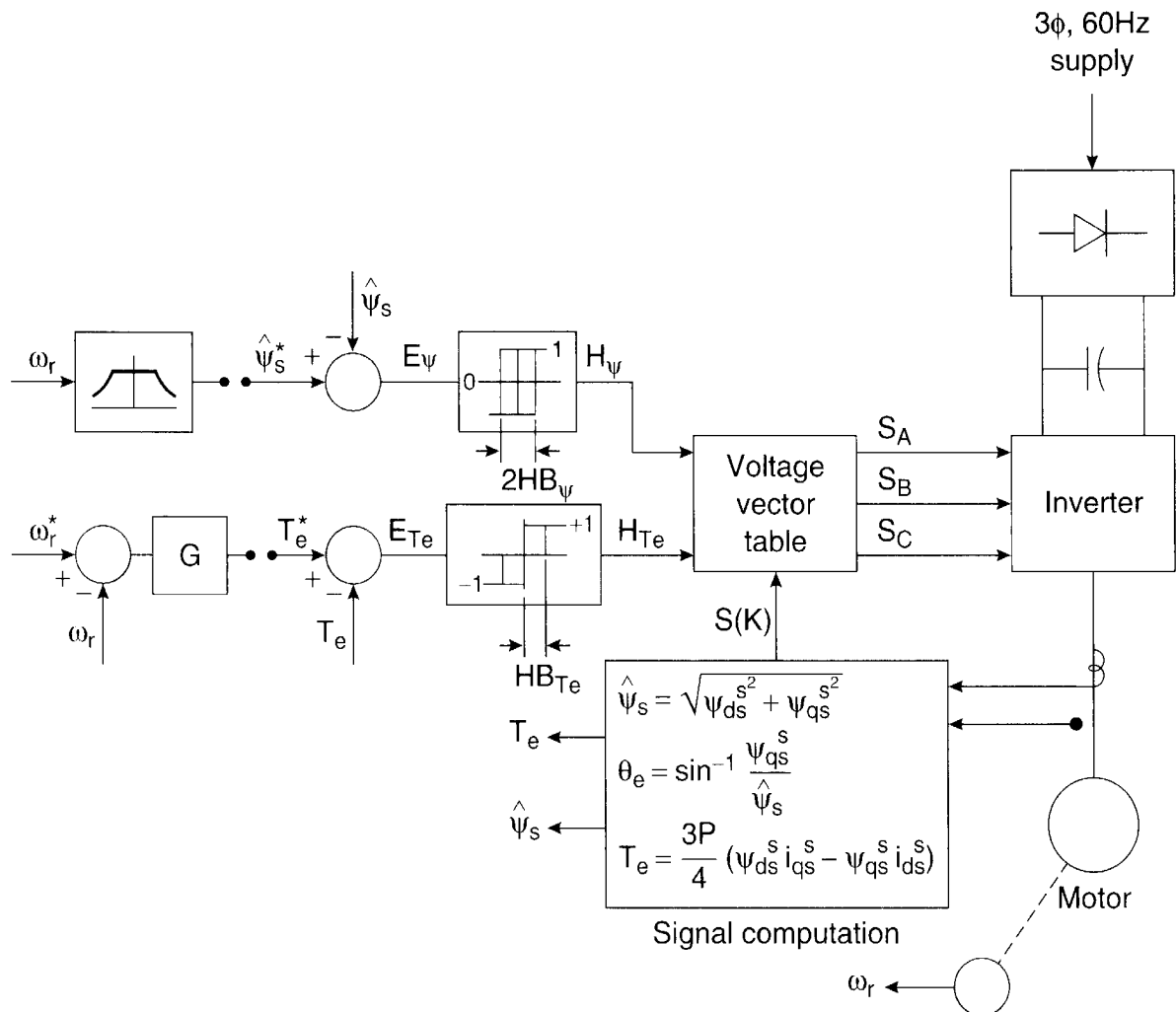
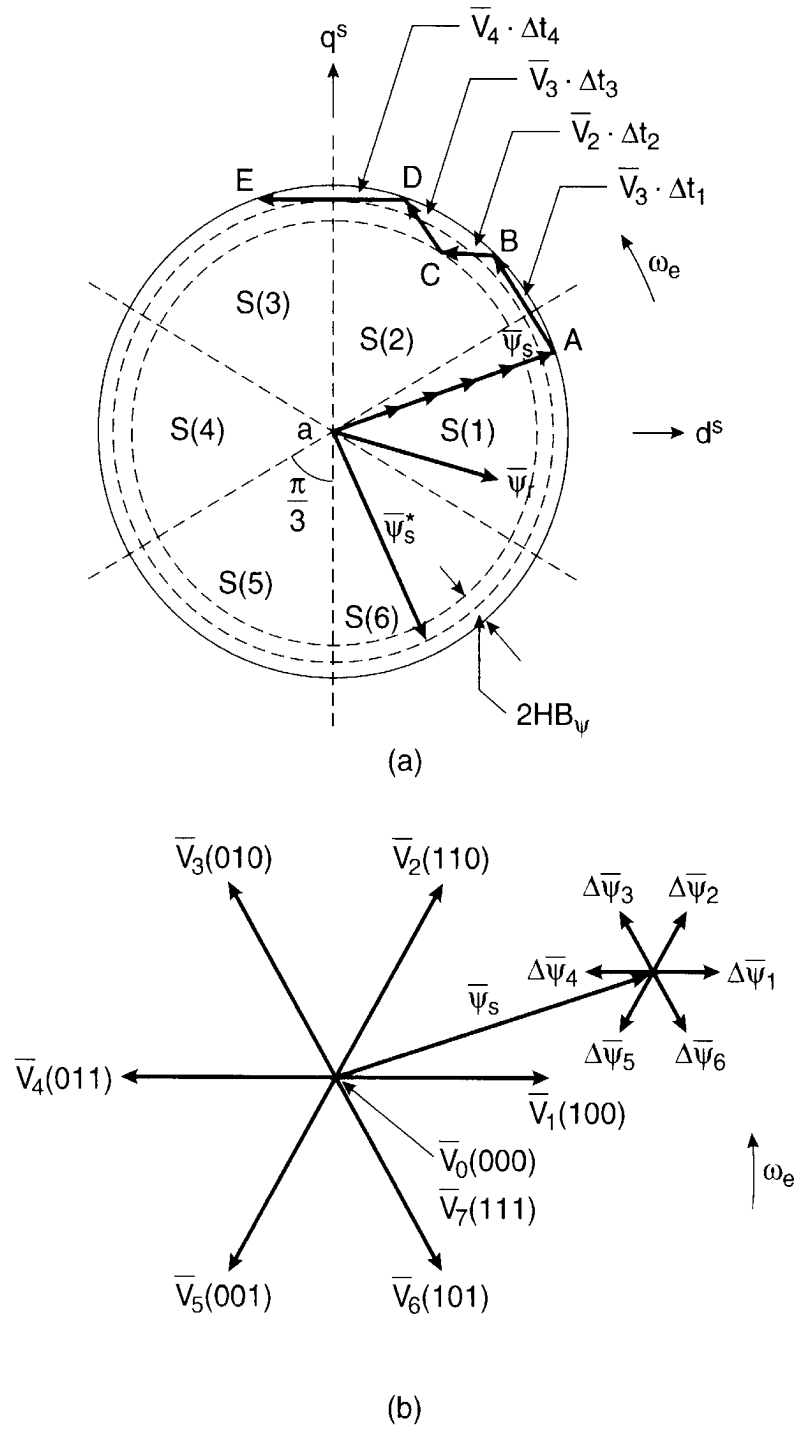


Figure 8.57 Direct torque and flux control block diagram



**Figure 8.58** (a) Trajectory of stator flux vector in DTC control, (b) Inverter voltage vectors and corresponding stator flux variation in time  $\Delta t$

it tracks the command flux in a zigzag path. The torque control loop has three levels of digital output, which have the following relations:

$$H_{Te} = 1 \quad \text{for} \quad E_{Te} > +HB_{Te} \quad (8.179)$$

$$H_{Te} = -1 \quad \text{for} \quad E_{Te} < -HB_{Te} \quad (8.180)$$

$$H_{Te} = 0 \quad \text{for} \quad -HB_{Te} < E_{Te} < +HB_{Te} \quad (8.181)$$

The feedback flux and torque are calculated from the machine terminal voltages and currents. The signal computation block also calculates the sector number  $S(k)$  in which the flux vector  $\psi_s$  lies. There are six sectors (each  $\pi/3$  angle wide), as indicated in Figure 8.58(a). The voltage vector table block in Figure 8.57 receives the input signals  $H_\psi$ ,  $H_{Te}$ , and  $S(k)$  and generates the appropriate control voltage vector (switching states) for the inverter by a lookup table, which is shown in Table 8.1 (the vector sign is deleted). The inverter voltage vectors (six active and two zero states) and a typical  $\bar{\psi}_s$  are shown in Figure 8.58(b). Neglecting the stator resistance  $R_s$  of the machine, we can write

$$\bar{V}_s = \frac{d}{dt}(\bar{\psi}_s) \quad (8.182)$$

or

$$\Delta\bar{\psi}_s = \bar{V}_s \Delta t \quad (8.183)$$

which means that  $\bar{\psi}_s$  can be changed incrementally by applying stator voltage vector  $\bar{V}_s$  for time increment  $\Delta t$ . The flux increment vector corresponding to each of the six inverter voltage vectors is shown in Figure 8.58(b). The flux in the machine is initially established at zero frequency (dc) along the radial trajectory OA shown in Figure 8.58(a). With the rated flux, the command torque is applied and the  $\bar{\psi}_s^*$  vector starts rotating. Table 8.1 applies the selected voltage vector, which essentially affects both the torque and flux simultaneously. The flux trajectory segments AB, BC, CD, and DE by the respective voltage vectors  $\bar{V}_3$ ,  $\bar{V}_4$ ,  $\bar{V}_3$ , and  $\bar{V}_4$  are shown in Figure 8.58(a). The total and incremental torque due to  $\Delta\bar{\psi}_s$  are explained in Figure 8.56. Note that the stator flux vector changes quickly by  $\bar{V}_s$ , but the  $\bar{\psi}_r$  change is very sluggish due to large time constant  $T_r$  (see Figure 8.35). Since  $\bar{\psi}_r$  is more filtered, it moves uniformly at frequency  $\omega_e$ , whereas  $\psi_s$  movement is jerky. The average speed of both, however, remains the same in the steady-state condition. Table 8.2 summarizes the flux and torque change (magnitude and direction) for applying the voltage vectors for the location of  $\bar{\psi}_s$  shown in Figure 8.58(b). The flux can be increased by the  $V_1$ ,  $V_2$ , and  $V_6$  vectors (vector sign is deleted), whereas it can be decreased by the  $V_3$ ,  $V_4$ , and  $V_5$  vectors. Similarly, torque is increased by the  $V_2$ ,  $V_3$ , and  $V_4$  vectors, but decreased by the  $V_1$ ,  $V_5$ , and  $V_6$  vectors. The zero vector ( $V_0$  or  $V_7$ ) short-circuits the machine terminals and keeps the flux and torque unaltered. Due to finite resistance ( $R_s$ ) drop, the torque and flux will slightly decrease during the short-circuit condition.

Consider, for example, an operation in sector S(2) as shown in Figure 8.58(a), where at point B, the flux is too high and the torque is too low; that is,  $H_\psi = -1$  and  $H_{Te} = +1$ . From Table 8.1, voltage  $V_4$  is applied to the inverter, which will generate the trajectory BC. At point C,  $H_\psi = +1$  and  $H_{Te} = +1$  and this will generate the  $V_3$  vector from the table. The drive can easily operate in the four quadrants, and speed loop and field-weakening control can be added, if desired. The torque



$H_\psi$	$H_{Te}$	S(1)	S(1)	S(1)	S(1)	S(1)	S(6)
1	1	1	1	1	1	1	1
	0	1	1	1	1	1	1
	1	1	1	1	1	1	1
1	1	$V_3$	$V_3$	1	1	1	1
	0	1	1	1	1	1	1
	1	1	1	1	1	1	1

**Table 8.1** Switching Table of Inverter Voltage Vectors

Voltage vector	1	1	1	1	1	1	$V_0$ or $V_7$
$\psi_s$	1	1	1	1	1	1	0
$\psi_s$	1	1	1	1	1	1	1

**Table 8.2** Flux and Torque Variations Due to Applied Voltage Vector in Figure 8.58(b)  
(Arrow indicates magnitude and direction)

response of the drive is claimed to be comparable with that of a vector-controlled drive. There are a few special features of DTC control that can be summarized as follows:

- No feedback current control
- No traditional PWM algorithm is applied
- No vector transformation as in vector control
- Feedback signal processing is somewhat similar to stator flux-oriented vector control
- Hysteresis-band control generates flux and torque ripple and switching frequency is not constant (like hysteresis-band current control)

## 8.7 ADAPTIVE CONTROL

A linear control system with invariant plant parameters can be designed easily with the classic design techniques, such as Nyquist and Bode plots. Ideally, a vector-controlled ac drive can be considered as linear, like a dc drive system. However, in industrial applications, the electrical and mechanical parameters of the drive hardly remain constant. Besides, there is a load torque disturbance effect. For example, the inertia of an electric vehicle or subway drive will vary with passenger load. In a robotic drive, on the other hand, the inertia will change, depend-

ing on the length of the arm and the load it carries. In a rolling mill drive, the drive load torque will change abruptly when a metal slab is introduced within the rolls. Figure 8.59 shows a block diagram of a speed-controlled vector drive indicating the moment of inertia  $J$  and load torque  $T_L$  variation. For the fixed control parameters in  $G$ , an increase of the  $J$  parameter will reduce the loop gain, deteriorating the system's performance. Similarly, a sudden increase of load torque  $T_L$  or  $J$  will temporarily reduce the speed until it is compensated by the sluggish speed loop. The effect of the parameter variation can be compensated to some extent by a high-gain negative feedback loop. But, excessive gain may cause an underdamping or instability problem in extreme cases. The problems discussed above require adaptation of the controller  $G$  in real time, depending on the plant parameter variation and load torque disturbance, so that the system response is not affected. Adaptive control techniques can be generally classified as

- Self-tuning control
- MRAC
- Sliding mode or variable structure control
- Expert system control
- Fuzzy control
- Neural control

In this section, the principles of adaptive control will be reviewed. Expert system, fuzzy logic, and neural network-based intelligent control techniques will be discussed in Chapters 10, 11, and 12, respectively. The application of sliding mode control in a vector drive will be discussed in somewhat detail.

### 8.7.1 Self-Tuning Control

In this method, as the name indicates, the controller parameters are tuned on-line to adapt to the plant parameter variation. A simple example of adaptive control is the loop gain scheduling in Figure 8.59, where the gain is proportional to parameter  $J$ , provided the information for the  $J$  variation is available. Another example is the slip gain ( $K_s$ ) tuning of an indirect vector-controlled drive with on-line identification of the rotor time constant  $T_r$ . Figure 8.60 gives the

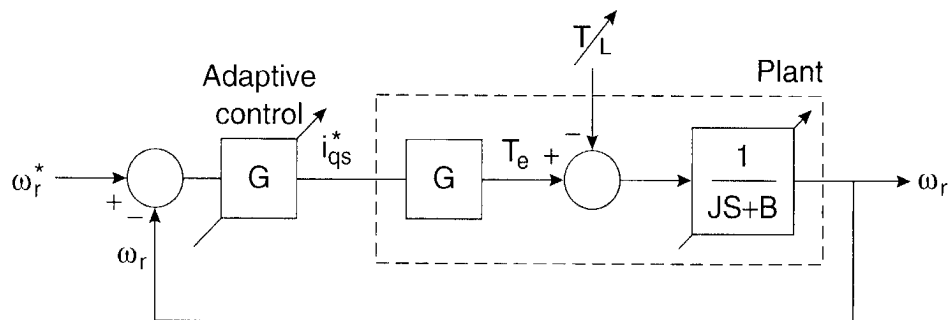


**Figure 8.59** Adaptive control block diagram for plant parameter variation and load torque disturbance

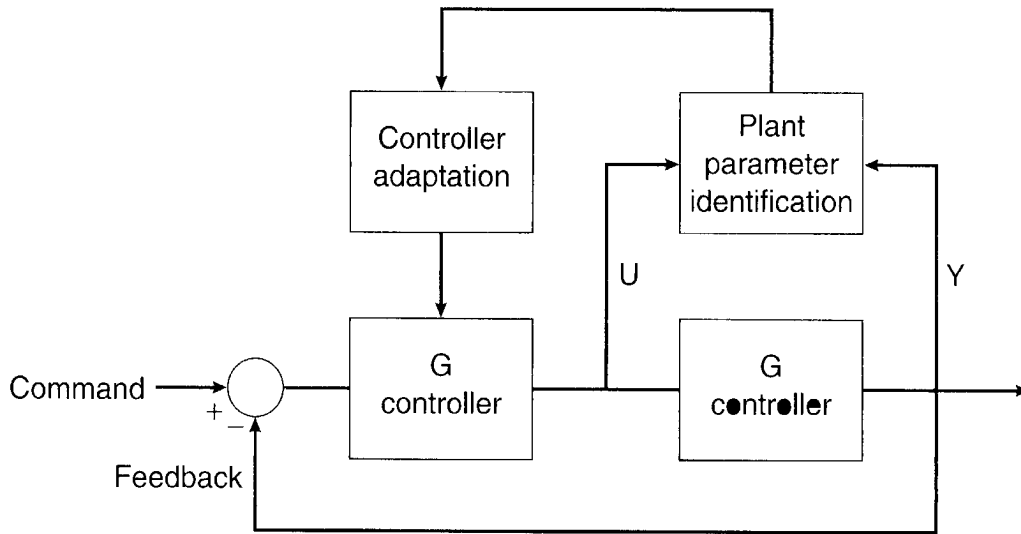


**Figure 8.60** Block diagram of self-tuning control

general block diagram for a self-tuning control. Basically, it consists of a plant parameter identification algorithm and controller adaptation algorithm. The identification algorithm estimates the varying plant parameter(s) on-line and updates the control parameters for the desired performance of the system. The controller can be P-I, P-I-D, dead-beat, pole assignment control, or pole-zero cancellation with the plant. The problems arising with P-I or P-I-D control are that no unique mathematical relation between the transfer function of the system to be controlled and the controller parameters exists. Updating must be done with the help of a search algorithm, which may be too slow for on-line adaptation. All the other controllers allow direct computation of the new controller settings based on the identified system parameters. The computational complexity and corresponding time delay may not impose much problem in a slow process control drive system, but in a fast system, rapid on-line computation becomes difficult.

#### 8.7.1.1 Load Torque Disturbance ( $T_L$ ) Compensation

As mentioned above, a sudden load or disturbance torque  $T_L$  can cause a droop in the speed in a speed-controlled drive system, which may not be desirable. The speed droop can be compensated with the help of a disturbance torque observer.

The speed and torque are given by the following relation:

$$J \frac{d\omega_m}{dt} + B\omega_m = T_e - T_L \quad (8.184)$$

where  $B$  = viscous friction coefficient. Therefore,  $T_L$  can be estimated by the following equation:

$$T_L = T_e - (JS + B)\omega_m \quad (8.185)$$

Figure 8.61 shows the estimation of the load torque and its compensation in a feedforward manner [27]. The actual speed  $\omega_m$  is measured with the measurement delay time  $T_d$ . The signal is processed through the inverse mechanical model  $(\hat{J}S + \hat{B})$  and then subtracted from the effective torque  $T_e'$  to generate the estimated torque signal  $\hat{T}_L$ . A low-pass filter is added to clean

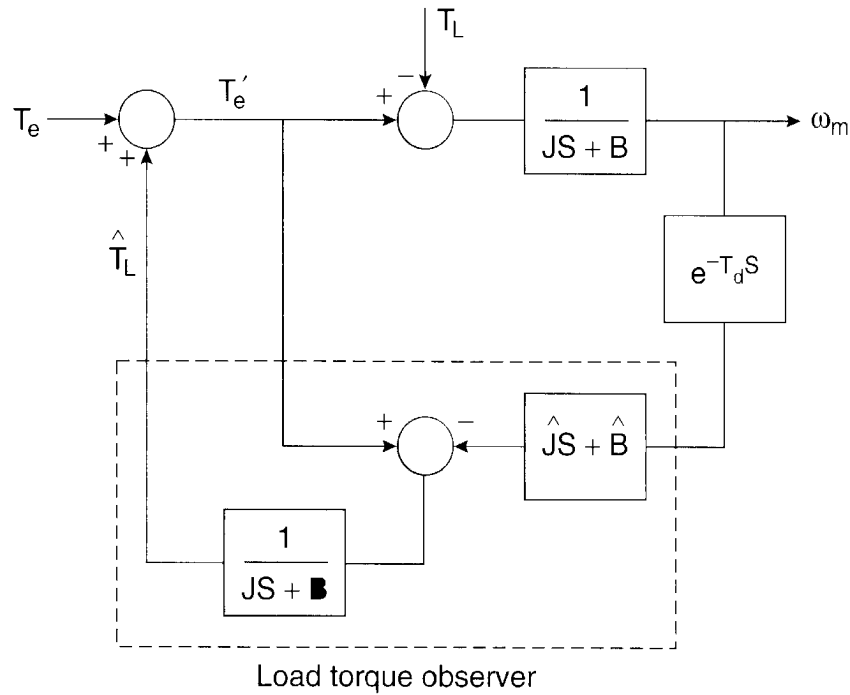


**Figure 8.61** Disturbance torque estimation and its compensation in the system

the noise generated by the inverse model (due to differentiation). The compensation will not be accurate because of the speed measurement delay, the inaccuracy of the inverse model, and the delay due to the low-pass filter. However, the compensation will be reasonably good, particularly in a high-inertia system.

### 8.7.2 Model Referencing Adaptive Control (MRAC)

The MRAC was already discussed for indirect vector control slip gain ( $K_s$ ) tuning (Figure 8.38) and speed estimation (Figure 8.47). In an MRAC, as the name indicates, the plant's response is forced to track the response of a reference model, irrespective of the plant's parameter variation and load disturbance effect. Such a system is defined as a robust system. The reference model may be fixed or adaptive and is stored in the DSP's memory.

Consider, for example, an indirect vector-controlled induction motor servo drive (Figure 8.32) and assume that the slip gain  $K_s$  has been tuned to achieve perfect decoupling. Ideally, the model of such a drive is identical to that of a dc machine. The position loop response of the system can be given by a second-order transfer function. A typical response for such a drive system with variable inertia ( $J_2 > J_1$ ) load is shown in Figure 8.62. Such a response variation may be undesirable in some applications. The problem can be solved by the MRAC system shown in Figure 8.63. The speed command  $\omega_r^*$ , generated by the position control loop, is applied in parallel to the reference model and plant controller as shown. The reference model output speed  $\omega_{rm}$  is compared with the measured plant speed  $\omega_r$ , and the resulting error signal  $e$  along with the  $\omega_r$  signal actuates the adaptation algorithm. The feedforward and feedback gains  $K_F$  and  $K_B$ , respectively, of the plant controller are iterated by the adaptation algorithm dynamically so as to

reduce the error  $e$  to zero. The algorithm contains P-I-type control law so that the desired  $K_F$  and  $K_B$  parameter values are locked in the integrator when the error vanishes to zero. The plant will be capable of tracking the reference model without saturation provided that the  $J$  parameter in the reference model is defined on the worst-case (maximum) basis (i.e., slowest response) for a variable-inertia plant load.

The MRAC profile for maximum inertia  $J_2$  is indicated in Figure 8.62. With a fixed machine-converter power rating, the drive will fail to meet the desired acceleration-deceleration profile if actual inertia exceeds  $J_2$ . If the plant inertia is  $J_1$  ( $J_1 < J_2$ ), the drive will have suboptimal transient response. Thus, the robustness of an MRAC system is obtained at the sacrifice of optimum response. Besides, there is the chattering problem on the speed signal, which is somewhat smoothed for the position signal because of integration. If chattering can be tolerated, an MRAC is applicable to a speed control system.

The adaptation algorithm can be defined as [29]

$$K_F = K_{FO} + FV\omega_r^* + \int_0^t GV\omega_r^* dt \quad (8.186)$$

$$K_B = K_{BO} + LV\omega_r + \int_0^t MV\omega_r dt \quad (8.187)$$

$$V = De \quad (8.188)$$

where  $K_{FO}$  and  $K_{BO}$  are the initial gain values and  $F$ ,  $G$ ,  $L$ ,  $M$ , and  $D$  are the adaptation law constants. In general, the structure of the reference model and the plant should be the same and the parameters should be compatible for satisfactory adaptation. In Figure 8.63, the state equations for the reference model and the plant, respectively, can be given as

$$\frac{d}{dt}(\omega_{rm}) = A_m\omega_{rm} + B_m\omega_r^* \quad (8.189)$$

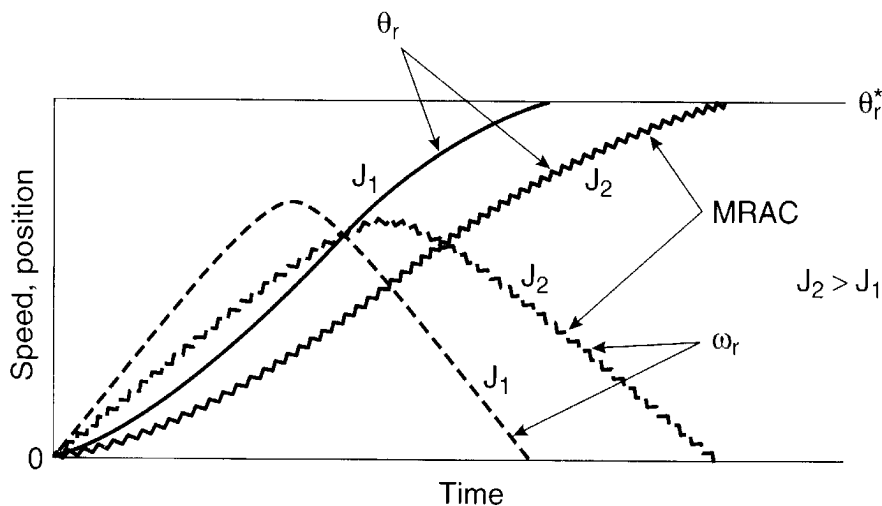


**Figure 8.62** Response variation of servo drive with variation of moment of inertia  $J$

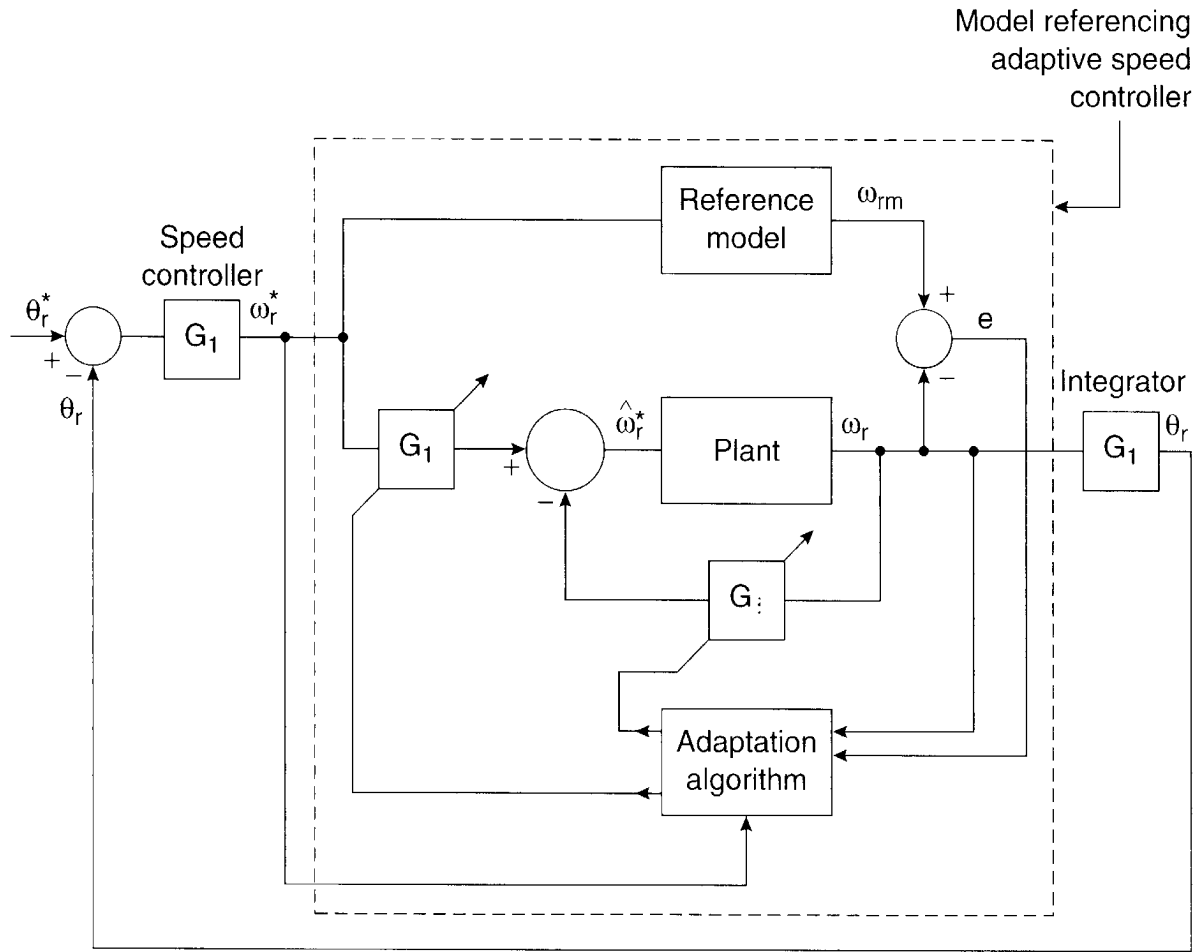


**Figure 8.63** Servo drive with model referencing adaptive speed control

$$\frac{d}{dt}(\omega_r) = A_p \omega_r + B_p \hat{\omega}_r \quad (8.190)$$

and the other control loop equations are

$$\omega_r^* = G_1(\theta_r^* - \theta_r) \quad (8.191)$$

$$\hat{\omega}_r^* = K_F \omega_r^* - K_B \omega_r \quad (8.192)$$

$$e = \omega_{rm} - \omega_r \quad (8.193)$$

Note that the control parameters  $K_F$  and  $K_B$  are time-varying. The speed control system within the dashed line in Figure 8.63 can be represented by an equivalent feedforward time-invariant linear system with a feedback, nonlinear, time-varying block. The global stability of the system can be analyzed by Popov's hyperstability theorem, and correspondingly, parameters  $F$ ,  $G$ ,  $L$ ,  $M$ , and  $D$  can be determined. An MRAC with a neural network will be discussed in Chapter 12.

### 8.7.3 Sliding Mode Control

A sliding mode control (SMC) with a variable control structure is basically an adaptive control that gives robust performance of a drive with parameter variation and load torque disturbance. The control is nonlinear and can be applied to a linear or nonlinear plant. In an SMC, as the name indicates, the drive response is forced to tract or “slide” along a predefined trajectory or “reference model” in a phase plane by a switching control algorithm, irrespective of the plant’s parameter variation and load disturbance. The control DSP detects the deviation of the actual trajectory from the reference trajectory and correspondingly changes the switching strategy to restore the tracking. In performance, it is somewhat similar to an MRAC, as described before, but the design and implementation of an SMC are somewhat simpler. SMCs can be applied to servo drives with dc motors, induction motors, and synchronous motors for applications such as robot drives, machine tool control, etc. In this section, we will review the principles of the SMC without going into rigorous theoretical aspects [31]. Then, we will apply it to a vector-controlled induction motor servo drive.

#### 8.7.3.1 Control Principle

An SMC is basically a variable structure control system (VSS) where the structure or topology of the control is intentionally varied to stabilize the control and make its response robust. Consider a simple second-order undamped linear system, as shown in Figure 8.64, with variable plant gain  $K$ . It can easily be seen that the system is unstable in either negative or positive feedback mode. However, by switching back and forth between the negative and positive feedback modes, the system cannot only be made stable, but its response can be made independent to the plant parameter  $K$ .

Consider Figure 8.64 in negative feedback mode with switch 1 closed. We can write

$$X_1 = R - C \quad (8.194)$$

or

$$R - X_1 = C \quad (8.195)$$

where  $X_1$  = loop error.

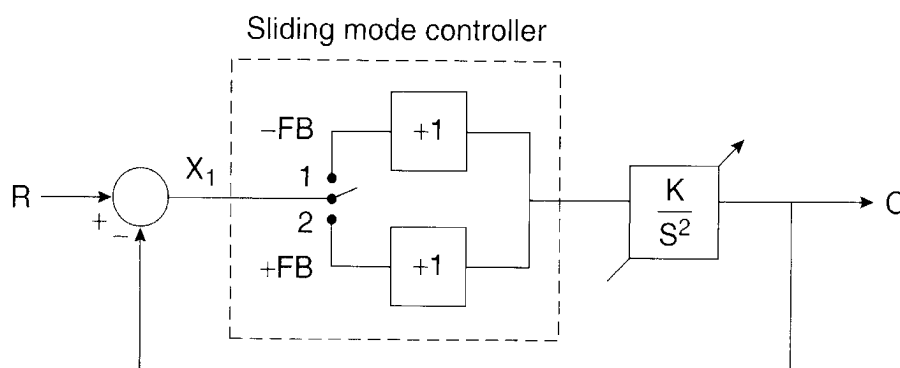


**Figure 8.64** Variable structure control of second-order system

Differentiating Equation (8.195),

$$\frac{d}{dt}(R - X_1) = \frac{dC}{dt} = -X_2 \quad (8.196)$$

or

$$\frac{dX_1}{dt} = X_2 \quad (8.197)$$

where  $R$  = step input with constant value at time  $t+$  and  $-X_2 = dC/dt$ .

We can also write the derivative of  $X_2$  in the following form to satisfy the loop relation:

$$\frac{dX_2}{dt} = -KX_1 \quad (8.198)$$

Combining Equations (8.197) and (8.198),

$$\frac{d^2 X_1}{dt^2} + KX_1 = 0 \quad (8.199)$$

which gives the second-order system model in terms of the loop error  $X_1$  and its derivative  $X_2$ .

The general solution of the undamped equation, (8.199), is

$$X_1 = A \sin(\sqrt{K}t + \theta) \quad (8.200)$$

$$X_2 = \frac{dX_1}{dt} = \sqrt{K}A \cos(\sqrt{K}t + \theta) \quad (8.201)$$

where  $A$  and  $\theta$  are arbitrary constants. Combining them, we get

$$\frac{X_1^2}{A^2} + \frac{X_2^2}{(\sqrt{K}A)^2} = 1 \quad (8.202)$$

Equation (8.202) describes an ellipse with semi-axes  $A$  and  $\sqrt{K}A$ . Its phase plane trajectory is plotted in Figure 8.65, which shows concentric ellipses with arbitrary  $A$ . The shape of the ellipses will vary with a variation of gain  $K$ .

In the positive feedback mode (switch 2 closed) of Figure 8.64, we can write the following equations:

$$\frac{dX_1}{dt} = X_2 \quad (8.203)$$

$$\frac{dX_2}{dt} = KX_1 \quad (8.204)$$



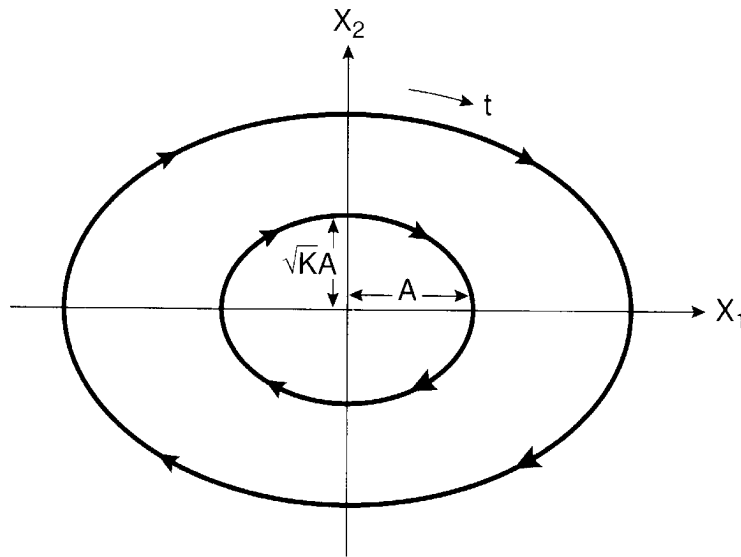


**Figure 8.65** Phase plane portrait of Figure 8.64 with negative feedback

Combining these equations,

$$\frac{d^2 X_1}{dt^2} - KX_1 = 0 \quad (8.205)$$

The general solution of Equation (8.205) is

$$X_1 = B_1 e^{\sqrt{K}t} + B_2 e^{-\sqrt{K}t} \quad (8.206)$$

$$X_2 = \frac{dX_1}{dt} = \sqrt{K} B_1 e^{\sqrt{K}t} - \sqrt{K} B_2 e^{-\sqrt{K}t} \quad (8.207)$$

where  $B_1$  and  $B_2$  are arbitrary constants. Squaring each equation and combining them gives us

$$\frac{X_1^2}{4B_1 B_2} - \frac{X_2^2}{4KB_1 B_2} = 1 \quad (8.208)$$

where term  $B_1 B_2$  can be positive, negative, or zero. Equation (8.208) describes hyperbolas that are plotted in the phase plane of Figure 8.66. The straight line asymptote equations can be derived by substituting  $B_1 B_2 = 0$  as

$$KX_1^2 - X_2^2 = 4KB_1 B_2 = 0 \quad (8.209)$$

i.e.

$$X_2 = \pm \sqrt{K} X_1 \quad (8.210)$$

The families of hyperbolas are plotted for  $B_1 B_2 > 0$  and  $B_1 B_2 < 0$ . The system can be switched back and forth between the positive and negative feedback modes for SMC, as

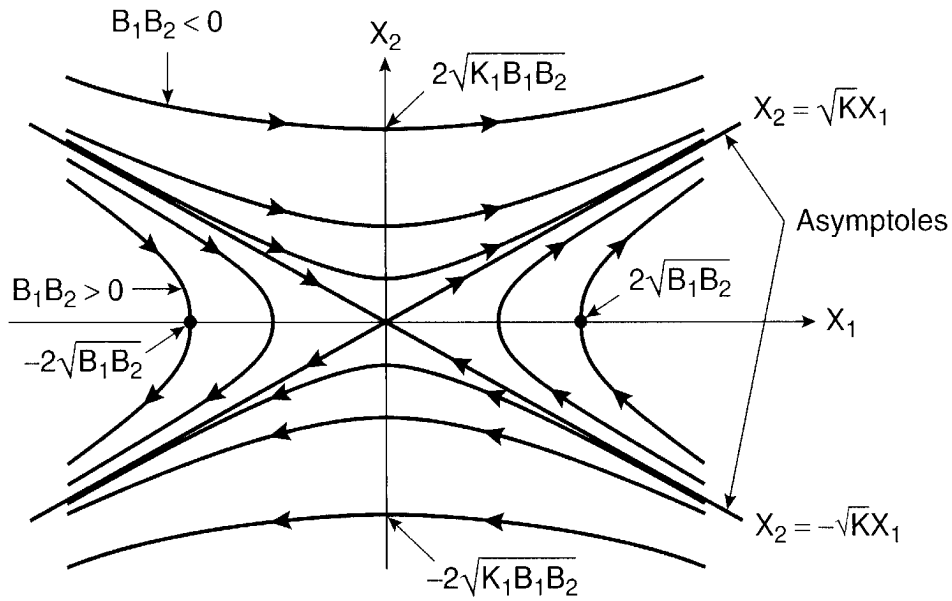


**Figure 8.66** Phase plane portrait of Figure 8.64 with positive feedback

explained in Figure 8.67. The operation in Figure 8.67 can be understood by the superposition of Figures 8.65 and 8.66, where the hyperbolic asymptote line is described by the equation

$$\sigma = \sqrt{K}X_1 + X_2 = 0 \quad (8.211)$$

where  $\sigma = 0$  is on the line.

Assume that initially, the system is in negative feedback mode and the operating point is at  $X_1 = X_{10}$  on the ellipse. As the operating point moves on an elliptic trajectory and touches point B as shown, the positive feedback mode is invoked. Ideally, it will then move along the straight line  $BO$  and settle at steady-state point  $O$ , where error  $X_1$  and error velocity  $X_2$  are zero. The slope of line  $BO$  may vary with a variation of  $K$ . Even with a constant  $K$ , precision switching at point B is practically impossible to reach the steady-state point  $O$ . Let us define the sliding line equation as

$$\sigma = CX_1 + X_2 = 0 \quad (8.212)$$

where  $C < \sqrt{K}$  so that the line slope is lower and beyond the range of the  $K$  variation. Note carefully that on the sliding line, defined as the “reference trajectory,” the positive and negative feedback trajectories, described by hyperbolas and ellipses, respectively, cross in opposite directions. This means that at point  $B'$ , the control can be switched to positive feedback mode, and then at point  $D$ , it can be switched back to negative feedback mode, and so on. The operating point will thus track the sliding line in a zigzag path until the steady-state point is reached at the origin. The time-domain solution of the sliding line is basically a deceleration with exponentially decaying  $X_1$ , as indicated by the following equation:

$$X_1(t) = X_1(t_0)e^{-C(t-t_0)} \quad (8.213)$$

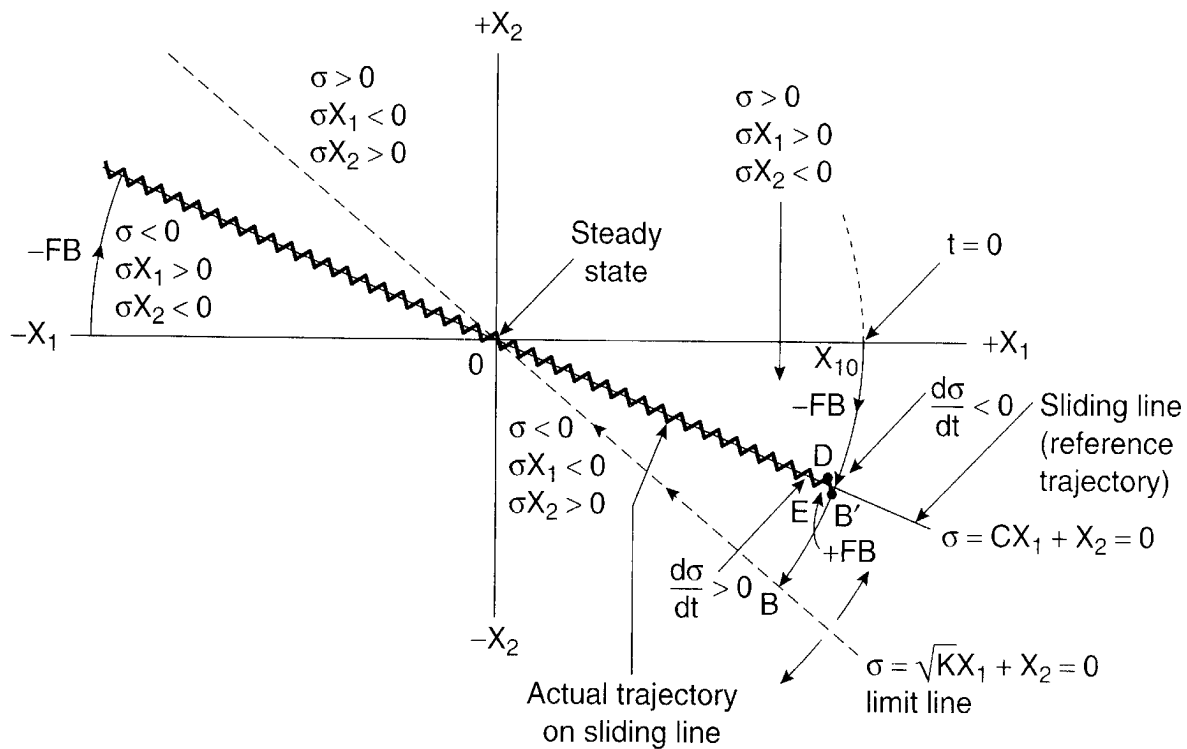


**Figure 8.67** Sliding line control in phase plane  $X_1 - X_2$

where  $t_0$  = time at which the trajectory reaches the sliding line. The time-domain response for the sliding line control of two different values of  $C$  is shown in Figure 8.68, which reflects the characteristic chattering effect. Note that once the operation reaches the sliding line, the response is strictly dictated by slope  $C$ , but it is not affected by a variation of parameter  $K$  or any load disturbance (robust). The operation of the sliding line control in the second quadrant for  $-X_1$  (reverse position error) is similar to that for the fourth quadrant, and is shown in Figure 8.67.

The polarities of parameters  $\sigma$ ,  $\sigma X_1$ , and  $\sigma X_2$  above and below the sliding line for both  $+X_1$  and  $-X_1$  are summarized in Figure 8.67. The strategy of switching control is defined by

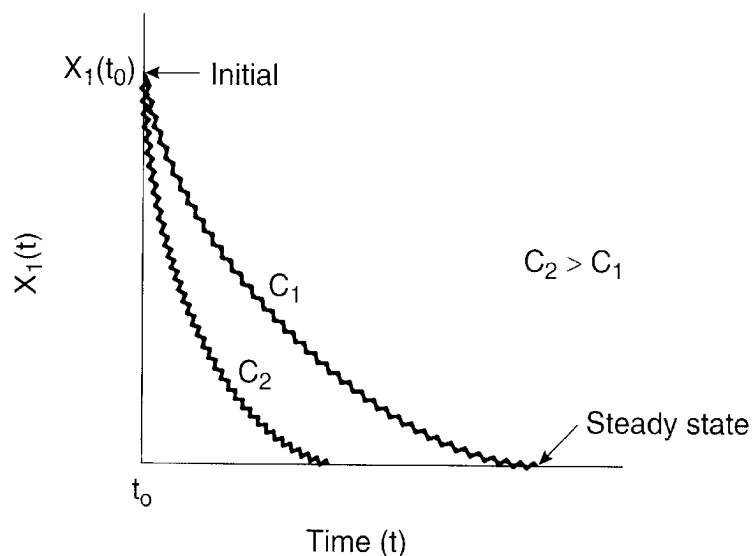


**Figure 8.68** Time-domain response in sliding line control for two different values of  $C$

these polarities, which will be described later. Evidently,  $\sigma > 0$  and  $d\sigma/dt < 0$ , as the trajectory tends to cross the sliding line from above, whereas  $\sigma < 0$  and  $d\sigma/dt > 0$ , as the trajectory tends to cross the line from below. Mathematically, we can write

$$\lim \frac{d\sigma}{dt} < 0 \quad \text{for} \quad \sigma \rightarrow +0 \quad (8.214)$$

and

$$\lim \frac{d\sigma}{dt} > 0 \quad \text{for} \quad \sigma \rightarrow -0 \quad (8.215)$$

Combining Equations (8.214) and (8.215), we get

$$\lim \sigma \frac{d\sigma}{dt} < 0 \quad \text{for} \quad \sigma \rightarrow 0 \quad (8.216)$$

Equation (8.216) is defined as an existence or reaching equation, which must be satisfied for the SMC. In other words, the validity of the reaching equation guarantees that the response will cross the trajectory in each switching transition, and is essential for a system to be controllable by the sliding mode. In practice, the parameters in the sliding mode controller are designed with the reaching equation, which will be discussed later.

### 8.7.3.2 Sliding Trajectory Control of a Vector Drive

We will now apply an SMC to a vector-controlled induction motor servo drive and develop design criteria for the controller's parameters. In addition, the sliding line control will be extended to a full sliding trajectory control, incorporating acceleration, constant speed, and deceleration segments. Figure 8.69 shows the block diagram of an ideal dc machine-like transfer function model of a vector drive that incorporates a sliding mode control. The idea is to make the response insensitive to the plant parameters, that is, the torque constant  $K_t$ , moment of inertia  $J$ , friction damping coefficient  $B$ , and load torque disturbance  $T_L$ . Assuming a step command of  $\theta_r^*$ , we can write the following equations:

$$T_e = K_t i_{qs} = K_t K_1 U \quad (8.217)$$

$$X_1 = \theta_r^* - \theta_r \quad (8.218)$$

$$\frac{dX_1}{dt} = \frac{d\theta_r^*}{dt} - \frac{d\theta_r}{dt} = -\omega_m = X_2 \quad (8.219)$$

$$(T_e - T_L) \frac{1}{JS + B} = -X_2 \quad (8.220)$$

where  $U$  = SMC output and  $K_1$  = control gain for active current  $i_{qs}^*$ .

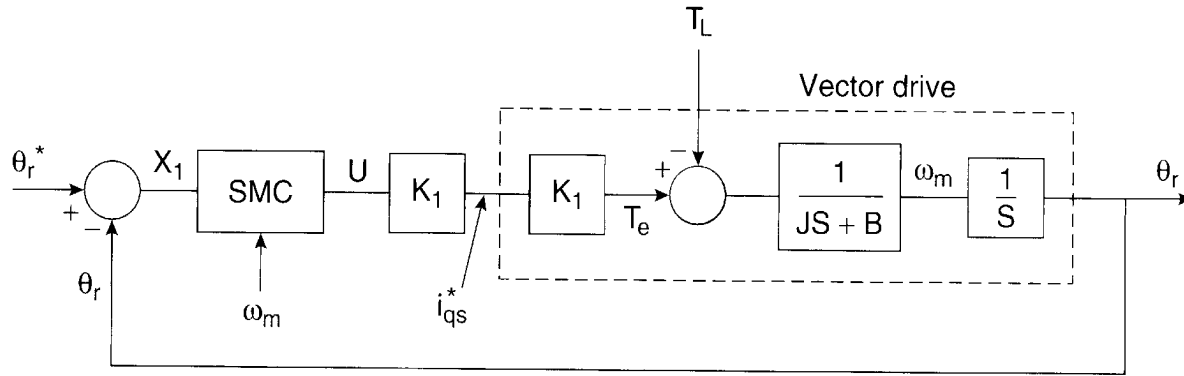


**Figure 8.69** Vector-controlled induction motor servo drive with sliding mode control

The second-order plant model is expressed in state-space equations in terms of state variables  $X_1$  and  $X_2$  by the following steps:

$$JSX_2 + BX_2 = -K_t K_1 U + T_L \quad (8.221)$$

$$\frac{dX_2}{dt} = -\frac{B}{J} X_2 - \frac{K_t K_1}{J} U + \frac{1}{J} T_L \quad (8.222)$$

$$\begin{bmatrix} \frac{dX_1}{dt} \\ \frac{dX_2}{dt} \end{bmatrix} = \begin{bmatrix} 0 & 1 \\ 0 & -b \end{bmatrix} \begin{bmatrix} X_1 \\ X_2 \end{bmatrix} + \begin{bmatrix} 0 \\ -a \end{bmatrix} U + \begin{bmatrix} 0 \\ d \end{bmatrix} T_L \quad (8.223)$$

where  $b = B/J$ ,  $a = K_t K_1/J$ , and  $d = 1/J$ . Figure 8.70 shows the proposed sliding mode control topology in detail, and Figure 8.71 shows the corresponding trajectory control for the acceleration, constant speed, and deceleration segments for both the  $+X_1$  and  $-X_1$  regions. Note that the  $X_2$  signal is directly derived from speed signal  $\omega_m$ .

There are essentially three control loops in Figure 8.70. The main or primary loop receives the position loop error  $X_1$  signal and generates  $U_1$  output through the switching controller with respective gains  $\alpha_i$  and  $\beta_i$ . The secondary control loop with derivative input  $dX_1/dt = X_2$  generates signal  $U_2$ . The input in this loop is derived directly from the motor speed signal  $\omega_m$ , as indicated. In addition to these loops, there is an auxiliary loop where constant  $A$  is injected to eliminate the steady-state error due to coulomb friction and load torque  $T_L$ . In a sliding mode controller, all the input signals are transmitted through single-pole double-throw (SPDT) switches, and the criteria for controlling each switch are indicated on the figure. All the loops contribute to the respective signals and the resultant signal  $U$  is

$$U = U_0 + U_1 + U_2 \quad (8.224)$$

In Figure 8.71, the outer curve is determined by the limiting values of the acceleration, speed, and deceleration of the drive system. Normally, the variation of plant parameters will cause drift within a band as shown by the dashed lines. For example, if the inertia  $J$  is increased, the max-

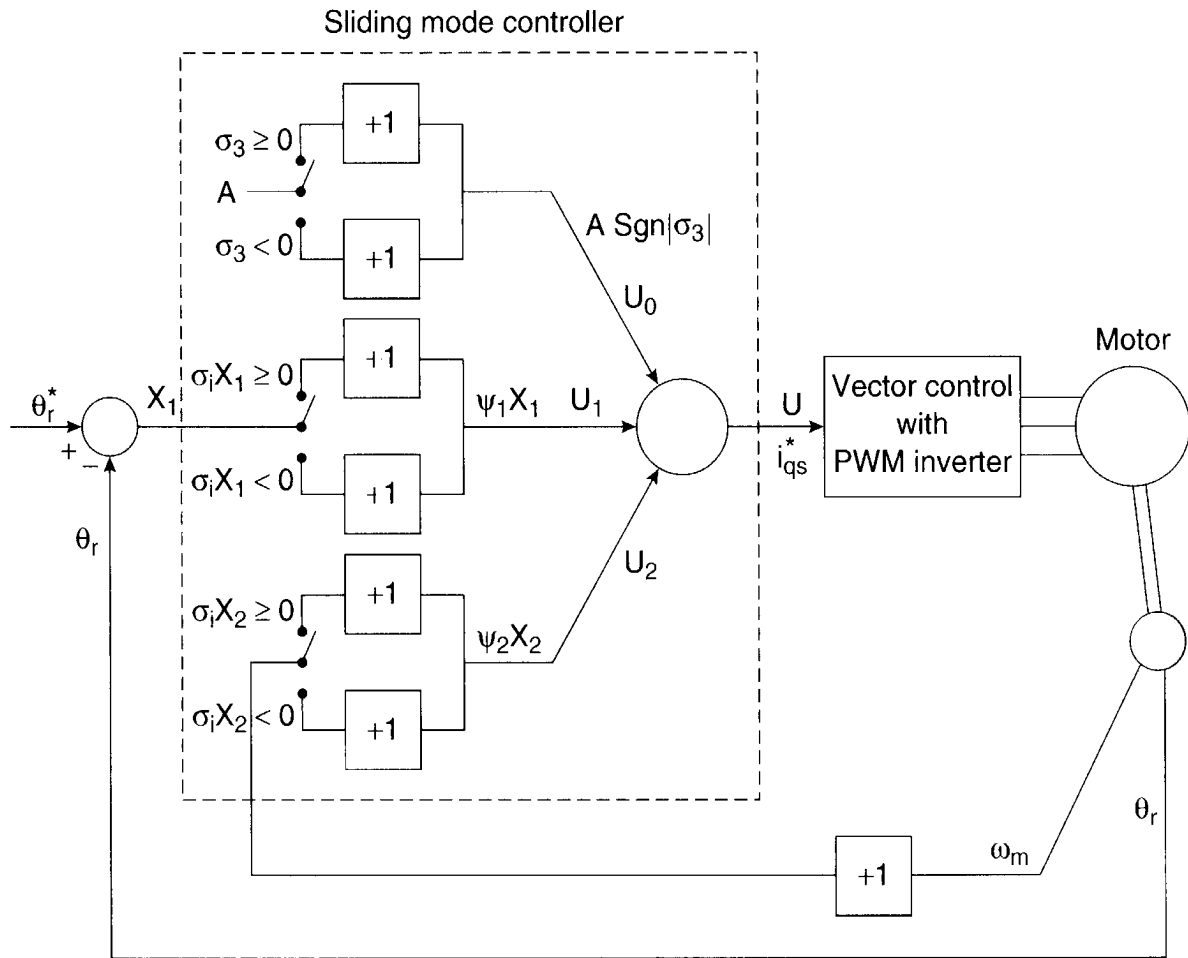


**Figure 8.70** Induction motor drive showing sliding mode controller in detail

imum acceleration and deceleration limits will shrink. The sliding trajectory or reference contour in phase plane  $X_1 - X_2$ , which the drive system will be forced to track, must be described beyond the drift band so that the system becomes controllable and the response is not affected by the drift. The sliding trajectory defined here consists of three segments, and their equations in the fourth quadrant (forward position error) are described as follows:

### 1. Acceleration segment:

$$\sigma_1 = \alpha X_2^2 + (X_1 - X_{10}) \quad (8.225)$$

where  $X_{10}$  = initial position error

### 2. Constant speed segment:

$$\sigma_2 = X_2 - X_{20} \quad (8.226)$$

where  $-X_2$  corresponds to positive speed and  $-X_{20}$  = maximum positive speed ( $|X_{20}| < |V_m|$ )

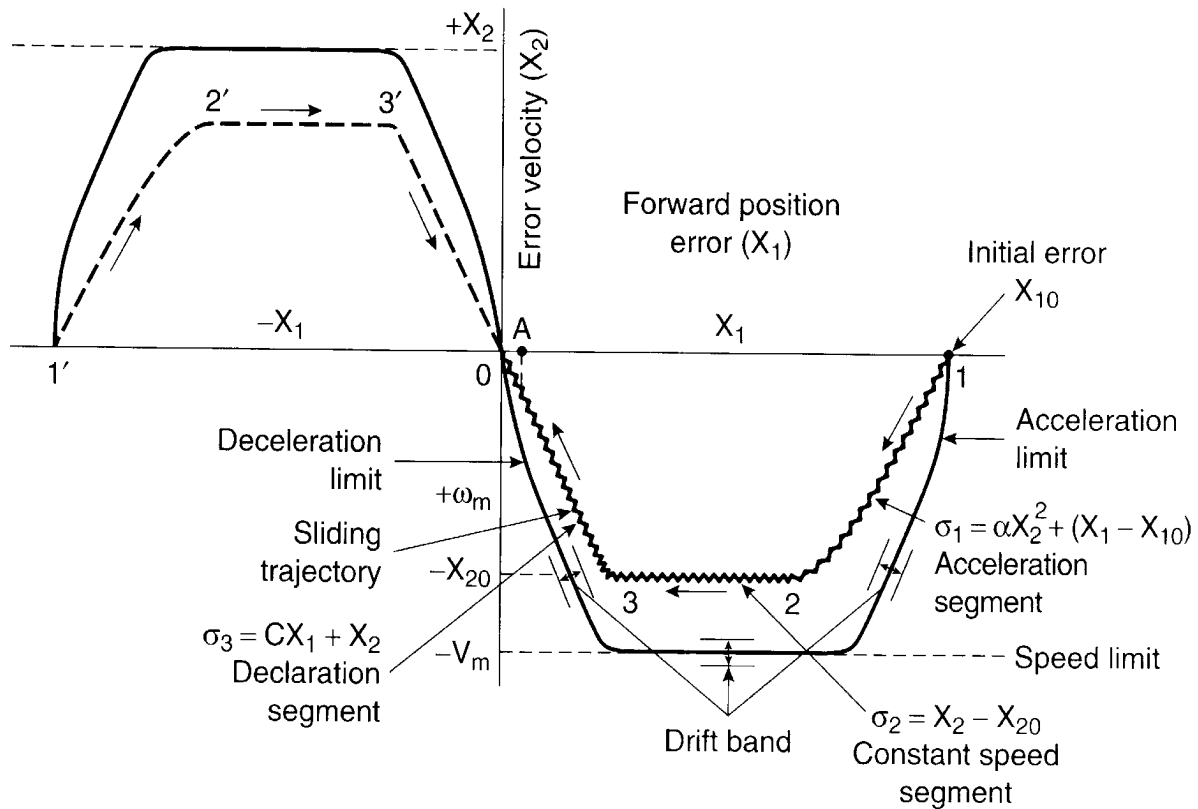


**Figure 8.71** Sliding trajectory of drive in acceleration, constant speed, and deceleration segments

### 3. Deceleration segment:

$$\sigma_3 = CX_1 + X_2 \quad (8.227)$$

which corresponds to the sliding line in Figure 8.67. All the sliding control parameters generally vary with the selection of the segment. Note that in each case,  $\sigma = 0$  means the reference trajectory. The actual trajectory that follows the reference trajectory is given by the zig-zag profile in the direction of the arrow, as shown. At steady state, the operating point oscillates at the origin of the phase plane. The trajectory should be defined as close as possible to the limit envelope, but beyond the drift band so as to get the best suboptimal transient response. It can be shown [31] that a second-order system theoretically requires only error signal  $X_1$  and its derivative  $X_2$  as control inputs, as shown in Figure 8.70.

The SMC law can be defined mathematically as

$$U = A \cdot \text{Sgn} |\sigma_3| + \psi_1 X_1 + \psi_2 X_2 \quad (8.228)$$

where

$$\begin{aligned} \text{Sgn} |\sigma_3| &= +1 & \text{if } \sigma_3 \geq 0 \\ &= -1 & \text{if } \sigma_3 < 0 \end{aligned} \quad (8.229)$$

$$\begin{aligned}\psi_1 &= \alpha_i & \text{if } \sigma_i X_1 \geq 0 \\ &= \beta_i & \text{if } \sigma_i X_1 < 0\end{aligned}\quad (8.230)$$

$$\begin{aligned}\psi_2 &= \gamma_i & \text{if } \sigma_i X_2 \geq 0 \\ &= \xi_i & \text{if } \sigma_i X_2 < 0\end{aligned}\quad (8.231)$$

as indicated in Figure 8.70.

Let us now take the individual sliding trajectory segments in Figure 8.71 and derive the relations of the control parameters of the primary and secondary control loops. In each segment, the validity of reaching Equation (8.216) will guarantee the success of the SMC.

Consider first the deceleration segment given by Equation (8.227). Differentiating this equation and substituting in (8.216), we get

$$\sigma_3 \left( C \frac{dX_1}{dt} + \frac{dX_2}{dt} \right) < 0 \quad (8.232)$$

But, the state-space equations of the system from (8.223) can be written as

$$\frac{dX_1}{dt} = X_2 \quad (8.233)$$

$$\frac{dX_2}{dt} = -bX_2 - aU + dT_L \quad (8.234)$$

Substituting Equations (8.233) and (8.234) in (8.232) and replacing  $U$  by the relation

$$U = \psi_1 X_1 + \psi_2 X_2 \quad (8.235)$$

we get

$$-\sigma_3 X_1 (a\psi_1) - \sigma_3 X_2 (b + a\psi_2 - C) + \sigma_3 dT_L < 0 \quad (8.236)$$

For validity of this equation, the following control relations should be satisfied:

### 1. Primary loop:

$$\text{If } \sigma_3 X_1 > 0, \text{ then } a\alpha_3 > 0, \text{ that is, } \alpha_3 > 0 \quad (8.237)$$

$$\text{If } \sigma_3 X_1 < 0, \text{ then } a\beta_3 < 0, \text{ that is, } \beta_3 < 0 \quad (8.238)$$



## 2. Secondary loop:

$$\text{If } \sigma_3 X_2 > 0, \text{ then } (b + a\gamma_3 - C) > 0, \text{ that is, } \gamma_3 > \frac{(C - b)}{a} \quad (8.239)$$

$$\text{If } \sigma_3 X_2 < 0, \text{ then } (b + a\xi_3 - C) < 0, \text{ that is, } \xi_3 < \frac{(C - b)}{a} \quad (8.240)$$

These equations indicate that control parameter selection in an SMC is very flexible. It appears safe to consider  $\alpha_3$  and  $\gamma_3$  as positive and  $\beta_3$  and  $\xi_3$  as negative values. It is better to design the preliminary values of control parameters and then optimize by simulation and experiment. For a wide variation of plant parameters, the control parameters can be adapted, if necessary.

Now, consider the constant speed segment of the trajectory given by Equation (8.226). Differentiating this equation and substituting (8.234), we get

$$\frac{d\sigma_2}{dt} = \frac{dX_2}{dt} = -bX_2 - aU + dT_L \quad (8.241)$$

Substituting equations (8.241) and (8.235) in (8.216)

$$-\sigma_2 X_1 (a\psi_1) - \sigma_2 X_2 (b + a\psi_2 - dT_L) < 0 \quad (8.242)$$

## 1. Primary loop:

$$\text{If } \sigma_2 X_1 > 0, \text{ then } a\alpha_2 > 0, \text{ that is, } \alpha_2 > 0 \quad (8.243)$$

$$\text{If } \sigma_2 X_1 < 0, \text{ then } a\beta_2 < 0, \text{ that is, } \beta_2 < 0 \quad (8.244)$$

## 2. Secondary loop:

$$\text{If } \sigma_2 X_2 > 0, \text{ then } (b + a\gamma_2 - dT_L) > 0, \text{ that is, } \gamma_2 > \frac{(dT_L - b)}{a} \quad (8.245)$$

$$\text{If } \sigma_2 X_2 < 0, \text{ then } (b + a\xi_2 - dT_L) < 0, \text{ that is, } \xi_2 < \frac{(dT_L - b)}{a} \quad (8.246)$$

Again, it appears safe to select  $\alpha_2$  and  $\gamma_2$  as positive and  $\beta_2$  and  $\xi_2$  as negative values.

Now, consider the acceleration segment in the fourth quadrant. Substituting the derivative of Equation (8.225) in (8.216),

$$\sigma_1 \frac{d\sigma_1}{dt} = \sigma_1 (2\alpha X_2 \frac{dX_2}{dt} + \frac{dX_1}{dt}) < 0 \quad (8.247)$$

Substituting Equations (8.233)–(8.235) in (8.247),

$$-\sigma_1 X_1 (2\alpha a \psi_1 X_2) + \sigma_1 X_2 (-2\alpha b X_2 - 2\alpha a \psi_2 X_2 + 2\alpha d T_L + 1) < 0 \quad (8.248)$$

Since  $X_2$  is always negative in the fourth quadrant, we can write the following equations:

### 1. Primary loop:

$$\text{If } \sigma_1 X_1 > 0, \text{ then } 2\alpha a \alpha_1 < 0, \text{ that is, } \alpha_1 < 0 \quad (8.249)$$

$$\text{If } \sigma_1 X_1 < 0, \text{ then } 2\alpha a \beta_1 > 0, \text{ that is, } \beta_1 > 0 \quad (8.250)$$

### 2. Secondary loop:

$$\text{If } \sigma_1 X_2 > 0, \text{ then } \gamma_1 > -\frac{(1 + 2\alpha d T_L + 2\alpha b |X_2|)}{2\alpha a |X_2|} \quad (8.251)$$

$$\text{If } \sigma_1 X_2 < 0, \text{ then } \xi_1 < -\frac{(1 + 2\alpha d T_L + 2\alpha b |X_2|)}{2\alpha a |X_2|} \quad (8.252)$$

It can be shown that an SMC becomes valid using the primary loop only. However, the secondary loop with a derivative input improves system response and permits a wider variation of plant parameters.

The “dither signal”  $U_0 = A \text{Sgn} |\sigma_3|$  is activated in the deceleration segment only. The signal is bipolar with a mean average value and strengthens the primary loop output in steady-state condition. Without this loop, the drive will have a steady-state position error ( $X_1$ ) with load torque  $T_L$  and coulomb friction because the developed torque with  $i_{qs}$  current is supplied by the primary loop error  $X_1$  only. The dither input permits  $X_1 = 0$  at steady state when the operating point oscillates in the origin. However, the disadvantage of the dither signal is that it enhances the chattering effect.

The chattering effect of an SMC may not be acceptable in many applications. Chattering in torque and speed may be large, but its effect is small on position because of inertia filtering. Chattering can be improved by a small computation sampling time, higher PWM frequency, and by minimizing any additional delay in feedback signal computation.

## 8.8 SELF-COMMISSIONING OF DRIVE

Self-commissioning of a drive involves the initial measurement of machine parameters for feedback signal estimation and tuning the control system. Traditionally, machine equivalent circuit parameters are determined by no-load and blocked rotor (or short-circuit) tests with 60 Hz voltage injection in the stator. Information about the parameters is important for the estimation of feedback signals (see Figs. 8.29 and 8.30) and slip gain tuning (see Figure 8.32) of vector-controlled drives. The proportional ( $P$ ) and integral ( $I$ ) gains of feedback control loops

can also be tuned with knowledge of the machine's parameters. This means that if the transfer function model of a plant is known with the plant parameters, the optimum  $P$  and  $I$  gains can be determined.

Note that in self-commissioning, we are concerned with initial plant parameters only, not the parameters during operating condition, which might change. Instead of P-I tuning of the loops with the knowledge of plant parameters, the tuning can also be done by observing the loop's response in real time. Expert system and fuzzy logic-based P-I tuning will be discussed in Chapters 10 and 11, respectively. For a digitally controlled drive with an unknown machine, a software routine can automate the whole parameter measurement procedure saving many man-hours.

Let us consider, for example, a direct vector-controlled drive with space vector PWM which has speed loop, flux loop, and synchronous current control loops, as shown in Figure 8.72. The motor has a speed encoder that helps to estimate the rotor flux vector starting from zero speed (current model estimation). Of course, the flux vector can also be estimated with the voltage model. Let us discuss the whole procedure of self-commissioning step-by-step [34].

### Step 1: Feed name plate machine parameters

Initially, with the machine at rest, dial into the microcomputer's memory the rated voltage  $V_s$ , rated current  $I_s$ , rated frequency  $\omega_e$ , and number of poles  $P$  of the machine.

### Step 2: Measure stator resistance ( $R_s$ )

- Set up the  $i_{ds}$  control loop ( $i_{qs}$  loop deactivated) with 100 percent dc stator current.
- Select the inverter voltage vector (say)  $V_1$  and PWM modulation index  $m_1$  so that the rated stator current is established. Note the current value of  $I_{s1}$ .

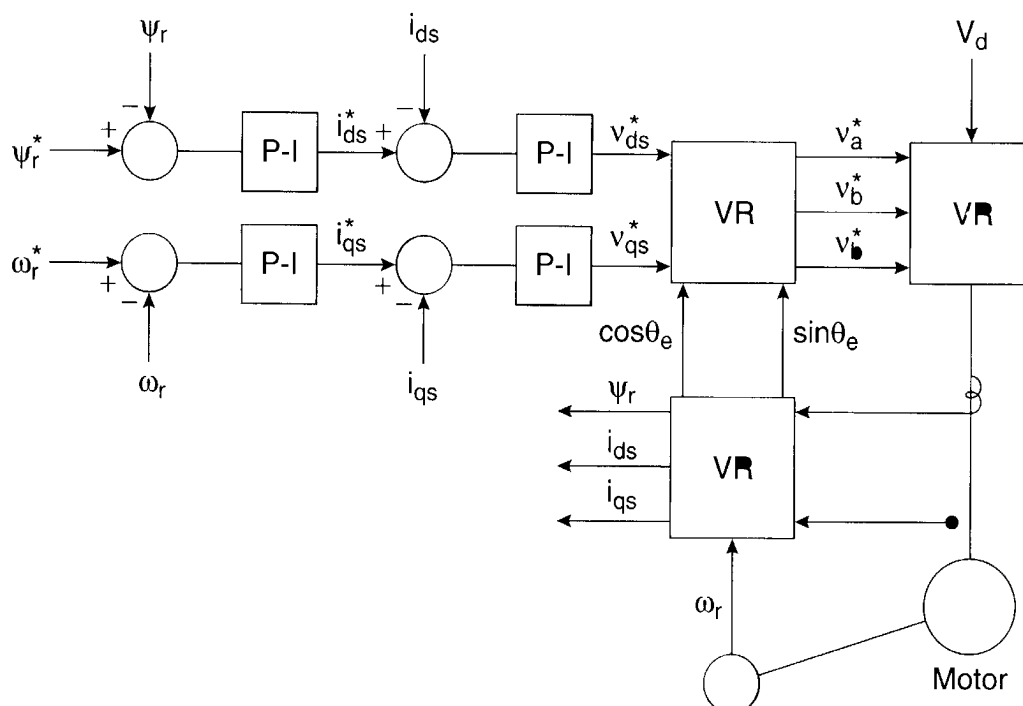


**Figure 8.72** Direct vector controlled drive with speed, flux and synchronous current control

- Repeat the above step for 50 percent stator current with modulation index  $m_2$ . Note the value of  $I_{s2}$ .
- Calculate  $R_s = (V_1.m_1 - V_1.m_2)/(I_{s1} - I_{s2})$ . The effect of distortion and inverter dead time is cancelled by the two-step measurement.

### Step 3: Measure stator transient parameters

- Select voltage vector  $V_1$ . Disable the PWM modulator. Apply the voltage for a short time  $t_1$  (in  $\mu s$ ), as shown in Figure 8.73. The resulting current response  $i_s$  is approximately linear.

Referring to the equivalent circuit Figure 2. 28(a), the transient loop equation is

$$\bar{V}_s = Ri_s + L \frac{di_s}{dt} \quad (8.253)$$

where  $R = R_s + R_r$  and  $L = L_{ls} + L_{lr}$

If the resistance drop is neglected, that is, the current rise is linear, the transient inductance  $L$  is given as

$$L = \frac{\bar{V}_s \Delta t}{\Delta \bar{I}_s} \quad (8.254)$$

Both  $R$  and  $L$  can be determined from the following solution of Equation (8.253) by measuring  $i_s$  for two different times  $t_1$  and  $t_2$ . Make a few tests and calculate the average.

$$i_s(t) = \frac{\bar{V}_s}{R} \left[ 1 - e^{-\frac{t}{\tau}} \right] \quad (8.255)$$

where  $\tau = L/R$ .

### Step 4: Tune the current loops

- Tune the  $i_{ds}$  and  $i_{qs}$  loops in Figure 8.72 one at a time. Note that the currents are perpendicular but do not have an orientation with rotor flux. Figure 8.74 shows the  $i_{qs}$  loop, where  $K_{IN}$  = inverter voltage gain and  $L/(R + LS)$  is the transient equivalent circuit transfer function. Determine the optimum P and I gains.
- Repeat the same for the  $i_{ds}$  loop.

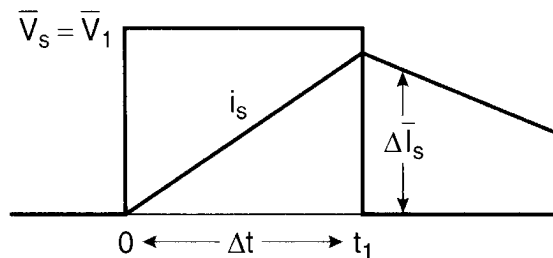


**Figure 8.73** Stator transient parameters measurement

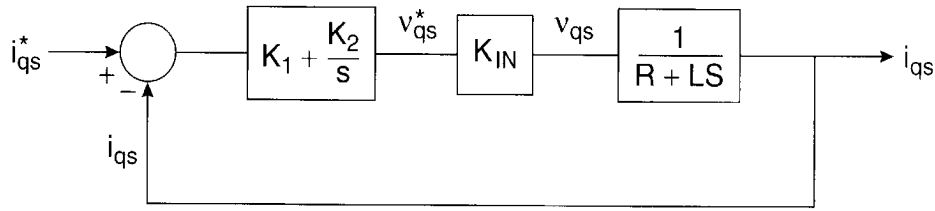


**Figure 8.74** Stator current loop with P-I control

**Step 5: Measure rotor time constant  $T_r$**

- Set up the  $i_{ds}$  loop and inject a dc current pulse for several seconds to establish the rotor flux, as shown in Figure 8.75. Turn off the inverter at time  $t_1$ , open-circuiting the machine. Measure the induced voltage  $v_m(t)$  on the stator side. The rotor flux in the equivalent circuit will decay exponentially with the time constant, which can be given by the equation

$$i_r R_r + L_r \frac{di_r}{dt} = 0 \quad (8.256)$$

The  $v_m(t)$  expression is given as

$$v_m(t) = L_m \frac{di_r}{dt} \quad (8.257)$$

which is plotted in Figure 8.75. The time constant  $T_r$  can be calculated as

$$\frac{T_r}{v_m(t_1)} = \tan \theta = \frac{t_2 - t_1}{v_m(t_2) - v_m(t_1)} \quad (8.258)$$

or

$$T_r = \frac{v_m(t_1)}{v_m(t_2) - v_m(t_1)} (t_2 - t_1) \quad (8.259)$$

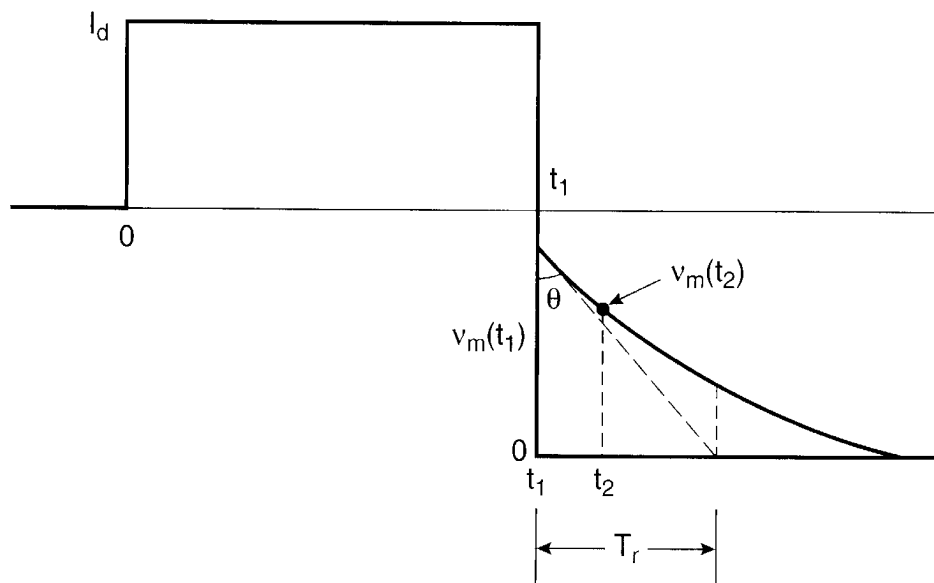


**Figure 8.75** Rotor time constant  $T_r$  measurement

**Step 6: Tune the current model flux vector estimation (see Figure 8.30)**

- Operate the drive in no-load volts/Hz control mode to establish a certain speed with a proper  $V_s/\omega_e$  ratio to establish rated flux  $\psi_r$ .
- Plug the  $T_r$  value in Figure 8.30 and change  $L_m$  until the calculated  $i_{qs} = 0$  so that the entire current is  $i_{ds}$  (magnetizing current). This  $i_{ds}$  is the rated magnetizing current for the rated  $\psi_r$ . The vector control currents are now tuned with  $\psi_r$  orientation.

**Step 7: Tune the flux control loop**

The flux control loop transfer function block diagram is given in Figure 8.76, where  $\tau_l$  corresponds to the  $i_{ds}$  loop response delay. Parameters  $L_m$  and  $T_r$  are known.

- Select the optimum P and I gains of the flux loop.

**Step 8: Measure mechanical inertia  $J$  and friction coefficient  $B$** 

- With the vector control active, establish torque at no-load, as shown in Figure 8.77.

The speed equation can be given as

$$T_e = J\left(\frac{2}{P}\right)\frac{d\omega_r}{dt} + B\omega_r \quad (8.260)$$

If  $B$  is neglected,  $J$  can be given as

$$J = \frac{T_e \Delta t}{\Delta \omega_r} \cdot \frac{P}{2} \quad (8.261)$$

where  $T_e$  is easily calculated from feedback signals (see Figure 8.29).

Considering  $B$ , the exact solution of Equation (8.260) is

$$\omega_r = \frac{T_e}{B} \left(1 - e^{-\frac{t}{\tau_m}}\right) \quad (8.262)$$

where  $\tau_m = \frac{2J}{PB}$  is the mechanical time constant. Both  $B$  and  $J$  can be solved from Equation (8.262), which measures  $\omega_r$  at two different instants.

Although we considered direct vector control with current model estimation as the example, it is possible to tune an indirect vector control and voltage model estimation with these parameter measurements. Finally, it should be noted that with step signal injection, some amount of skin effect in the rotor bars will reduce accuracy.

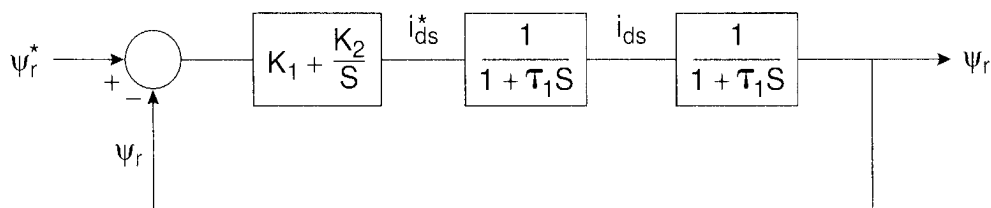


**Figure 8.76** Flux control loop with P-I control

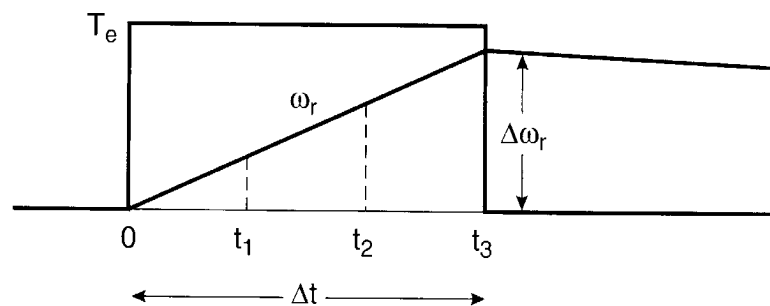


**Figure 8.77** Rotor inertia  $J$  and friction coefficient  $B$  measurement

## 8.9 SUMMARY

In this chapter, we extensively reviewed the different control and feedback signal estimation techniques for cage-type induction motor drives. This class of drives is widely used in various industrial applications, and the technology is continuously expanding. Therefore, a somewhat lengthy discussion on the subject was justified.

Both scalar and vector control techniques with appropriate feedback signal estimation were covered. In scalar control, we emphasized open loop volts/Hz control because of its popularity in industrial applications. A few more scalar control techniques were reviewed briefly for completeness. Vector control with rotor and stator flux orientation was discussed extensively because of its importance in high-performance drive applications. The vector control implementation with corresponding feedback signal estimation is complex, and therefore, digital control with high-speed, powerful microprocessor or DSP is essential. It is expected that vector control will eventually emerge as the industry-standard control method for induction motor drives.

Speed sensorless vector control is an emerging technology. A number of speed estimation techniques have been reviewed. However, very low-speed operation, including start-up at zero frequency, remains a challenge. DTC control was discussed in detail. It has been accepted commercially, and it will be interesting to see how it competes with vector-controlled drives. The adaptive control methods, particularly the sliding mode control were discussed in some detail for a vector-controlled drive. Fuzzy logic and neural network-based adaptive controls constitute emerging technologies and will be covered in Chapters 11 and 12, respectively. Most of the control and estimation concepts for induction motor drives are also applicable for synchronous motor drives. Self-commissioning of drives was covered at the end of this chapter. Finally, the reader should note the difference between a space vector and rms phasor and the corresponding vector or phasor diagrams.

## REFERENCES

1. B. K. Bose (Ed.), *Power Electronics and Variable Frequency Drives*, IEEE Press, NY, 1996.
2. I. Boldea and S. A. Nasar, *Vector Control of AC Drives*, CRC Press, NY, 1992.
3. R. Ueda, T. Sonada, K. Koga, and M. Ichikawa, "Stability analysis in induction motor driven by V/f controlled general purpose inverter", *IEEE Trans. Ind. Appl.*, vol. 28, pp. 472–481, March/April 1992.

4. A. B. Plunkett, "A current-controlled PWM transistor inverter drive", *IEEE IAS Annu. Meet. Conf. Rec.*, pp. 785–792, 1979.
5. A. B. Plunkett and D. L. Plette, "Inverter-induction motor drive for transit cars", *IEEE Trans. Ind. Appl.*, vol. 18, pp. 26–37, 1977.
6. E. P. Cornell and T. A. Lipo, "Modeling and design of controlled current induction motor drive system", *IEEE Trans. Ind. Appl.*, vol. 13, pp. 321–330, July/Aug. 1977.
7. B. K. Bose, "Variable frequency drives – technology and applications", *PEMC Conf. Rec.*, Poland, 1994.
8. W. Leonhard, "Adjustable speed ac drives", *Proc. Of the IEEE*, vol. 76, pp. 455–471, 1988.
9. F. Blaschke, "The principle of field orientation as applied to the new transvector closed loop control system for rotating field machines", *Siemens Review*, vol. 34, pp. 217–220, May 1972.
10. K. Hasse, "Zur dynamik drehzahl geregelter antriebe mit stromrichter gespeisten asynchron-kurzschlusslaufermaschinen", Darmstadt, *Techn. Hochsch., Diss.*, 1969.
11. R. W. De Doncker and D. W. Novotny, "The universal field oriented controller", *IEEE IAS Annu. Meet. Conf. Rec.*, pp. 450–456, 1988.
12. B. K. Bose, "Variable frequency drives—technology and applications", *Proc. Int'l. Symp. Ind. Elec.*, Budapest, Hungary, pp. 1–18, 1993.
13. B. K. Bose, "High performance control and estimation in ac drives", *IEEE IECON Conf. Rec.*, pp. 377–385, 1997.
14. P. Jansen and R. D. Lorenz, "A physically insightful approach to the design and accuracy assessment of flux observers for field oriented induction machine drives", *IEEE IAS Annu. Meet. Conf. Rec.*, pp. 570–577, 1992.
15. G. Kaufman, L. Garces, and G. Gallagher, "High performance servo drives for machine tool applications using ac motors", *IEEE IAS Annu. Meet. Conf. Rec.*, pp. 604–609, 1982.
16. T. M. Rowan, R. J. Kerkman, and D. Leggate, "A simple on-line adaption for indirect field orientation of an induction machine", *IEEE IAS Annu. Meet. Conf. Rec.*, pp. 579–587, 1989.
17. X. Xu, R. De Doncker, and D. W. Novotny, "A stator flux oriented induction machine drive", *IEEE Power Elec. Spec. Conf.*, pp. 870–876, 1988.
18. K. Rajashekara, A. Kawamura, and K. Matsuse (Ed.), *Sensorless Control of AC Drives*, IEEE Press, NY, 1996.
19. C. Schauder, "Adaptive speed identification for vector control of induction motors without rotational transducers", *IEEE Trans. Indus. Appl.*, vol. 28, pp. 1054–1061, Sept./Oct. 1992.
20. H. Kubota, K. Matsuse, and T. Nakano, "DSP-based speed adaptive flux observer of induction motor", *IEEE Trans. Ind. Appl.*, vol. 29, pp. 344–348, March/April 1993.
21. J. Holtz, "Sensorless position control of induction motor – an emerging technology", *IEEE IECON Conf. Rec.*, pp. II – 112, 1998.
22. Y. R. Kim, S. K. Sul, and M. H. Park, "Speed sensorless vector control of induction motor using extended Kalman filter", *IEEE Trans. Ind. Appl.*, vol. 30, pp. 1225–1233, Sept./Oct. 1994.
23. B. K. Bose and N. R. Patel, "A sensorless stator flux oriented vector controlled induction motor drive with neuro-fuzzy based performance enhancement", *IEEE IAS Annu. Meet. Conf. Rec.*, pp. 393–400, 1997.
24. I. Takahashi and T. Noguchi, "A new quick response and high efficiency control strategy of an induction motor", *IEEE Trans. Ind. Appl.*, vol. 22, pp. 820–827, Sept./Oct. 1986.
25. G. Buja et al., "Direct torque control of induction motor drives", *ISIE Conf. Rec.*, pp. TU2–TU8, 1997.
26. P. Vas, *Sensorless Vector and Direct Torque Control*, Oxford, NY, 1998.
27. K. Hong and K. Nam, "A disturbance torque compensation scheme considering the speed measurement delay", *IEEE IAS Annu. Meet. Conf. Rec.*, pp. 403–409, 1996.
28. K. J. Astrom, "Theory and applications of adaptive control – a survey", *Automata*, vol. 19, pp. 471–486, Sept. 1983.
29. Y. D. Landau, *Adaptive Control – The Model Referencing Approach*, Marcel Dekker, 1979.
30. A. Brickwedde, "Microprocessor-based adaptive speed and position control for electrical drives", *IEEE Trans. on Ind. Appl.*, vol. 21, pp. 1154–1161, Sept./Oct. 1985.
31. U. Itkis, *Control Systems of Variable Structures*, Wiley, NY, 1976.



32. B. K. Bose, "Sliding mode control of induction motor", *IEEE IAS Annu. Meet. Conf. Rec.*, pp. 479–486, 1985.
33. F. Harashima, H. Hashimoto, and S. Kondo, "MOSFET converter-fed position servo system with sliding mode control", *IEEE Trans. Ind. Electron.*, vol. 32, pp. 238–244, Mar. 1985.
34. A. M. Khambadkone and J. Holtz, "Vector controlled induction motor drive with a self-commissioning scheme". *IEEE Trans. Ind. Elec.*, vol. 38, pp. 322–327, Oct. 1991.



# Control and Estimation of Synchronous Motor Drives

## 9.1 INTRODUCTION

Synchronous motor drives are close competitors to induction motor drives in many industrial applications, and their application is growing. They are generally more expensive than induction motor drives, but the advantage is that the efficiency is higher, which tends to lower the life cycle cost. The basic principles of synchronous machines and their characteristics were discussed in Chapter 2. As mentioned before, wound-field synchronous machines (WFSMs) are generally used in high-power (multi-megawatt) applications. On the other hand, permanent magnet synchronous machines (PMSMs) are used in low- to medium-power (up to several hundred horsepower) applications. A traditional line-start 60 Hz machine starts as an induction motor with a cage or damper winding, but locks into synchronous speed at steady state.

The general classifications of PM machines are radial flux (drum-type) and axial flux (or disk-type), and the former type is most commonly used. There are also classifications of sinusoidal and trapezoidal types, as discussed in Chapter 2. A sinusoidal machine can be a surface permanent magnet (SPM) type or an interior or buried permanent magnet (IPM) type. Synchronous reluctance machines (SyRMs), as the name indicates, do not have any separate field excitation. Variable-reluctance or double-reluctance (reluctance variation in both stator and rotor) machines can be stepper or switched reluctance types. The switched reluctance machine (SRM) does not strictly fall into the synchronous machine category.

Some typical applications of synchronous motor drives are:

- Fiber spinning mills
- Rolling mills
- Cement mills
- Ship propulsion